Impacts of retrogressive thaw slumps on the geochemistry of permafrost catchments, Stony Creek Watershed, NWT

Laura Malone

Thesis presented to the Faculty of Graduate and Postdoctoral Studies
in partial fulfillment of the requirements for the degree of
Master of Science in Earth Sciences

Department of Earth Sciences
Faculty of Science
University of Ottawa

Supervisors:
Dr. Ian D. Clark (Department of Earth Sciences)
Dr. Denis Lacelle (Department of Geography)

Thesis Committee:
Dr. Danielle Fortin (Department of Earth Sciences)
Dr. Fred Michel (Carleton University)

The undersigned certify that they have read, and recommend to the Faculty of Graduate and Postdoctoral Studies for acceptance, a thesis entitled: “Impacts of retrogressive thaw slumps on the geochemistry of permafrost catchments, Stony Creek Watershed, NWT” submitted by Laura Malone in partial fulfillment of the requirements for the degree of Master of Science.

____

Dr. Ian Clark
Supervisor, University of Ottawa

____

Dr. Denis Lacelle
Supervisor, University of Ottawa

____

____

Date: _________________________

The undersigned certify that they have read, and recommend to the Faculty of Graduate and Postdoctoral Studies for acceptance, a thesis entitled: “Impacts of retrogressive thaw slumps on the geochemistry of permafrost catchments” submitted by Laura Malone in partial fulfillment of the requirements for the degree of Master of Science.

____
Dr. Ian Clark
Supervisor, University of Ottawa

____
Dr. Denis Lacelle
Supervisor, University of Ottawa

____

____

Date: ______________________________

Abstract

Retrogressive thaw slumps are one of the most dramatic thermokarst landforms in periglacial regions. This thesis investigates the impacts of two of the largest hillslope thaw slumps on the geochemistry of periglacial streams on the Peel Plateau, Northwest Territories and aims to describe the inorganic geochemistry of runoff across active mega-slumps, impacted and pristine tundra streams, as well as that of the ice-rich permafrost exposed in the slump headwalls. Slump runoff is characterized by elevated suspended sediments (911 g/L), high conductivity (2700 µS/cm), and high SO_4^{2-} (up to 2078 ppm). The runoff originates as a solute-rich meltwater near the slump headwall, and leaches and re-dissolves soluble salts (e.g., gypsum) as it flows along the mudflow. Conductivity increases until the runoff mixes with pristine tundra streams, diluting the slump runoff signal. SO_4^{2-}/Cl^- is used as a tracer to isolate the slump runoff signal in impacted waters, and suggests that the contribution of slump runoff to the Peel River has been increasing since the 1960s.

Résumé

Les glissements de fonte rétrogressifs sont l'une des conséquences de la dégradation de pergélisol les plus dramatiques dans les régions périglaciaires. Cette thèse porte sur les impacts de deux des plus gros glissements de fonte sur la géochimie des cours d'eau périglaciaires sur le Plateau Peel, aux Territoires du Nord-Ouest. L'objectif principal de cette thèse est de décrire la géochimie inorganique de l'eau de fonte des glissements, des eaux affectées et non-affectées par les glissements, et de la glace présente dans le pergélisol formant le mur du glissement. Les eaux de fonte sont caractérisées par une teneur élevée en sédiments en suspension (911 g/L), une conductivité élevée (2700 µS/cm), et une teneur élevée SO_4^{2-} (max. 2078 ppm). L'eau de fonte, qui tire son origine près du mur de glissement, est au départ riche en ions. À mesure qu'elle circule dans la coulée de boue, elle entraîne la dissolution des minéraux solubles (p.ex., le gypse). En outre, la conductivité de l'eau de fonte augmente jusqu'à ce que cette dernière se mélange aux eaux claires, diluant son signal géochimique. La dissolution et la lessivation des minéraux de soufre dans la coulée de boue sont la source des concentrations élevées de SO_4^{2-}. Le rapport SO_4^{2-}/Cl^- est utilisé comme traceur pour identifier et quantifier la contribution des glissements de fonte régrogressifs aux les eaux affectées. Les résultats indiquent que la contribution de l'eau de fonte des glissements dans la rivière Peel est en augmentation depuis les années 60.

Acknowledgements

This project would not have been possible without funding from NSERC (Natural Sciences and Engineering Research Council of Canada), OGS (Ontario Graduate Scholarship), NSTP (Northern Scientific Training Program), PCSP (Polar Continental Shelf Program) and the University of Ottawa.

There are many people that were also instrumental in making this project a success. Special thanks to Ping Zhang from the Department of Earth Sciences, Paul Middlestead and Patricia Wickham at the G.G. Hatch laboratory, Glenn Poirier at the Earth Sciences MicroAnalytical Laboratory and Ron Hartree at the University of Ottawa X-Ray Laboratory. I'd also like to thank Alex Yard and Shamus Duff for their assistance in the field.

I must especially thank my research supervisors Dr. Ian Clark and Dr. Denis Lacelle. I am forever grateful for their encouragement, patience and support throughout the duration of this project. I would also like to thank Steve Kokelj for being a great mentor and especially for his collaborative support with fieldwork.

To my wonderful officemates and fellow grad students, thank you for always creating a positive and fun work environment. Thank you so much for all your support and encouragement! You have all helped make this a truly memorable experience.

Finally, I would like to thank my family and friends for their continued support over the past two and a half years. I am hugely appreciative for the love and support they have given me throughout my academic career.

Table of Contents

List of Tables

List of Figures

---

1. INTRODUCTION

Across the circumpolar Arctic, the most abrupt impacts to freshwater ecosystems result from degrading permafrost (e.g. active layer deepening, thermokarst disturbance such as active layer detachment slides, lake drainage, thaw slumps ; Lamoureux and Lafreniere, 2009; Marsh et al., 2010; Kokelj et al., 2013). The elevated ionic concentration in near-surface permafrost (Kokelj and Burn, 2005) may result in increasing ionic concentrations in the fluvial system due to deeper active layer thawing and degradation of near-surface permafrost (Keller et al. 2010). Further, local-scale studies (up to ~ 1 km^2) indicate that suspended sediment and solute concentrations in streams situated immediately downstream of active layer detachment slides, which are isolated geomorphic events, may be orders of magnitude greater than from the adjacent landscape (Kokelj and Lewkowicz, 1999; Bowden et al. 2008; Lamoureux and Lafreniere 2009; Stewart and Lamoureux 2011; Dugan et al. 2012). A growing number of observations support the idea that permafrost thaw may be driving changes to the water quality of major circumpolar rivers (Raymond et al., 2007 ; Frey and McClelland, 2009).

Retrogressive thaw slumps are one of the most dynamic manifestations of permafrost degradation and commonly develop in ice-rich glaciogenic deposits throughout the circumpolar arctic (Lantz and Kokelj, 2008; Lantuit and Pollard, 2008). Unlike active layer detachment slides, a thaw slump may enlarge for decades until the exposed ground ice is covered by the accumulation of thawed sediments (Burn and Lewkowicz, 1990; Burn and Friele, 1989). Some of the largest thaw slumps ever observed (up to 40 ha), termed “mega-slumps”, have recently developed along valley sides and open slopes of fluvial incised ice-rich landscapes across northwestern Canada (Lacelle et al., 2010; Kokelj et al., 2013).

Thaw slump formation can be initiated by a variety of mechanisms that expose ground ice to melting. These include mechanical erosion by fluvial processes or wave action (Lantuit and Pollard, 2008), thermally driven subsidence along lakeshores (Kokelj et al., 2009b) or mass wasting triggered by extreme thaw or precipitation (Lacelle et al., 2010). Slump growth is then driven by summer ground ice ablation and the progressive backwasting of the ice-rich headwalls (Lewkowicz, 1987a). The thawed materials accumulate as a mud-slurry on the slump floor and may be transported downslope by debris flows that can join water bodies such as streams, lakes and even the ocean in the case of coastal slumps. The mass-wasting associated with the growth of these slumps is making immense quantities of previously frozen, highly weatherable sediments available for leaching and transport to hundreds of streams throughout these landscapes. As a result, an increase in the intensity of thaw slump activity has the potential to dramatically alter periglacial fluvial regimes where the flux of water, sediment and solutes is typically driven by snowmelt and rainfall events (Carey and Woo, 2001; Dyke et al., 2002). The ephemeral runoff is rapidly transported through a shallow, nutrient-poor active layer which limits the sediment and solute transport from the landscape to streams and deeper ground water contribution is negligible (Lewkowicz and Kokelj, 2002; Quinton and Marsh, 1999; Lim and Douglas, 2003). The geochemical contrast between ion-rich permafrost and the overlying leached active layer indicates that there is potential for chemical modification of soils and surface waters as a result of thawing permafrost and that the magnitude of impacts would likely vary with the scale and intensity of degradation (Kokelj and Lewkowicz, 1999; Kokelj and Burn, 2005; Keller et al., 2007). Modifications to permafrost terrain and ecological conditions that are anticipated in response to climate warming suggest that the importance of catchment processes on the chemistry and biology of Arctic streams will intensify (Osterkamp and Romanovsky, 1999; Jorgenson et al., 2006; Lantz and Kokelj, 2008). Recent studies support the idea that growth of active thaw slumps along lakeshores can modify water quality for several decades after slumps have stabilized (Kokelj et al., 2009b), with significant impacts to lake ecosystems (Mesquita et al., 2009; Theinpont et al., 2013).

Considering that a recent increase in the intensity and frequency of thaw slump activity has been observed (e.g. Lantz and Kokelj, 2008; Lantuit and Pollard, 2008) and is expected to continue with anticipated climate warming (Lewkowicz, 1991), this thesis investigates the geochemical impacts of thaw slumps on permafrost watersheds.

1.1 Thesis Structure and Research Objectives

This thesis is part of an ongoing collaborative study with the community of Frt McPherson (NWT) on the impacts of retrogressive thaw slumps on the Peel Plateau. In this study, we characterize the chemistry of runoff from thaw slumps and associated mudflows to investigate in detail the impacts of active hillslope retrogressive thaw slumps on the geochemical composition of periglacial streams in the Stony Creek watershed and of the Peel River.

The goals of this thesis are threefold:

(I) To describe, in detail, the chemical composition of the slump runoff from two slumps within the Stony Creek Watershed and to determine factors that influence the chemistry of the runoff;

(II) To assess the influence of slump runoff on unaffected streams in the watershed; and

(III) To isolate and trace slump runoff contribution in affected waters and attempt to detect its presence in permafrost watersheds.

1.2 Thaw slump morphology

Slump morphology is a function of ground ice volume and the nature of the slope (Lewkowicz, 1987a; Lantuit and Pollard, 2005). General thaw slump morphology consists of a near vertical headwall (up to 30m high) where the massive ice body or sediment rich ice is exposed (Burn and Lewkowicz, 1990) and is typically overlain by a 2-5m thick sediment deposit (Figure 1C). As the headwall retreats due to ice ablation, it creates a horseshoe-shaped scar in the landscape (Figure 1A,B) and the thawed material accumulates and forms a mud-slurry on the low-gradient slump floor (Figure 1C). The thawed material can then be transported downslope as debris flows. In some instances, these debris flows dam the flow of rivers to form lakes whereas others spill directly into streams. The debris flows can be many meters thick and can increase in length on a yearly basis (Figure 1D). The removal of supernatant water and some fluidized sediment allows the remaining supersaturated sediments to slowly dewater leaving behind a thick layer of cohesive mud. There is clear zonation, with increasing distance from the headwall, from pooled supersaturated sediment and standing water at the base of the headwall, to very plastic mud (sometimes with a dry crust), and eventually to dry mud. The zone of plastic mud experiences slow flow and often forms distinct lobes (Lantuit and Pollard, 2008). Water and liquefied mud flowing across the stable slump floor gradually erodes a network or channels and gullies. This can lead to the exposure of more buried ice that may be situated beneath the slump floor (Lantuit and Pollard, 2005).

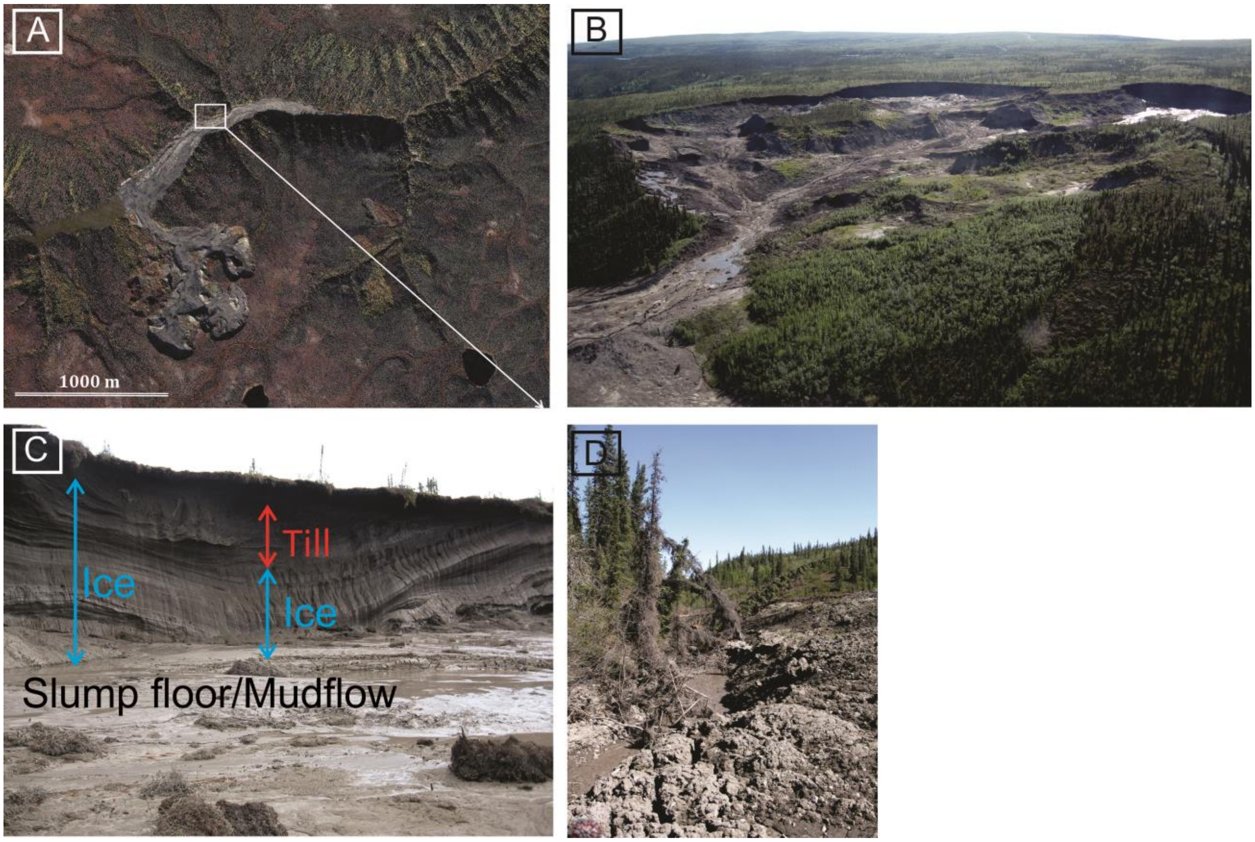

Figure 1. (A) Quickbird image of Charas slump located off the Dempster Highway (B) Aerial photo of slump scar (~1km across) (C) Photo of slump headwall taken from slump floor (D) Debris flow infilling stream

1.3 Thaw slump formation

Thaw slumps initiate when, by some mechanism, a body of ice, or ice-rich sediment is exposed to ablation. As the ice melts, the headwall retreats to form a scar in the landscape and material can move downslope as a debris flow. These mechanisms of formation can include, but are not limited to: mechanical erosion by fluvial processes of wave action, thermal subsidence along lakeshores, fire, and heavy precipitation. The thickness of the layer of sediment covering the ice body is usually slightly greater than the active layer depth at the time of thermokarst. Any increase in the active layer depth or reduction in the thickness of sediment cover by either erosion by runoff or flow, can trigger new thermokarst (Lantuit and Pollard, 2008).

1.3.1 Mechanical erosion by fluvial processes or wave action

Retrogressive thaw slumps are often initiated by wave erosion at the base of ice-rich coastal bluffs, which uncovers massive ice and leads to ice ablation, or by active layer detachments (a form of slope failure linked to deep seasonal thaw which may occur as coastal erosion oversteepens coastal slopes) (Lewkowicz, 1990). If the massive ice melts at a rate that exceeds the rate of erosion along the coast, then a retrogressive thaw slump forms (Lewkowicz, 1987). This formation mechanism applies to thaw slumps located along the coast, or along a river bank (Lantuit and Pollard, 2008).

During the brief open water season, ice-rich permafrost coasts in the southern Beaufort sea experience erosion rates on the order of 1 to 5 m/yr (Solomon, 2005). Warming air temperatures and increasing sea levels in the Arctic will weaken coastal sediments by thawing ice-rich earth materials and lead to increased wave energy by reducing sea ice cover and thus predispose arctic coasts to even higher rates of erosion (McGillivray et al., 1993).

Coastal erosion is amplified where retrogressive thaw slumps occur and is diminished where they are absent (Lantuit and Pollard, 2008). The increase in erosion is associated with three processes: (1) the presence of large quantities of massive ground ice which facilitates the thermoabrasion of sediments (Kobayashi, 1985; Are, 1988; Hequette and Barnes, 1990); (2) the melting of the massive ice body in the headwall of the slump which can induce a settlement of the ground by over 20m (Lantuit and Pollard, 2005), thereby reducing the volume of materials in the shore-backshore area and thus reducing resistance to erosional processes; (3) mudflows that originate from the supernatant water derived from melting massive ice which accumulate at the base of the headwall and flow down the slump floor to the coast, preferentially removing cohesive fine-grained sediments and thus increasing the relative proportion of unconsolidated coarse-grained materials on the slump floor and the cliff (Lantuit and Pollard, 2008).

Coastal erosion may be linked to retrogressive thaw slumps through the lowering of the cliff profile, the sorting of sediments by mudflows covering coastal cliffs, and the presence of remaining ground ice below the slump floors. The difference between annual headwall retreat rates of retrogressive thaw slumps and coastal retreat rates can lead to the development of large polycyclic retrogressive thaw slumps (Lantuit and Pollard, 2008).

1.3.2 Thermal subsidence along lakeshores

This formation mechanism is important in the polycyclic behaviour (initiation and growth of slumps within an area previously affected by slumping; see section 1.3.4) of thaw slumps, and is not seen as an initial formation mechanism. It’s likely that mechanical erosion by wave action along lakeshores initiates slumping (Coté and Burn, 2002), causing an increase in ground temperatures due to the high thermal conductivity of exposed mineral soils and deep snow accumulation in winter. The removal of the insulating surface organic cover increases ground warming in summer and enhances active-layer thaw in a manner similar to effects following forest fire (Mackay, 1995). Modelling by Kokelj et al., (2009b) has shown that thermal disturbance caused by thaw slumping adjacent to tundra lakes can lead to rapid near-surface lateral talik expansion. Talik growth into ice-rich materials is likely to cause lake-bottom subsidence and rejuvenation of shoreline slumping. Although wave-induced thermal erosion may lead to the initiation of new lakeside slumps, it is unlikely that wind-generated waves or currents could remove sediments from disturbed shorelines of small lakes at rates large enough to account for frequent rejuvenation of existing slumps. Where the permafrost is ice-rich, lakeside polycyclic thaw slumping may be sustained for centuries (Kokelj et al., 2009b).

1.3.3 Other mechanisms

Intense precipitation could trigger thaw slump formation in much the same way as it triggers landslides in permafrost-free environments. Heavy precipitation also aids in removing the mud slurry on the slump floor, keeping the ice exposed to ablation, and allowing the slump to continue backwasting (Lacelle et al., 2010).

Fire-induced active layer deepening can also lead to catchment wide permafrost thawing, but this type of degradation is usually restricted to the top few decimetres of permafrost (Mackay, 1995; Wolfe et al., 2000).

1.3.4 Thaw slump growth-stabilization

Once thaw slump formation has been triggered, and the ice body in the headwall is exposed, ice ablation occurs as a result of solar radiation and heat flux. Once the headwall has started to retreat, it will continue until the ice body has completely melted, or the ice rich headwall is covered by the slumped sediments, protecting the ice from further melt. On average, a thaw slump remains active for 30-50 years after which local vegetation re-colonises the slump floor, leaving only a horseshoe-shaped scar in the landscape (French and Egginton, 1973; Burn and Friele, 1989; Bartleman et al., 2001). Frequently, stabilised and re-vegetated retrogressive thaw slumps are reactivated and are termed polycyclic slumps (Mackay, 1966). Polycyclic behaviour can be explained by the fact that there is incomplete melting of massive ice by backwasting thermokarst, hence most slumps contain some portion of the original massive ice body under the stabilized and revegetated slump floors (Burn, 2000).

1.4 Thermokarst disturbance affecting lake chemistry

Although there has been no previous work done to characterize thaw slump runoff and to determine its impacts on streams, previous studies have shown that thermokarst disturbance (including thaw slumps) can affect the water quality of small upland lakes in the Mackenzie Delta region (Kokelj et al., 2005 and Kokelj et al., 2009a). As discussed above, thaw slumps often form along lakeshores due to the erosion that exposes ice rich sediments (Coté and Burn, 2002). In 2005, Kokelj et al. studied 11 pristine and 11 disturbed lakes and found that mean concentrations of Ca^{2+}, Mg^{2+}, and SO_4^{2-} were significantly higher in lakes affected by thermokarst. The concentrations in the lake water were elevated as a result of surface runoff transporting soluble materials from the degrading permafrost. It was further suggested that with a disturbance as small as 2% of the catchment area, lake water chemistry may be modified, and the lake water may remain affected for several decades after slumping has ceased. In 2009, the study was expanded to include even more lakes (34 affected and 39 unaffected). Thaw slumping was found to be the primary source of variability in water chemistry of the study lakes. Environmental factors typically used to explain variation in tundra lake water quality, including surficial geology and proximity to the treeline or coast, were secondary to the main cause, which is permafrost degradation (Kokelj et al., 2009a).

2. **REGIONAL SETTING**

2.1 Stony Creek watershed, Northwest Territories

The study region is situated in the 1100 km^2 Stony Creek watershed. The watershed is ~30 km southwest of Fort McPherson (67°25’N, 134°51’ W), NWT at the eastern foothills of the Richardson Mountains on the Peel Plateau (Figure 2). The gravel bed streams of the Stony Creek watershed run parallel to the Dempster highway, draining the Peel Plateau into the Peel River which contributes significant discharge and sediment loads to the Mackenzie Delta (Carson et al., 1999). This chapter will include a description of the Stony Creek watershed and the surrounding area as well as a description of the two thaw slumps that were the focus of this study.

2.1.1 Glacial history and geology

The Peel Plateau reaches an elevation of 950 m and is located within the maximum westward extent of the Laurentide Ice Sheet (LIS) (Dyke et al., 2002). The maximum extent of the LIS was reached ca. 30 ka BP (Duk-Rodkin and Lemmen, 2000) but the plateau was also affected by two subsequent re-advances of the LIS termed the Katherine phase (22ka) and the Tutsieta Lake phase (13ka). Both the Katherine and Tutsieta Lake phases are marked by the presence of moraines and ice-marginal melt channels. The Katherine Creek phase is recorded by channels extending from the southern Mackenzie Mountains to the Richardson Mountains (Lemmen et al., 1994), one of which is currently occupied by Stony Creek (Duk-Rodkin and Hughes, 1995). Similarly, part of the ice-marginal channel of the Tutsieta Lake phase now serves as the modern route of the Peel River (Duk-Rodkin, and Lemmen, 2000). Drainage blockage on the Peel Plateau, caused by the glacial re-advance of both phases, resulted in the formation of temporary glacial lakes and deposition of discontinuous lake sediments on the rolling moraine of the plateau. The study area has been ice free since ca. 12 ka BP (Zazula et al., 2009) and postglacial stream incision of up to 500 m has produced spectacular canyons on the Peel Plateau (Duk-Rodkin, and Lemmen, 2000).

Elevations in the Stony Creek watershed range from about 600 m in the mountains to less than 10 m above sea level at the confluence with the Peel River. The geology is dominated by Lower Cretaceous marine shale and siltstone bedrock of the Arctic Red River Formation (Figure 3). This is overlain by up to 60 m of Late Pleistocene glacial, glacio-fluvial and glacio-lacustrine sediments (Figure 4) hosting ice-rich permafrost (Norris, 1984; Smith et al. 2004).

On a more regional scale, the geology of the area to the southeast (Fort Good Hope and surrounding areas) consists of Lower-Middle Devonian dolomite, anhydrite and limestone units of the Bear Rock, Headless and Nahanni Formations.

The thickness of permafrost reaches 100m at Inuvik, and has been estimated at 400 m for a nearby site 30 km west of Fort McPherson (Smith and Burgess, 2000, Mackay, 1967). Lacelle et al. (2004) suggests that the sediment-rich ice formed during permafrost aggradation following the retreat of the LIS between 18 000 and 12 500 BP.

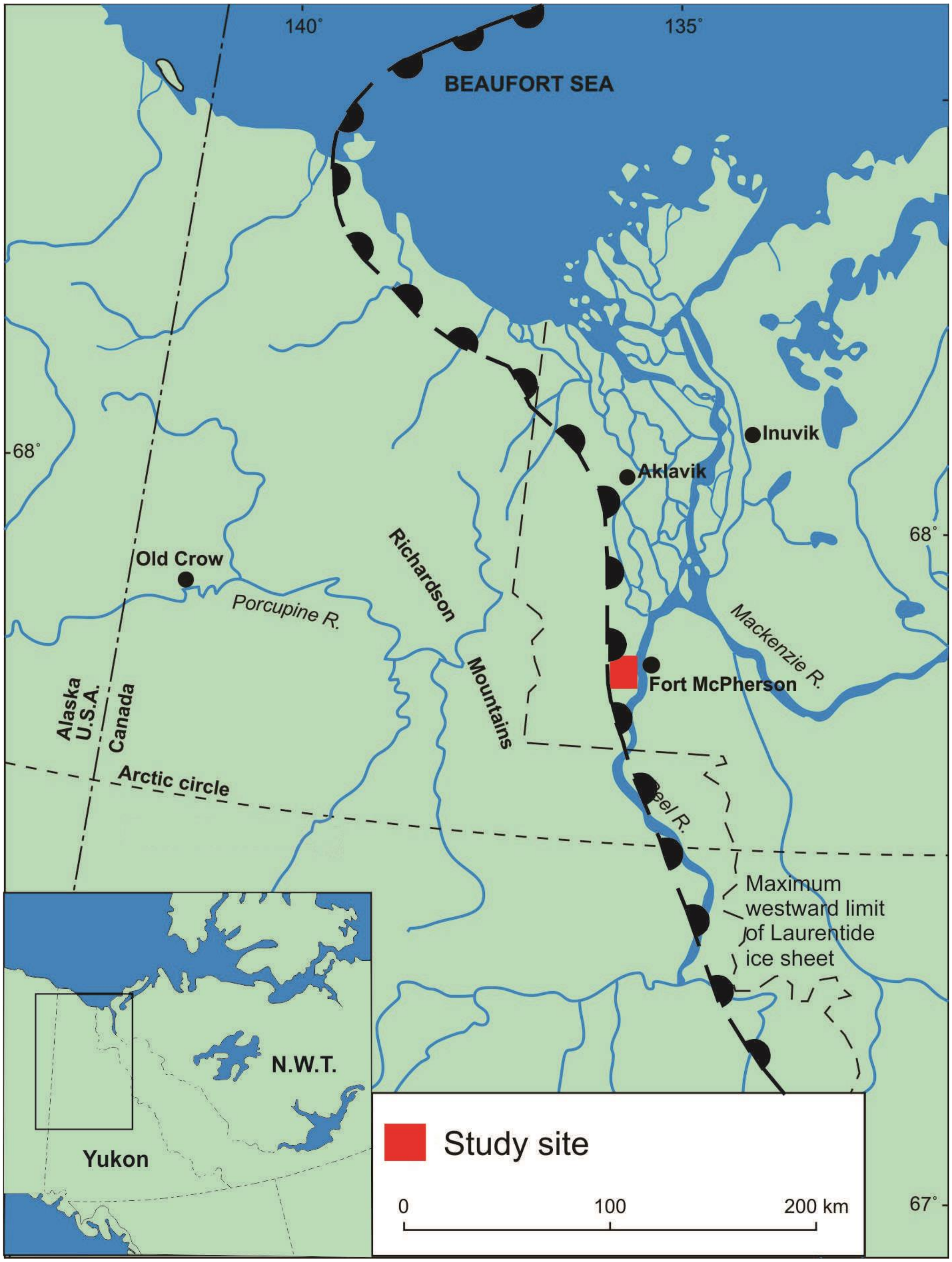

Figure 2. Location of the Stony Creek Watershed, Northwest Territories.

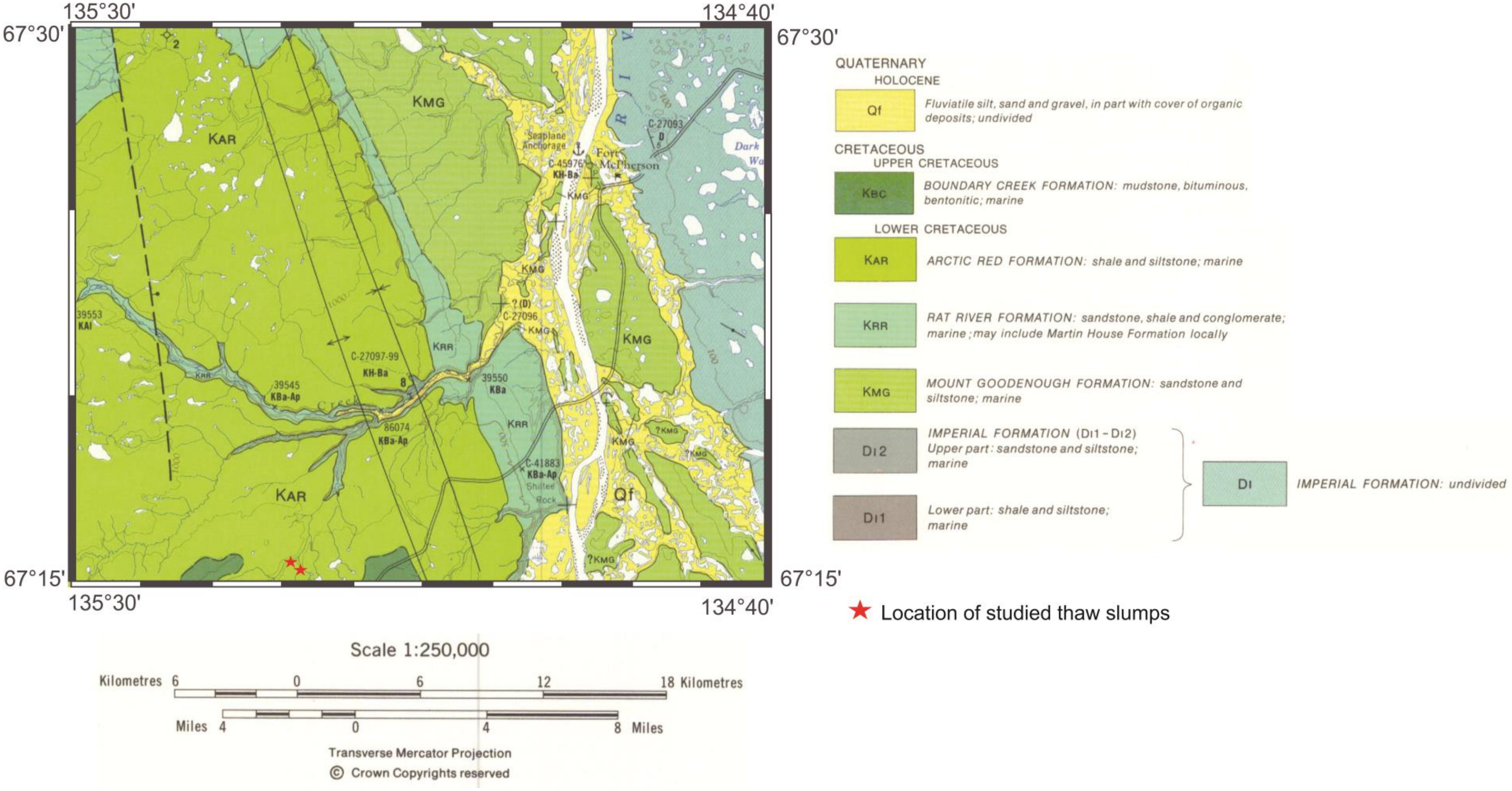

Figure 3. Geology of the Stony Creek Watershed (modified from Geological Survey of Canada, Norris, 1981).

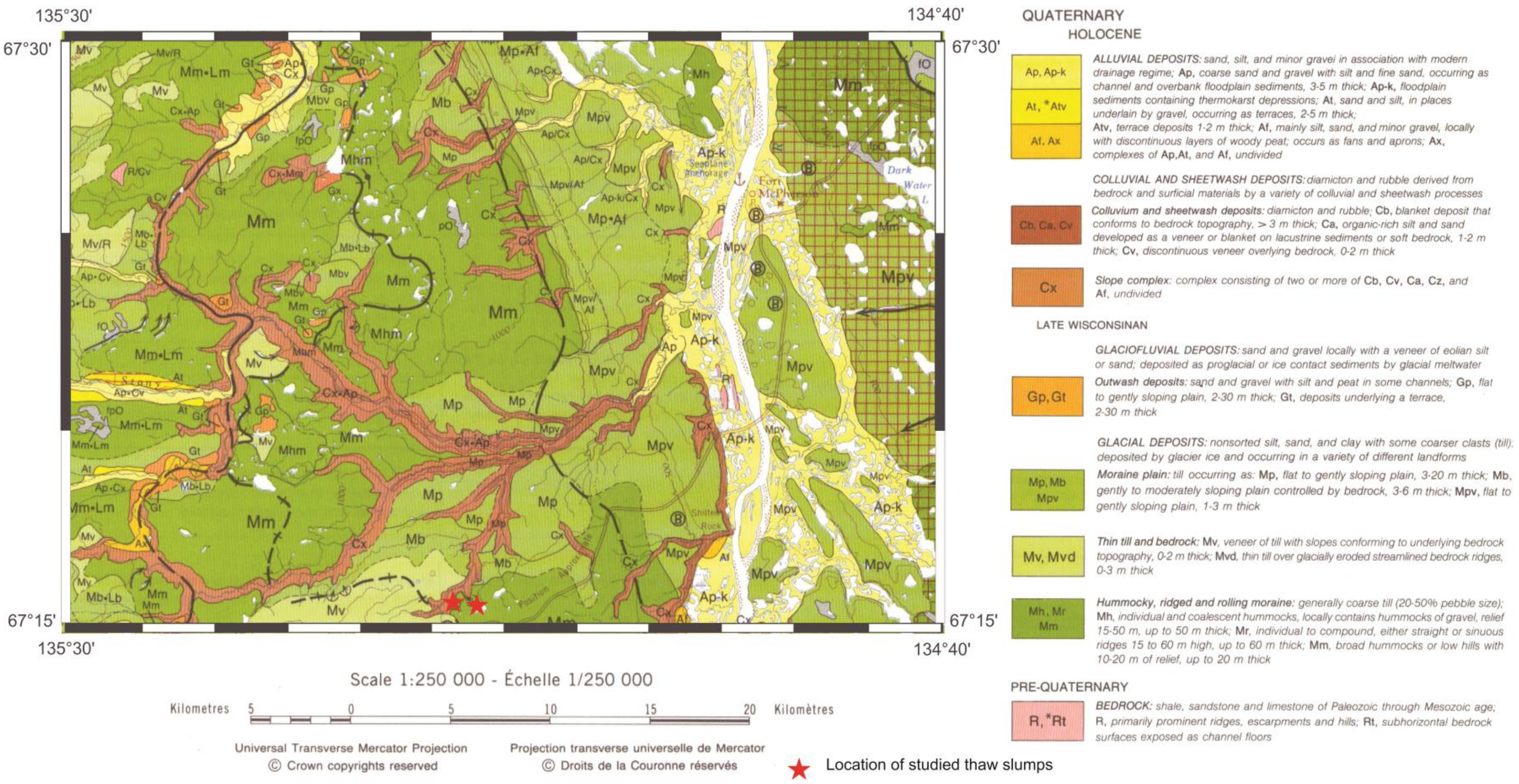

Figure 4. Surficial Geology of the Stony Creek Watershed (modified from Geological Survey of Canada, Duk-Rodkin, 1992).

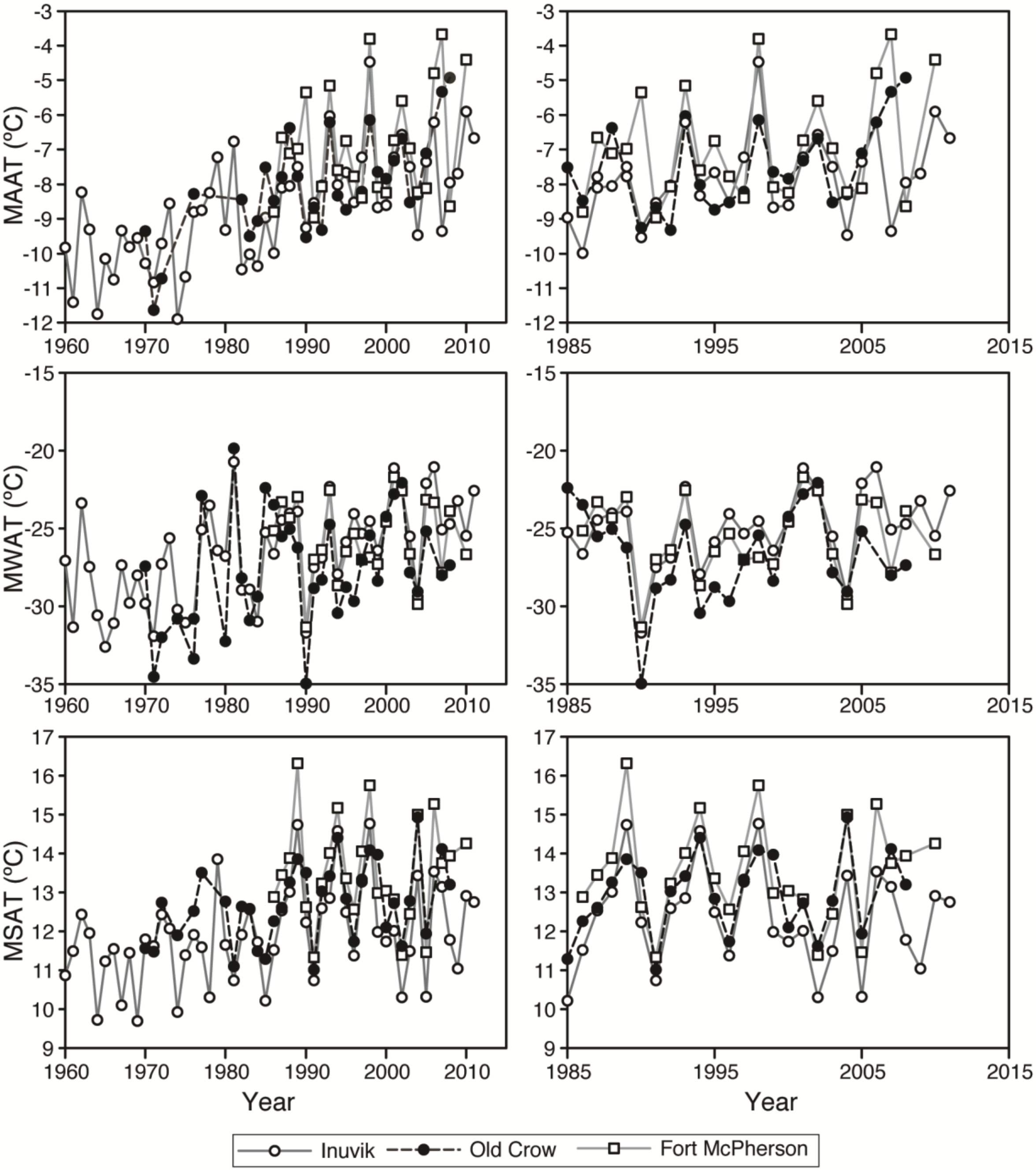

Figure 5. Mean annual (MAAT), winter (MWAT) and summer (MSAT) air temperatures for Inuvik, Old Crow and Fort McPherson from 1960-2012

2.1.2 Climate and vegetation

The regional climate consists of long, cold winters and short, cool summers. The mean annual air temperature at Fort McPherson (1986-2007) is -6.2 ºC with mean annual summer air temperatures of 13.3°C (Environment Canada, 2010). July is the warmest month with average temperatures of 15°C (1986-2007), while the coldest temperatures occur in January with an average of -27°C (Figure 6). Although there is a decreasing trend in mean summer air temperature recorded at Fort McPherson (Figure 6), an increasing trend can be seen in mean annual air temperature (Figure 6). Mean annual air temperatures in the region have increased at a rate of 0.77°C per decade since the 1970s (Burn and Kokelj, 2009), making the western Canadian Arctic one of the most rapidly warming regions on Earth (Serreze et al., 2000).

Total precipitation at Fort McPherson (1986-2007) averaged 295 mm, with rainfall representing 148mm. Maximum annual rainfall values can approach 250 mm. Three of the five wettest summers on record extending back to the 1920s have occurred in the past decade, suggesting an increase in summer precipitation. This trend can be seen in the total summer precipitation recorded from 1986-2007 where there is a slight overall increase in the amount of summer precipitation with a sharp increase from 2004 to 2007 (Figure 7). Winter snowfall amounts over the same time period show a decreasing trend with a sharp decrease from 2005-2007 (Figure 7). A slight decrease can also be seen in the overall yearly precipitation from 1986-2007 (Figure 7).

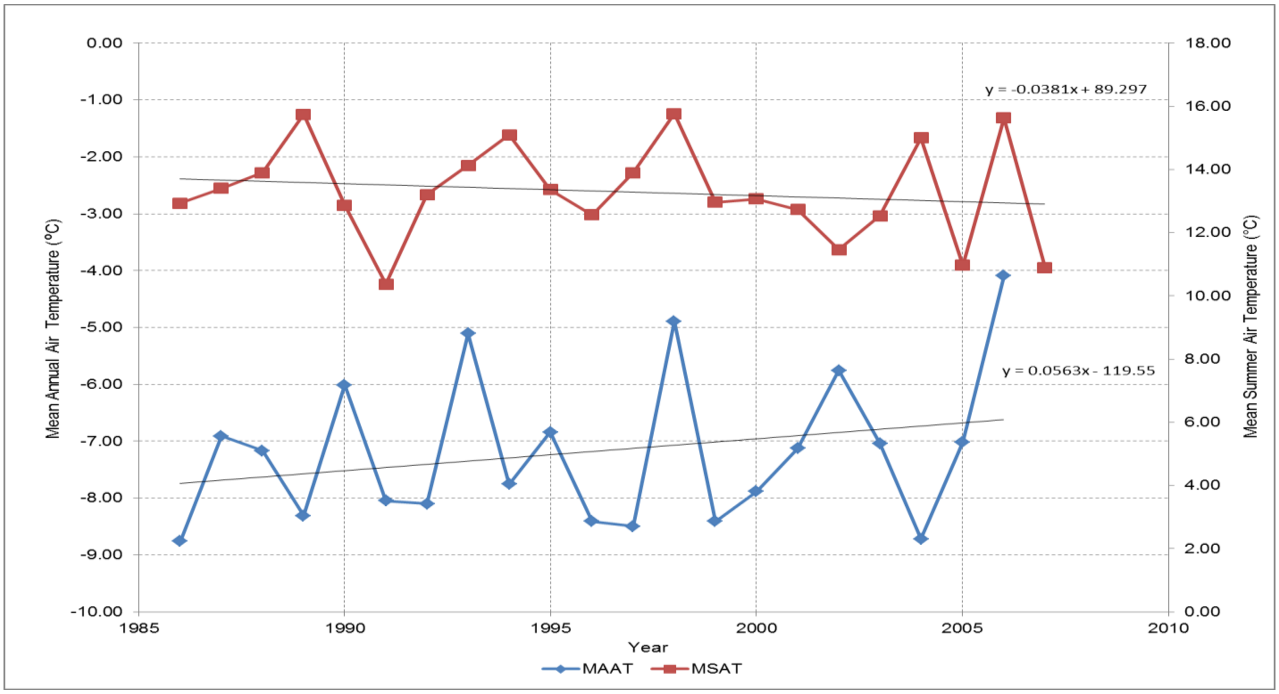

Figure 6. Mean Summer and Annual Air Temperature (June-August, 1986-2007), Fort McPherson.

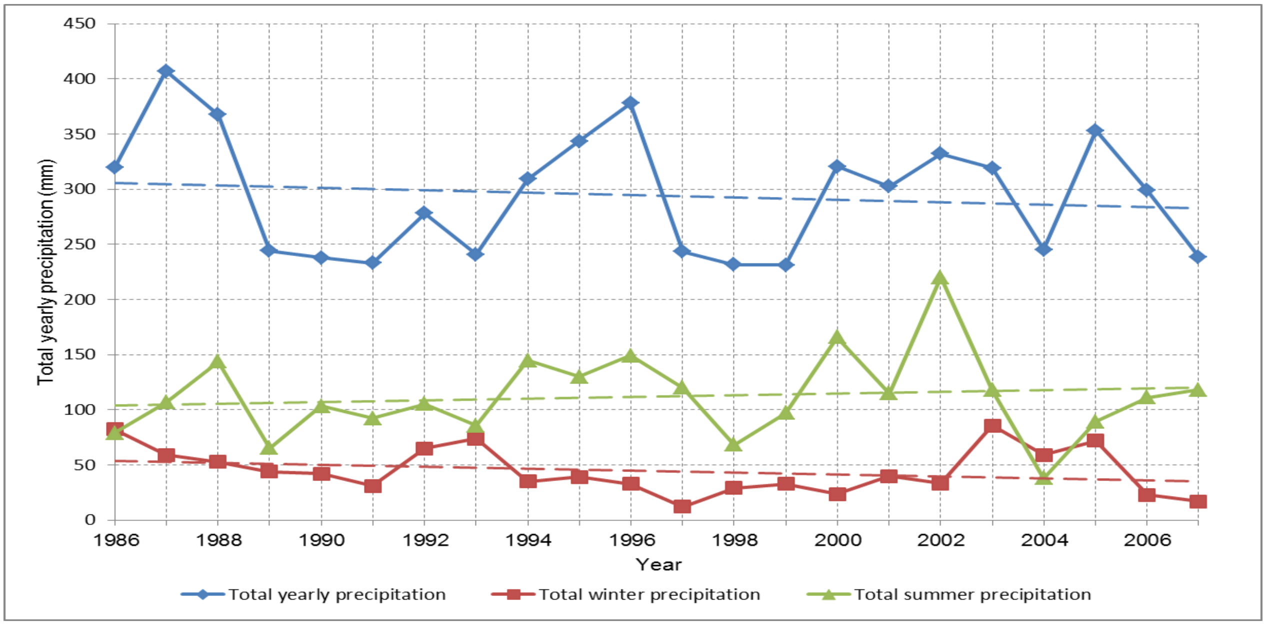

Figure 7.Total yearly precipitation (1986-2007), summer rainfall (June-August) and winter snowfall (December-February) Fort McPherson.

Vegetation plays an important role in the insulation of permafrost. In the Stony Creek watershed, vegetation consists of open forest-tundra woodlands in the valley bottoms, transitioning to shrub and dwarf shrub tundra at higher elevations (Smith et al. 2004). Overall vegetation is dominated by black and white spruce, sphagnum moss and lichens. Dwarf birch, alder and willow form a sparse layer of high shrubs while Labrador tea and species of *Vaccinium* are the major, and *Potentilla fruticosa*, *Rubus Chamaemorus* and roses the minor species in the dense, low shrub layer. Sphagnum and feather mosses cover 75 to 100% of the ground. Lichen, mainly *Cladonia* and *Cetraria*, is present in small patches on flat areas but forms a significant part of the ground cover on some slopes (EC-VTMC, 1974). This wide range of plant species cannot be found all growing together, as they are dependent on environmental factors such as elevation, slope aspect, moisture, and wind conditions.

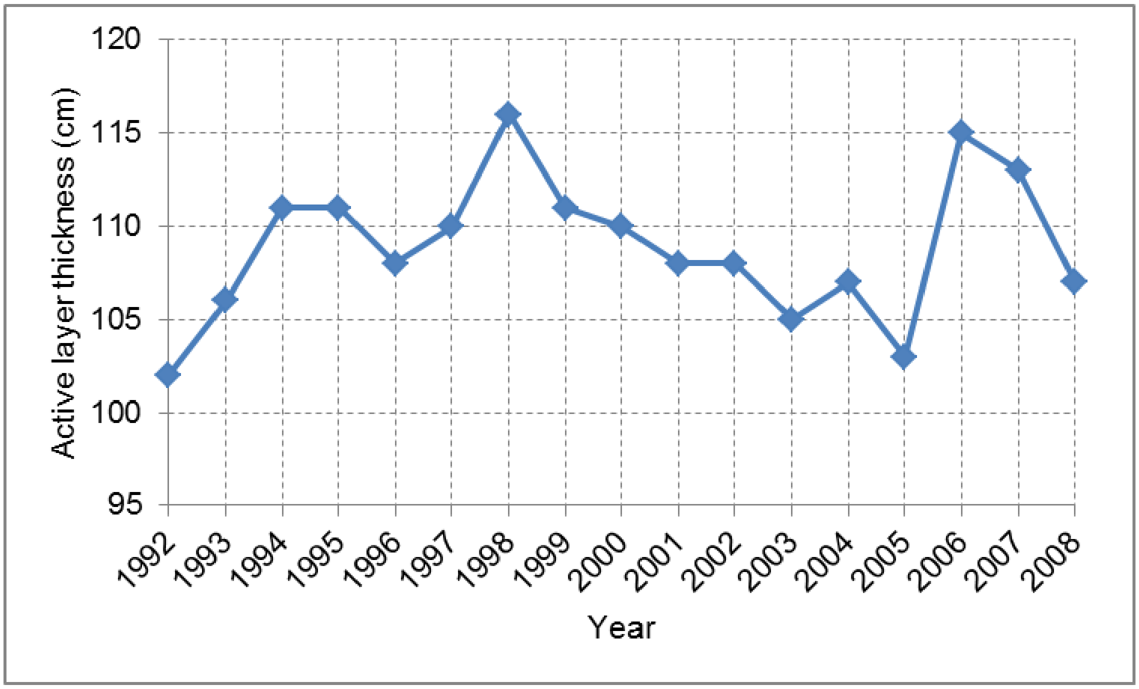

Figure 8. Active layer thickness at Rengleng River, 50km NE of Fort McPherson, 1992-2008 (CALM).

The active layer thickness on the Peel Plateau ranges from about 50 cm on vegetated surfaces in fine-grain tills or in organic deposits, to more than 100 cm in disturbed areas and gravelly floodplains. Circumpolar Active Layer Monitoring (CALM) data from Rengleng River site (ca. 50km NE of Fort McPherson) shows that the active layer thickness in the area fluctuates yearly, but a decreasing trend is observed since 1998 (Figure 8). This site was used as an approximation of the historical behaviour of the active layer in the study area as it is the closest CALM site. The decrease in active layer thickness is a result of a decrease in total degree days as demonstrated by the decreasing mean summer air temperatures (MSAT) since 1985 (Figure 5). The decrease in active layer thickness in the study area rules out any potential ionic increase caused by an increasing active layer (i.e., Keller et al., 2010).

2.2 Studied Thaw Slumps

This study focuses on two slumps that drain into Poor Man’s Creek, a small tributary of Stony Creek. These two slumps were chosen due to their accessibility from the Dempster Highway and the difference in their sizes (Figure 9).

2.2.1 Charas slump

The Charas slump (Figure 10) is located ~1.5 km north of the Dempster Highway and it is ~1 km wide. This slump is the largest, most dynamic slump in the Stony Creek Watershed and it has been active since 1944 (the oldest air photograph available).

The slump headwall is 20-30m high and contains sections of silt-rich reticulate ice, vertical ice veins passing through sections of silt, and laminated ice-rich colluvium which are all overlain by a continuous layer of till varying in thickness from ~30cm to >1m. There is also a stabilized slump area on the west side of the slump which can be distinguished by the vegetation re-colonizing the slump floor. The slump runoff extends as a massive debris flow into Poor Man’s Creek. The debris flow blocked a portion of the creek, which generated a mud-dammed lake upstream of the debris flow (Figure 9).

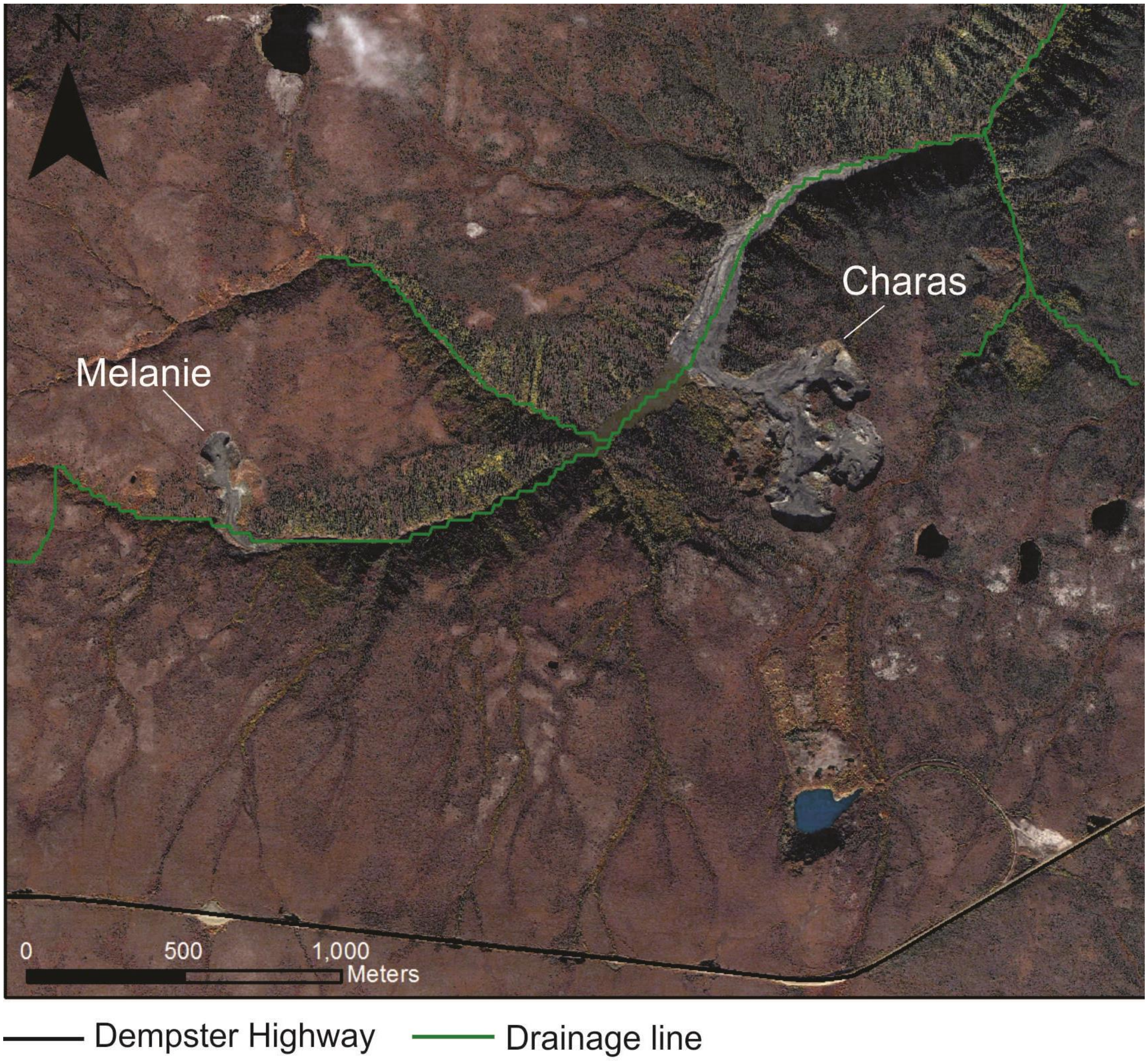

Figure 9. Quickbird image (2008) of Melanie and Charas thaw slumps in the Stony Creek watershed.

Figure 10. Oblique view from the NW of the Charas slump.

2.2.2 Melanie slump

The Melanie slump (Figure 11) is located 1.8 km west of the Charas slump, 1.3 km north of the Dempster highway and is much smaller (160 m wide) than the Charas slump. The headwall is about 15 m high, and consists of diamicton, reticulate ice and frozen diamicton. The runoff from this slump flows into the mud-dammed lake.

Figure 11. Oblique view from the south of Melanie slump.

3. METHODOLOGY

The characteristics of slump runoff and the associated impacts to the Stony Creek Watershed were assessed by sampling and analyzing i) slump runoff from two thaw slumps of different sizes (Charas and Melanie); ii) streams affected to various extents by slump runoff within the watershed; iii) streams unaffected by slump runoff (tundra streams that represent control points on natural geochemistry of the watershed; iv) ice-rich permafrost exposed in the headwall of both slumps. In addition, the geochemistry and mineralogy of suspended sediments in slump runoff and affected streams were determined.

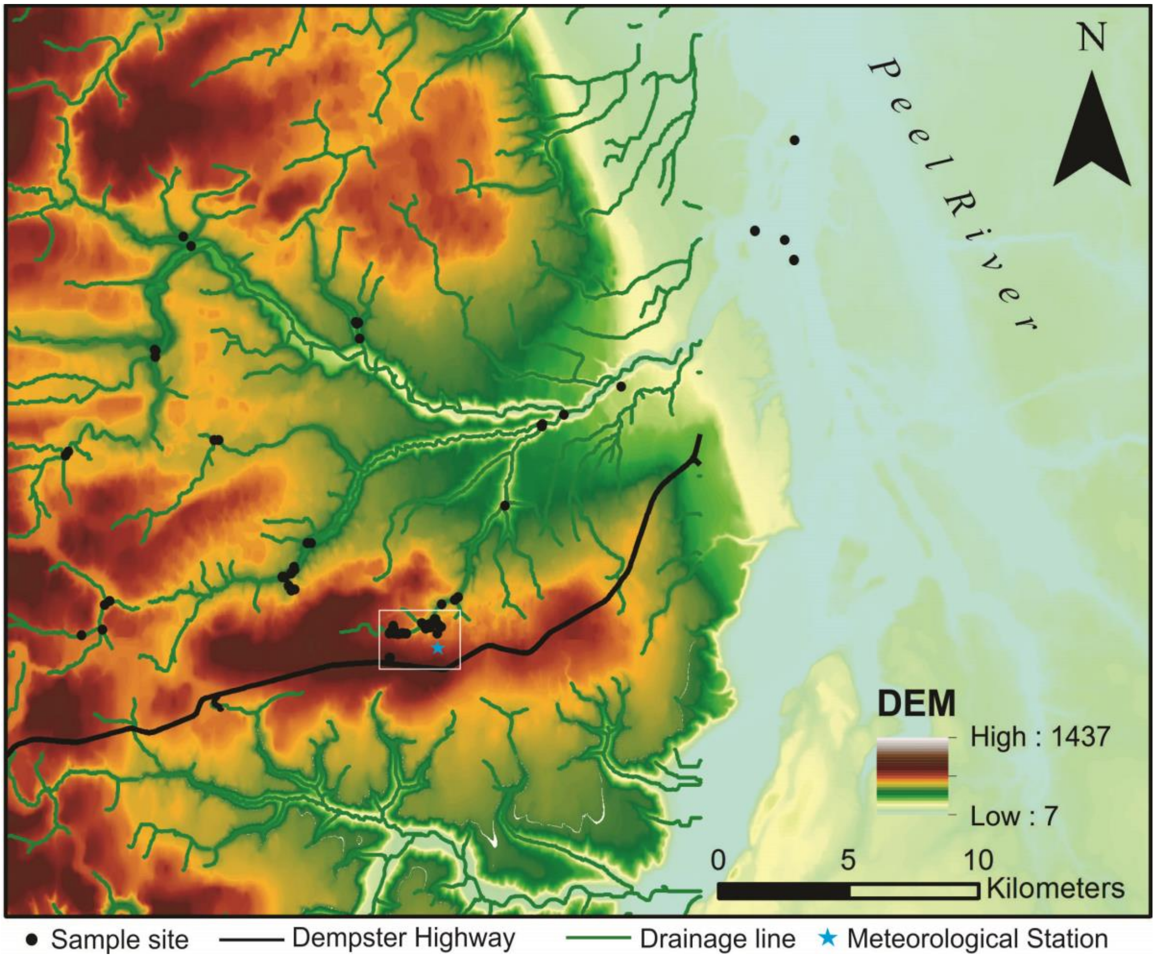

Figure 12. Digital Elevation Model (DEM) of the Stony Creek watershed showing sample locations. DEM is from National Topographic DataBase (www.geogratis.com).

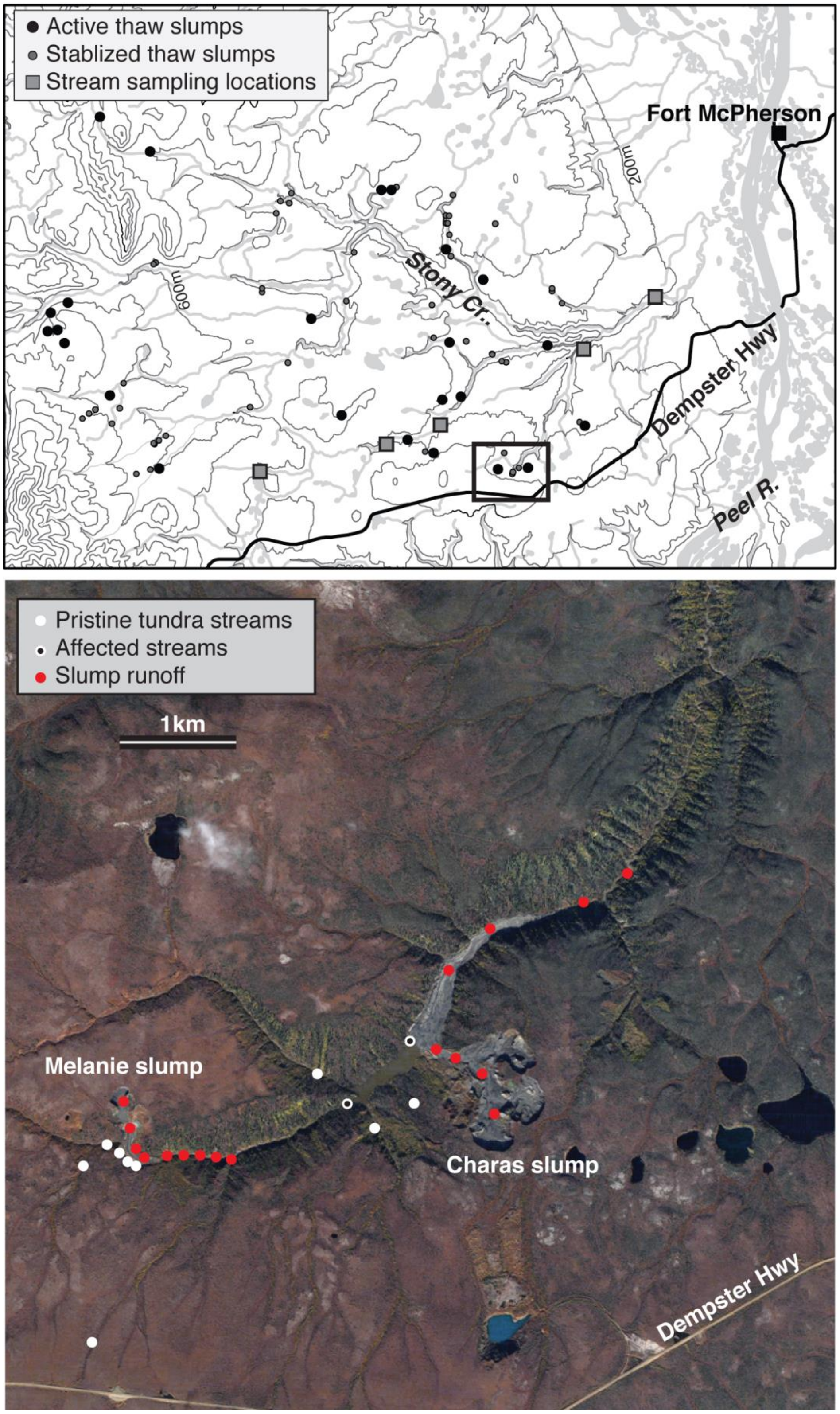

Figure 13. Quickbird image (August 2009) of two studied thaw slumps showing sample locations within and around the slumps.

3.1 Sampling of surface waters and in-situ measurements

Sample collection took place over 2-3 week periods during the months of June and August in 2010 and 2011. Slump runoff samples in 2010 (*n*=16), and 2011 (*n*=27) were collected at the base of the headwall of Charas and Melanie slumps, as well as at 3-4 locations along the mudflow, depending on its length (Figure 13). Water samples from unaffected and affected streams within the watershed were collected twice during the summer using helicopter support. Unaffected stream samples (2010: *n*=17, 2011: *n*=8) were collected at locations where there is no contribution of slump runoff to the stream and represent the background geochemistry of the watershed (Figure 13). Affected stream samples (2010: n=8, 2011: n=8) were collected in stream segments situated downstream of a slump and as such receive slump runoff contribution (Figure 13). Block samples (100 cm^3) of ice-rich permafrost exposed in the headwall of both thaw slumps were collected using an ice pick or chainsaw. The samples were melted in sealed plastic bags and yielded excess water. The excess water was filtered in HDPE bottles until analysis. A few block samples were kept frozen to perform a leaching experiment on the sediments.

At each stream sampling location, pH and conductivity were measured *in situ* using a VWR SP90M5 symphony multi-meter calibrated daily with pH 4, 7 and 10 buffer solutions. Due to their high sediment load, slump runoff samples were collected in 1L bottles and the sediments allowed to settle for up to 1 week before the supernatant water was extracted, filtered and transferred into 30 ml polyethylene bottles for geochemical analyses. Waters from affected and unaffected streams were collected unacidified from each sampling location in 30ml pre-rinsed amber polyethylene bottles after rinsing with the local water and filtered (where possible) through 0.45 µm pore diameter filters.

3.2 Aqueous geochemistry analysis

The slump runoff, stream water samples and melted ice-rich permafrost were analyzed for major ions. Cation (Al_{tot}, As_{tot}, Ba^{2+}, Ca^{2+}, Fe_{tot}, Mg^{2+}, Mn_{tot}, Na^{+}, K^{+}, Si^{4+}, and Zn^{2+}) concentrations were determined on acidified samples (pH 2) using a Vista-Pro simultaneous charge coupled device (CCD) detector Inductively Coupled Plasma Optical Emission

Spectrometer (ICP-OES) at the University of Ottawa. The anion (SO_4^{2-} , NO_3^- and Cl^-) concentrations were determined by ion chromatography (Dionex ICS-2100). Select samples were run in duplicate to ensure precision during the analysis with analytical reproducibility of 5%.

Alkalinity titrations were performed in the field using a Hach® Digital titrator kit to the pH endpoint (<4.3). Alkalinity was then calculated from Gran titration plot using the following equation:

$$alk_T\ ({}^{eq}/_{kg}) = \frac{V_{acid}(ml) \cdot\ N_{acid}\ ({}^{eq}/_{kg})}{V_{sample}\ (ml)}$$

Where V_{acid} is the volume of acid added in the titration; N_{acid} is the normality of the acid used, and V_{sample} is the volume of the sample being titrated for alkalinity.

3.3 Stable isotopes ($^{18}O/^{16}O$ and D/H)

The $^{18}O/^{16}O$ and D/H ratios of melted ice samples were determined using a liquid water analyzer (Los Gatos Research Liquid water analyzer model 908-0008) at the University of Ottawa. The liquid water analyzer instrument uses off-axis integrated cavity output spectroscopy (OA-ICOS) and relies on spatial separation of reflections from highly reflective mirrors installed within the optical cavity. The OA-ICOS liquid water analyzer was coupled to a CTC LC-PAL autosampler for simultaneous $^{18}O/^{16}O$ and D/H ratio measurements of H_2O. All measured water samples were calibrated and normalized to internal laboratory water standards that were previously calibrated relative to VSMOW using conventional IRMS systems. Consequently, results are presented using the δ-notation ($\delta^{18}O$ and δD), where δ represents the parts per thousand differences for $^{18}O/^{16}O$ or D/H in a sample with respect to Vienna Standard Mean Ocean Water (VSMOW). Analytical reproducibility for $\delta^{18}O$ and δD is ±0.3 and ±1 respectively. The complete measurement procedure and performance of the liquid water analyzer is described in Lis et al. (2008).

3.4 Sediment sampling and analysis

The sediments recovered from the slump runoff and affected streams were analyzed for particle size distribution, geochemistry and mineralogy.

3.4.1 Particle size analyzer

The particle size distribution of select sediment samples in the debris flow (*n*=8) was determined using a Microtrac S3500 laser particle size analyzer at the University of Ottawa. Prior to analysis, 50ml Falkan tubes were filled to the 10ml mark with sediment, and then to the 45ml mark with a solution of 0.08M sodium hexametaphosphate. This mixture was left in suspension for 5 days. Prior to analysis, each sample was placed on a vortex mixer for 2 minutes, before being diluted into a 250mL beaker of tap water and continuously stirred with a mixer. The sample aliquot was extracted from a consistent depth with an eyedropper, introduced into the sample chamber where the eyedropper was then rinsed 3 times. Each sample is analyzed 3 times, for an average grain size in µm.

3.4.2 Leaching Experiment

Suspended sediments collected in the slump runoff were used in leaching experiments in an effort to determine which process drives the geochemical evolution of the slump runoff as it travels over the mudflow. The experiment was performed twice, with slightly different water extraction intervals. The first experiment was performed with 3 sediment samples (11-LM-23, 11-LM-46, 11-LM-61) that were oven dried and slightly crushed to silt-sized particles before starting the experiment. Ten grams of each sample were weighed into 50ml centrifuge tubes, and 50 ml of distilled water was added. Samples were allowed to leach for 1, 3, 19, 24, 28, and 35 days. For the second experiment, 11-LM-60 was added to the above samples, making a total of 4 samples analyzed in the second experiment. These samples were allowed to leach for intervals of 7, 14, 21, and 28 days. The leached waters were then analyzed by ICP-OES to determine the concentration of major ions.

3.4.3 X-ray Fluorescence

Select sediment samples (*n*=4) were also analyzed by a Philips PW2400 X-Ray Fluorescence (XRF) with a Rh tube and 30 position sample changer (Philips PW 2510) at the University of Ottawa. Philips SuperQ/Quantitative and SemiQ/Qualitative software (ver. 2.1D) control the instrument and quantitative analysis of samples. Samples were crushed with an agate mortar and pestle into a fine powder and prepared with a Claisse Fluxer for fused disks and a Carver press for pressed pellets.

3.4.4 X-Ray Diffraction

Powder X-ray diffraction (XRD) was performed to determine the specific mineralogy of the sediment (n=9). More specifically, the goal was to detect the presence of soluble sulfate minerals including gypsum, anhydrite and selenite. The samples were prepared by grinding them into a fine powder with an agate mortar and pestle. The XRD is a Philips double goniometer X'Pert system which can be used with an Anton Parr low temperatures (~80 to 575 K) or high temperatures (up to 1300 °C) cameras. The analysis was set with a scan step of 1s and step size 0.02 [°2θ.]. Measurements were carried out between 10° and 85° and at 40v/45mA, on a continuous goniometer scan with the sample mount spinning. A long scan was performed on sample 11-LM-60 to try to better detect the presence of gypsum. This scan was performed with a scan step time of 5s, and step size of 0.01[°2θ.]. Measurements were carried out between 5° and 85°. Five gypsum standards were also prepared to assess the presence of a gypsum signature at different concentrations. The standards included a 100% gypsum sample, as well as 0.5%, 1%, 2% and 5% gypsum concentrations mixed with quartz.

3.4.5 Scanning Electron Microscopy

The potential presence of pyrite and sulfate minerals in the ice-rich permafrost (originating from the shales) prior to thawing, and the geochemical modification between frozen and thawed sediments was also investigated. A block sample of frozen ice-rich permafrost was sublimated in a commercial freeze-dryer. The residual sediments, as well as oven dried suspended sediments from the debris flow, were investigated by a Jeol 6610LV Scanning Electron Microscope (SEM) with an Oxford Inca large area SSD detector for qualitative chemical analysis by energy dispersive x-ray spectrometry (EDS) at the University of Ottawa. Imaging was done in both backscattered electron (BSE) mode and secondary electron (SE) mode. For analysis, samples were mounted on sample holders by placing the material directly onto carbon tape, and were carbon coated.

3.5 Mixing calculations

Mixing calculations were performed using 2 end member mixing. The two end members were that of slump runoff, and unaffected water. The slump runoff sample with the highest value of SO_4/Cl was chosen for the calculations using SO_4/Cl as the tracer.

The relative fractions of each end member in the affected waters are defined as follows:

$f_{1\,(SR)} + f_{2\,(US)} = 1$ = Affected streams (AS)

where SR = slump runoff and US = unaffected streams.

To solve for $f_{(SR)}$ and $f_{(US)}$, a solute mass balance equation was used with the SO_4/Cl tracer.

$$f_{(US)} = \frac{SO_{4\,(SR)} - SO_{4\,(AS)}}{SO_{4\,(SR)} - SO_{4\,(US)}} \quad \text{and } f_{(SR)} = 1 - f_{(US)}$$

4. RESULTS

The results are presented in four sections. The first section presents the aqueous geochemistry results of the ice-rich permafrost. The second section presents the aqueous geochemistry results of the slump runoff and streams including *in situ* measurements, stable isotopes and major ion geochemistry. The third section presents the characteristics of the suspended sediments from each slump including sediment load, particle size analysis and geochemical composition. The fourth and final section presents the results of a leaching experiment performed on the suspended sediments of select Charas samples, including XRD, SEM imaging and analysis and PHREEQC modelling, to shed light on geochemical evolution in the slump runoff component.

4.1 Aqueous geochemistry: ice-rich permafrost exposed in headwalls

A Schoeller diagram of the average major ions chemistry of the various ice-rich permafrost units exposed in the headwall of both slumps shows the same relative proportions of soluble ions between different units (Figure 14). The dominant ions are SO_4^{2-}>Ca^{2+}>Mg^{2+}>Na^+, with very low amount of Fe_{tot} and HCO_3^-. At the Charas slump, five different ice-rich permafrost units were sampled and the chemical facies is similar between all units. However, a distinction is observed between the units based on absolute solute concentration. The reticulate dirty ice units (i.e., reticulate ice, ice-rich diamicton) have the highest concentration of solutes (i.e. TDS= 3328 mg/L), whereas the massive ice unit (i.e., ice vein) has the lowest (i.e. TDS = 1240 mg/L). The concentrations of SO_4^{2-}, Ca^{2+} and Mg^{2+} in the dirty ice units are up to five times higher (average SO_4: 1915 mg/L) than massive ice units (average SO_4^{2-}: 401 mg/L) (Figure 15). Complete ice chemistry results are presented in Appendix A.

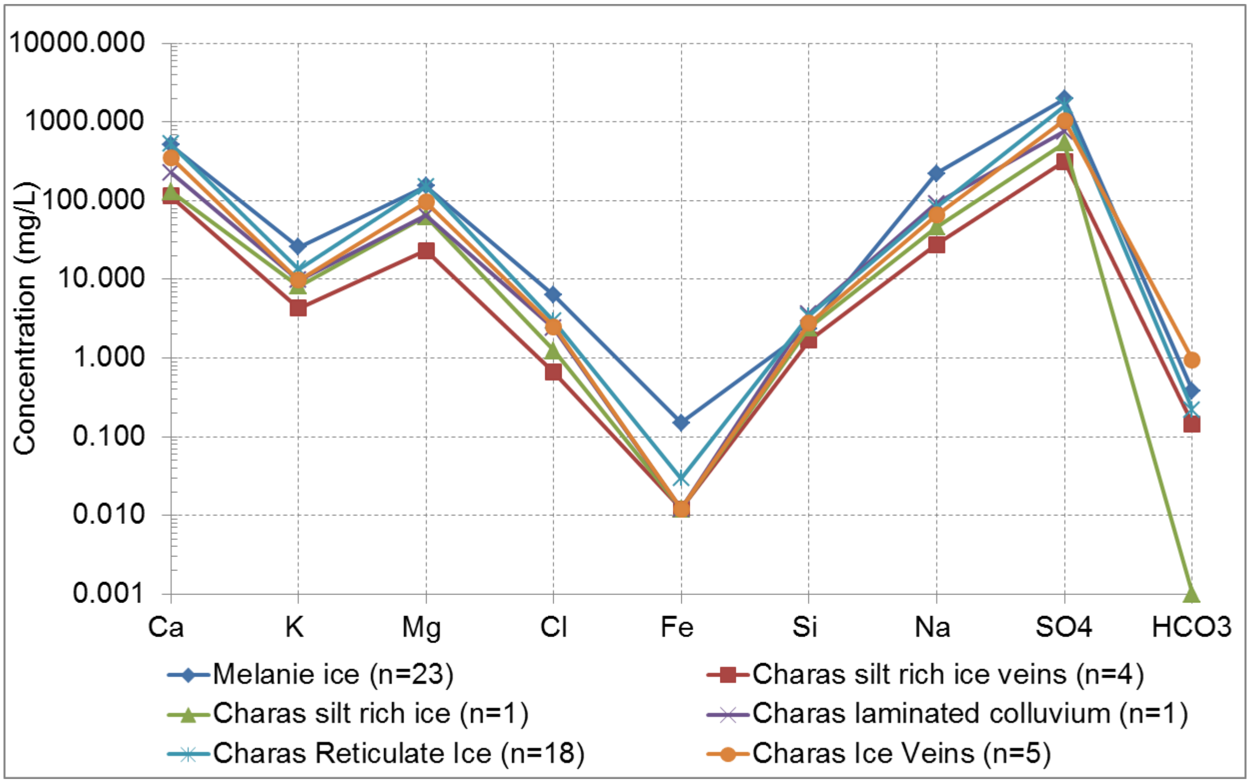

Figure 14 Schoeller diagram of ice chemistry for Melanie ice composition, and different types of Charas ice. Fe is below detection for Charas silt rich ice vein, Charas laminated colluvium and Charas silt rich ice, but is plotted as 0.001 to be shown on graph.

4.2 Aqueous geochemistry: slump runoff and streams

In situ measurements of labile parameters, including pH and conductivity, allow for an initial characterisation of the slump runoff and affected and unaffected streams. The pH values for the three groups range between 5.5 and 8.5 (Figure 16) and no statistical differences (t-test) is observed in the average value (Table 1). There exist a few outliers with pH values near 4.5 and these were collected from streams in June receiving contribution from melting late-lying snowpatch. There is also an outlier within the values of the Melanie slump. 11-LM-74C has a pH value of 5.78 and was collected on a cold, drizzly day when the melting of the headwall was minimal, and runoff movement slow, allowing for more influence by rainfall. With the exception of this outlier within the slump runoff samples, both Charas and Melanie exhibit a relatively narrow distribution, when compared to the unaffected and affected streams.

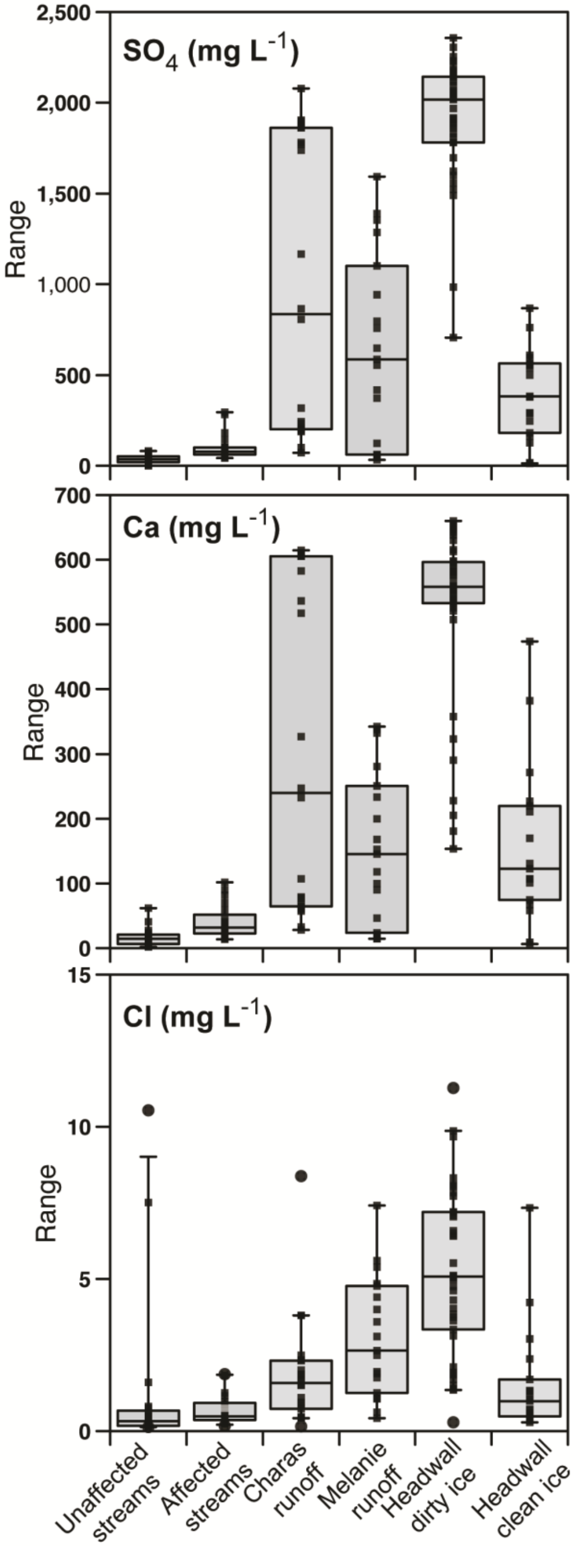

Figure 15. Box and Whisker plots for SO_4^{2-}, Ca^{2+} and Cl^- concentrations in stream water and ice samples.

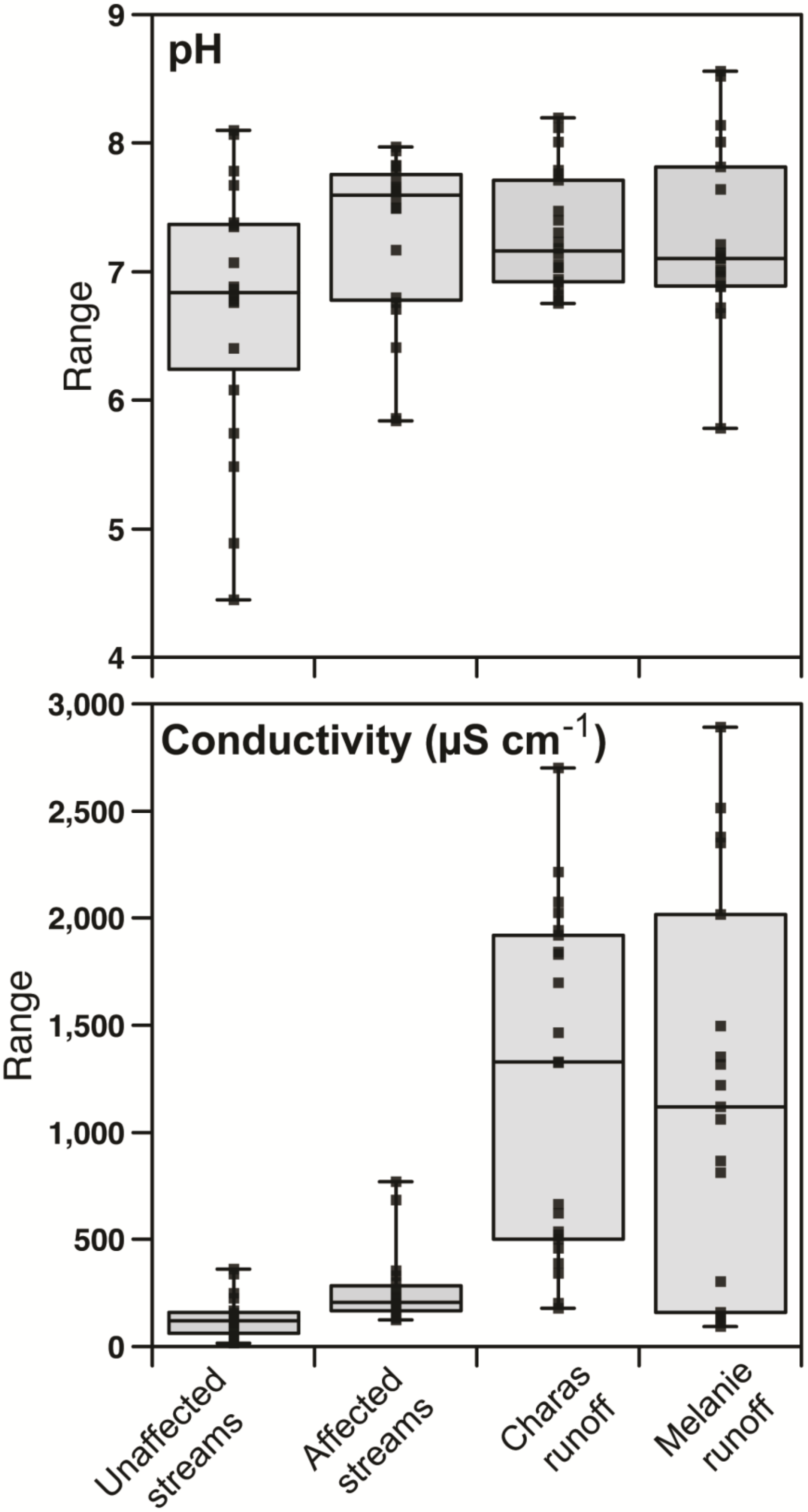

Figure 16. Box and Whisker plots for pH and conductivity of slump runoff and stream samples.

Conductivity is one of the most recognizable characteristics of the slump runoff from both Charas and Melanie slumps (Figure 16). The mean conductivity for slump runoff (Charas=1217 µS/cm and Melanie=1176 µS/cm) is nearly an order of magnitude greater than the mean for unaffected streams (135 µS/cm). The conductivity of affected streams reflect variable contribution of slump runoff and unaffected waters (up to 770 µS/cm). A t-test analysis indicates that the conductivity of the slump runoff (both Charas and Melanie slumps) is significantly different ($p<0.001$) from that of affected and unaffected streams (Table 1). No statistical difference exists between the average conductivity values of affected and unaffected streams ($p=0.017$) (Table 1).

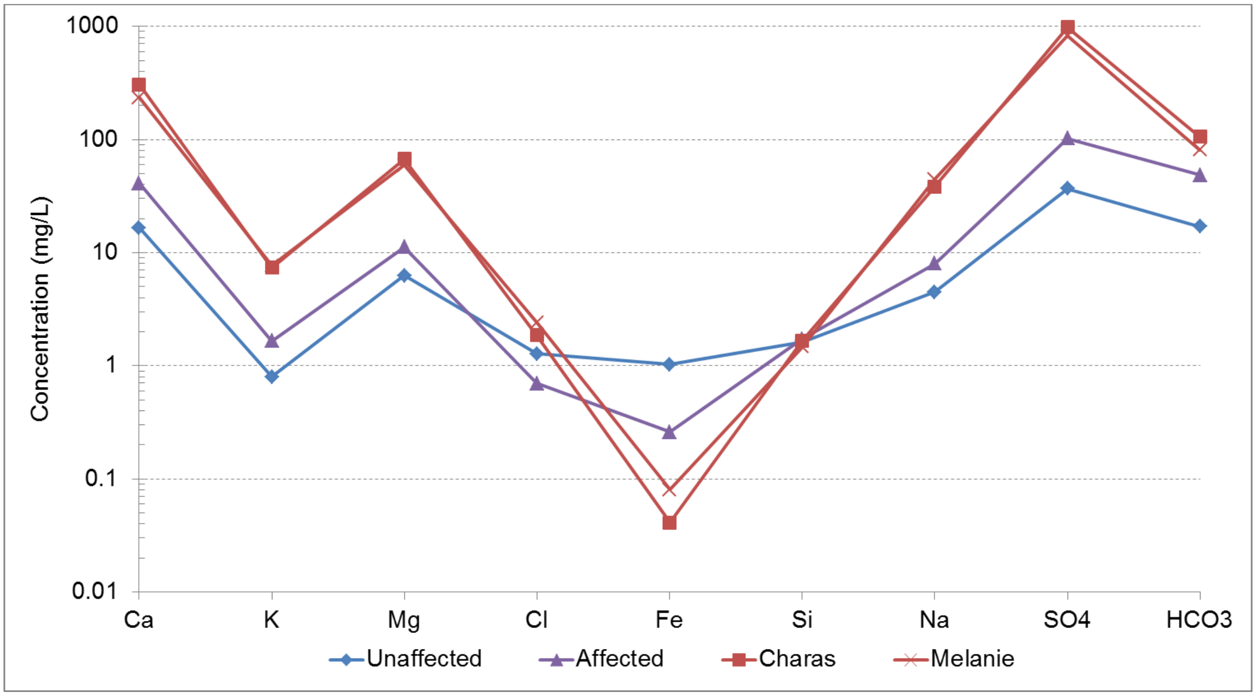

Figure 17. Schoeller Diagram of average major ion chemistry for Charas and Melanie slumps, unaffected and affected water.

Table 1 Results of t-test for each water category and several parameters

pH	*Unaffected streams*	*Affected streams*	*Charas runoff*
Affected streams	0.084		
Charas runoff	0.016	>0.5	
Melanie runoff	0.069	>0.5	>0.5
Conductivity	*Unaffected streams*	*Affected streams*	*Charas runoff*
Affected streams	0.017		
Charas runoff	**< 0.001**	**<0.001**	
Melanie runoff	**< 0.001**	**<0.001**	>0.5
SO4	*Unaffected streams*	*Affected streams*	*Charas runoff*
Affected streams	0.003		
Charas runoff	**<0.001**	**<0.001**	
Melanie runoff	**<0.001**	**<0.001**	0.045
Ca	*Unaffected streams*	*Affected streams*	*Charas runoff*
Affected streams	0.003		
Charas runoff	**<0.001**	**<0.001**	
Melanie runoff	**<0.001**	**<0.001**	0.005
Cl	*Unaffected streams*	*Affected streams*	*Charas runoff*
Affected streams	0.361		
Charas runoff	0.441	0.014	
Melanie runoff	0.008	**<0.001**	0.077
Suspended sediments	*Unaffected streams*	*Affected streams*	*Charas runoff*
Affected streams	0.244		
Charas runoff	**<0.001**	**<0.001**	
Melanie runoff	**<0.001**	>0.5	**<0.001**
SO4/Cl	*Unaffected streams*	*Affected streams*	*Charas runoff*
Affected streams	0.153		
Charas runoff	**<0.001**	0.007	
Melanie runoff	0.303	0.338	**<0.001**

The similarity in the profiles of the geochemical composition of the unaffected, affected and slump runoff samples reflects the general homogeneity in the composition of the exposed ice-rich headwalls and ice-rich till deposits that blanket much of the study basin (Figure 4). With the exception of Fe_{tot}, where its concentration is highest in unaffected streams, the slump runoff has the highest concentration of specific dissolved solutes and unaffected streams have the lowest; the affected streams have intermediate concentrations due to the contribution of slump runoff (Figure 17). The slump runoff values are in most cases an order of magnitude higher than the values of the unaffected streams. The concentrations of the dominant major ions, SO_4^{2-}, Ca^{2+} and Mg^{2+}, of each water type, are one order of magnitude higher in slump runoff than in unaffected streams (Figure 17, Figure 15). This suggests that SO_4^{2-} and Ca^{2+} are the dominant ions released during the thaw and subsequent weathering of shale-rich tills. A t-test indicates that a statistically significant difference exists in the concentration of SO_4^{2-}, and Ca^{2+} between slump runoff and unaffected and affected streams (Table 1). By contrast, variations in Cl^- concentration, a conservative ion, between the three groups shows no statistical differences (Table 1).

Stable isotopes proved to be another useful tool in distinguishing between slump runoff, affected and unaffected streams. The $\delta^{18}O$ and δD values range from -24.6 to -20.3 and -188.6 to -157.6 for the unaffected streams respectively, -22.9 to -19.1 and -179.5 to -153.9 for affected streams, -27.4 to -21.2 and -219.5 to -159.7 for the Charas slump and -29.3 to -20.0 and -234.6 to -159.8 for the Melanie slump. The isotopic values for the slump runoff plots closer to the ice than unaffected and affected streams, which is expected as the runoff hasn't been affected by evaporation or mixing this close to the headwall (Figure 18). The unaffected and affected waters plot along the local meteoric water line for Fort Smith, NT as these waters are influenced by precipitation. Unaffected and affected samples and are more enriched in $\delta^{18}O$ and δD compared to the ice and slump runoff. The variation in isotopic content of the slump runoff can also be attributed to the mixing that occurs in the mudflow with unaffected streams as it reaches the end of the mudflow.

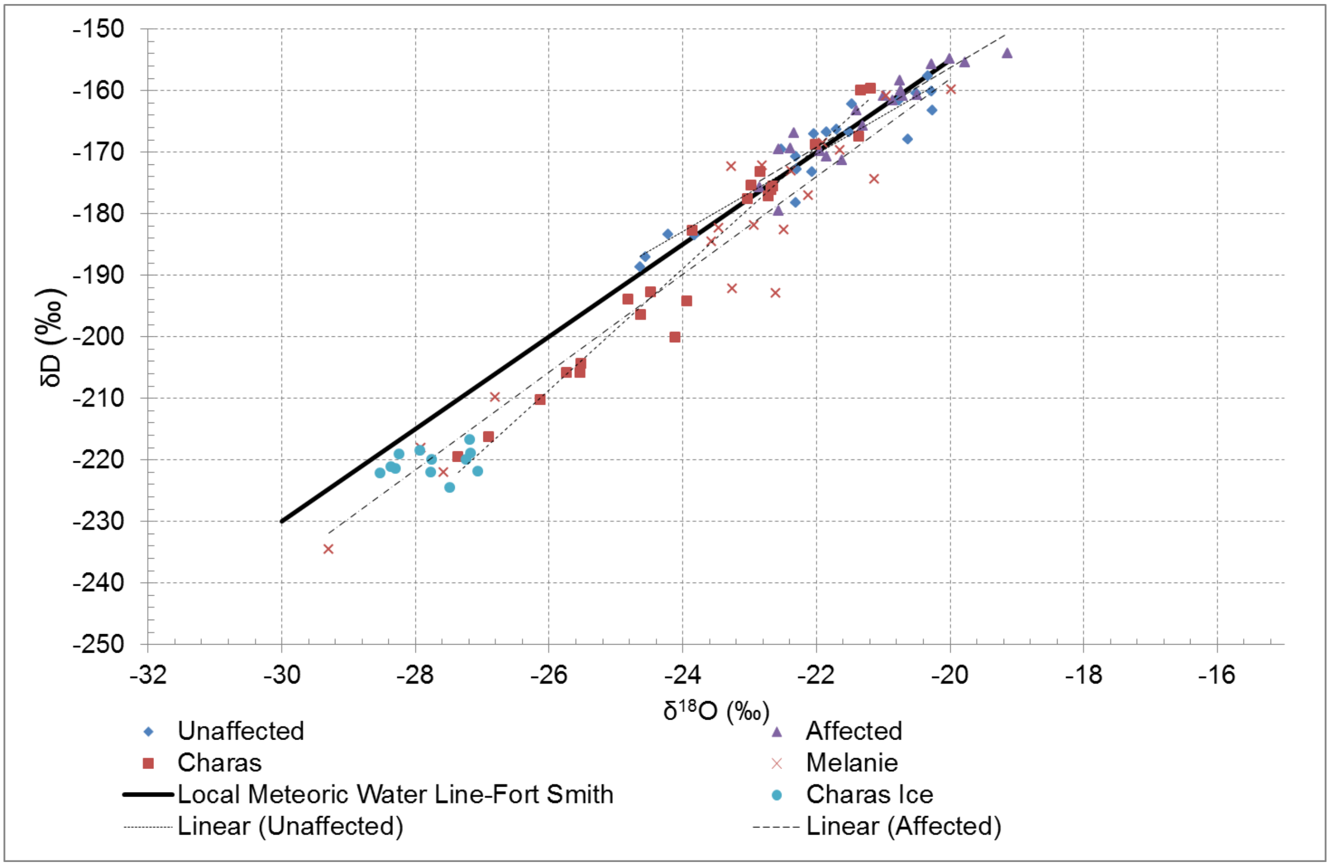

Figure 18. Co-isotope diagram of unaffected streams, affected streams, and slump runoff from the Melanie and Charas slumps plotted with ice samples collected from the Charas headwall in 2011 and the Local Meteoric Water Line for Fort Smith, NWT ($dD=7.5d^{18}O-4.9$).

The geochemical evolution of dissolved ions along the two mudflows varies with increasing distance from the headwall (Figure 19). Within the Charas mudflow, the conductivity and concentration of dissolved ions increases from the headwall to approximately halfway down the mudflow and then begins to decrease with distance (Figure 19). At increasing distance from the headwalls, unaffected stream water mixes with and dilutes the slump runoff, thus decreasing the conductivity of the slump runoff. By contrast, an increase in conductivity and dissolved ions is not observed at the Melanie mudflow (Figure 19). This may be because the Melanie mudflow is only 800 m long compared to 2041 m at Charas, and the runoff does not travel along the mudflow very far before receiving the addition of unaffected water.

Assuming that the only slump runoff contribution is coming from the Charas and Melanie slumps, a similar trend is observed in the geochemical evolution of dissolved ions from the Charas mudflow to the Peel River situated 22 km downstream (Figure 19). As the distance downstream of the Charas mudflow increases towards the Peel River, conductivity decrease gradually until it levels off at 10 km to ~200 µS/cm, which is still higher than the average conductivity of unaffected streams (135 µS/cm) even at 22 km downstream of the slump. A comparable trend is also observed for SO_4^{2-} concentration, where it measures 2078 mg/L at the headwall and decreases to 183 mg/L at a point 6 km away (Figure 19). At the confluence of Stony creek with the Peel River, the concentration of SO_4^{2-} has levelled out at 100 mg/L, which is still more than double the average concentration of unaffected waters (36.8 mg/L) (Figure 19). A slight increase in concentrations can be seen downstream of the confluence due to inputs from other affected streams in the watershed. Appendix B presents complete geochemistry results for slump runoff and stream samples.

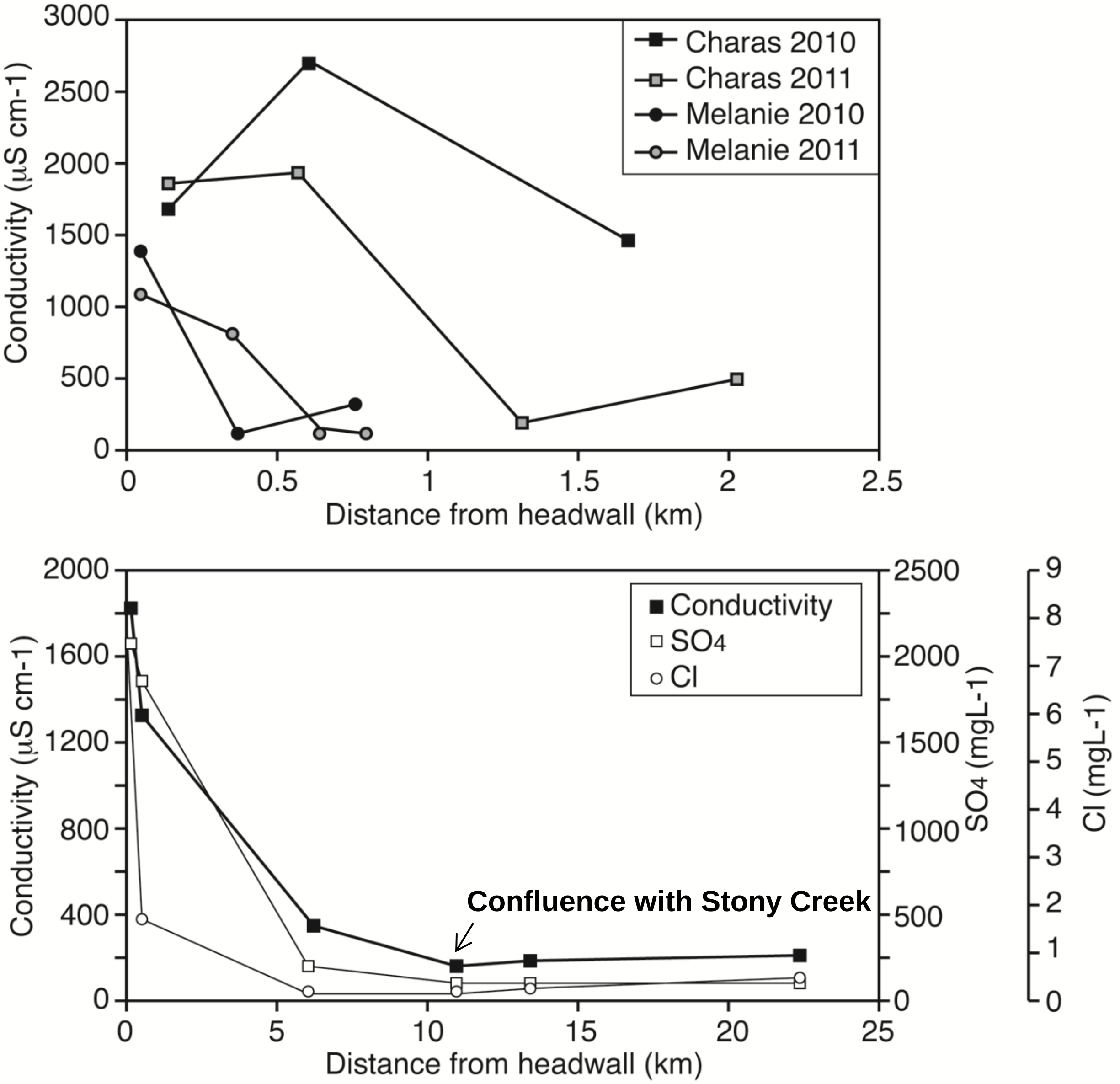

Figure 19. Geochemical evolution shown by conductivity on the slump scale (top) and by major ion chemistry on the watershed scale (bottom).

4.3 Aqueous geochemistry: saturation indices

The pH and geochemical composition of the waters were entered into PHREEQC, a hydrogeochemical program (Parkhurst and Appelo, 1999), to calculate the mineral saturation index. Using this program to model aqueous solutions allows for the determination of which minerals may be precipitating/dissolving in solution given the environmental conditions and the composition of the sample. Modelling of the the ice-rich permafrost units was performed at 0°C, whereas for the streams, modeling was performed at the measured temperature (5-10°C). The solution is undersaturated if SI is <1, at equilibrium if SI=1, or supersaturated if SI>1.

In the ice-rich permafrost samples, barite (SI=0.31), gypsum (SI=-3.05) and anhydrite (SI=-3.30) are predicted to be undersaturated, whereas Fe-hydroxides are oversaturated (amorphous Fe(OH) SI=1.50, goethite SI=6.46). For the slump runoff, barite (SI= 0.59), gypsum (SI= -2.69) and anhydrite (SI= -0.19) are all undersaturated. Since the Fe_{tot} concentrations were below the detection limit for most stream samples, saturation indices were not given for Fe-minerals. Since the Fe-hydroxides are predicted to be oversaturated in the thawing ice-rich permafrost samples, and because of the pH conditions of the water, Fe^{3+} will precipitate predominantly as $Fe(OH)_3$, which supports the low Fe concentrations in the stream samples.

4.4 Suspended sediments

Particle size analysis showed that sediments transported in Charas and Melanie slump runoff consists of well sorted silt. The average particle size at Charas was 22.3 µm and the one sample analyed from the Melanie site had a grain size of 12.3µm. The well sorted nature of the sediment is expected due to its transportation in water. Table C1 in Appendix C presents the complete results of the particle size analysis.

The suspended fine sediment load is a characteristic parameter of both the Charas and Melanie slump runoff compared to unaffected streams (Figure 20). The suspended sediment of the slump runoff can reach up to 911 g/L, whereas it is generally less than 0.1 g/L in unaffected streams (Figure 20). In affected waters, the suspended sediment load is one to three orders of magnitude higher than in unaffected waters and varied diurnally by up to an order of magnitude and followed the patterns of net radiation and ground ice ablation in thaw slumps (Kokelj et al., 2013). The influence of the slump runoff sediment load is the most visible effect on unaffected water, making it easy to identify streams that have potentially been affected by slump runoff (Figure 21). The slight increase in suspended sediments that is seen between 13 km and 22 km can be explained by the possible contribution of other sediment sources in the stream, as well as other slump activity upstream of the studied slumps.The suspended sediment load of the affected streams downstream of the Charas slump drops off significantly at a distance of ~ 10 km from the headwall, and levels out at ~ 9 g/L. Suspended sediment load does not recover to unaffected levels (<0.1 g/L), even at a distance of 22 km from the headwall (Figure 22).

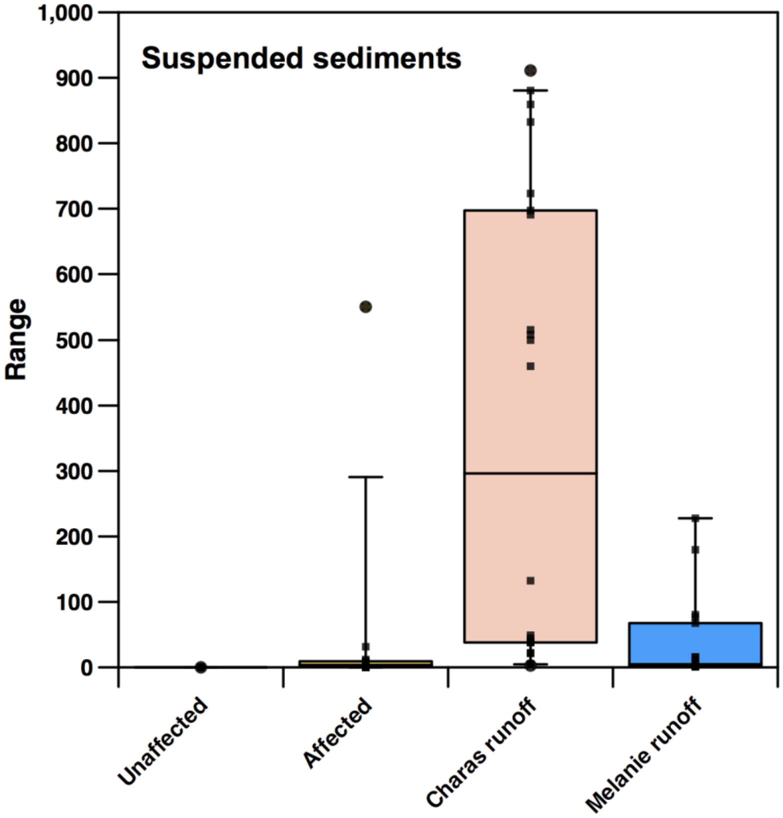

Figure 20. Box and Whisker plot of sediment load for different water sample types. Unaffected samples with negligible sediment load (n=19) are plotted at 0.01 g/L.

Figure 21. (A) Typical stream affected by slump runoff (B) typical unaffected stream.

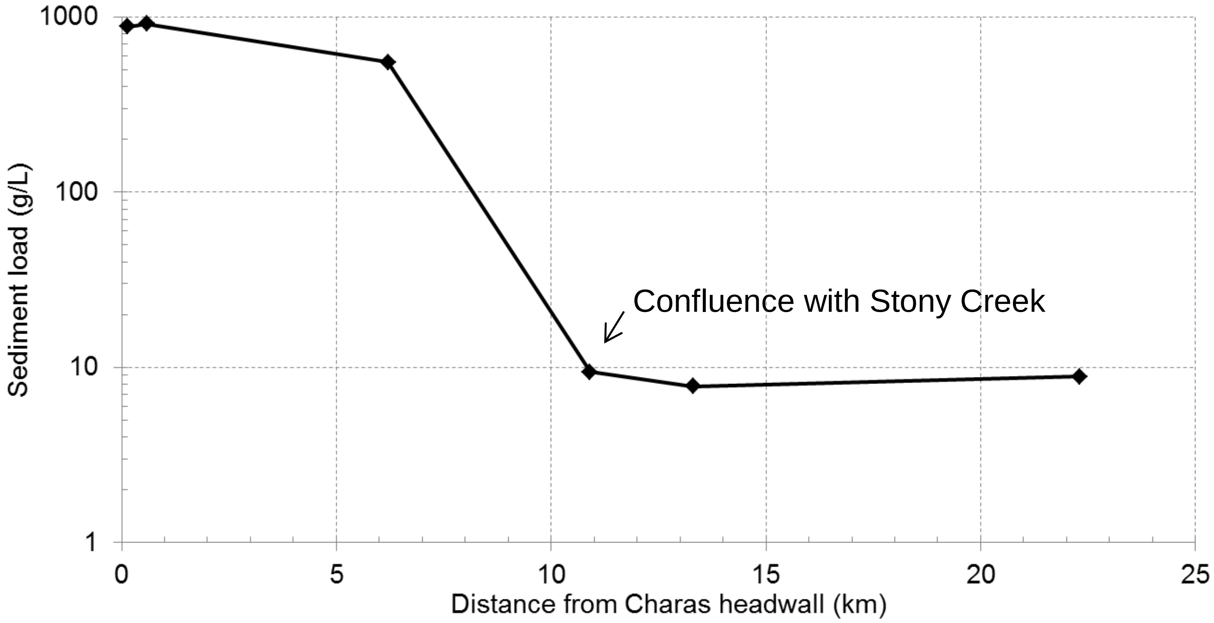

Figure 22. Sediment load with distance from Charas headwall to the confluence of Stony Creek with the Peel River.

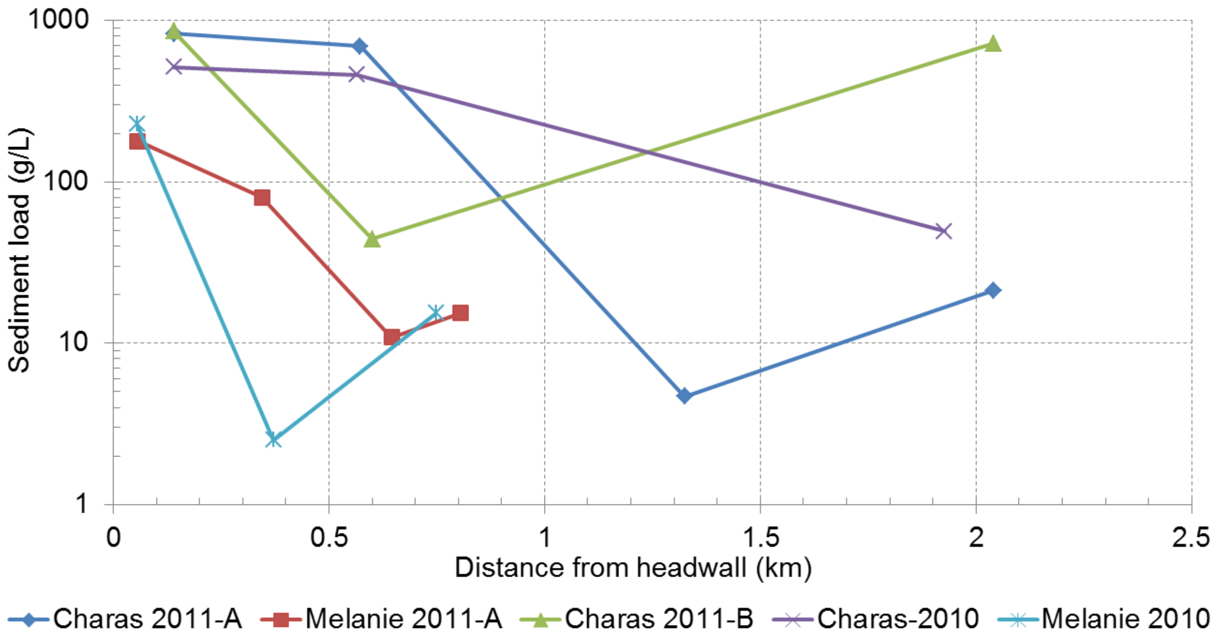

Figure 23. Sediment load from the headwalls of Charas and Melanie slump to the end of their respective mudflows for transects taken in 2010 and 2011.

Similar to the conductivity, the sediment load of slump runoff also varies along the mudflow (Figure 23). There is, however, much more variation in the sediment load between different transects than is seen in the conductivity measurements. The sediment load is affected by the addition of low sediment load unaffected waters, as well as the rate of melting and velocity of the runoff. The sediment loads in the Charas runoff are up to 5 times higher than those of Melanie suggesting that the size of the slump can also influence sediment load (Figure 23). The low points in the profiles indicate the areas of maximum unaffected water contribution. This dilutes the slump runoff, resulting in a decrease in the concentration of suspended sediments. As the runoff continues to flow down the mudflow, it carves channels into the hardened mud of the mudflow. This erosion, caused by the runoff, increases the sediment load as the runoff flows to the end of the mudflow. These same trends are seen in the Melanie slump (Figure 23).

The XRD spectra of sediments contained in the ice-rich headwalls and along the mudflows indicate identical mineralogy between Charas and Melanie slump samples (Figure 24). The mineralogy at different locations along the mudflow are also identical. The major mineralogy consists of quartz, muscovite, ferroan clinochlore and albite. The geochemistry of sediments of both slumps is dominated by SiO_2, AlO_2 and Fe_2O_3 (Figure 25 and Figure 26), which supports the XRD analysis. With the exception of CaO, little variation in the concentration between the samples from the two slumps is observed, which again reflects the general homogeneity in the composition of the till deposits that blanket much of the study basin. Complete XRF results are shown in Table C2 of Appendix C.

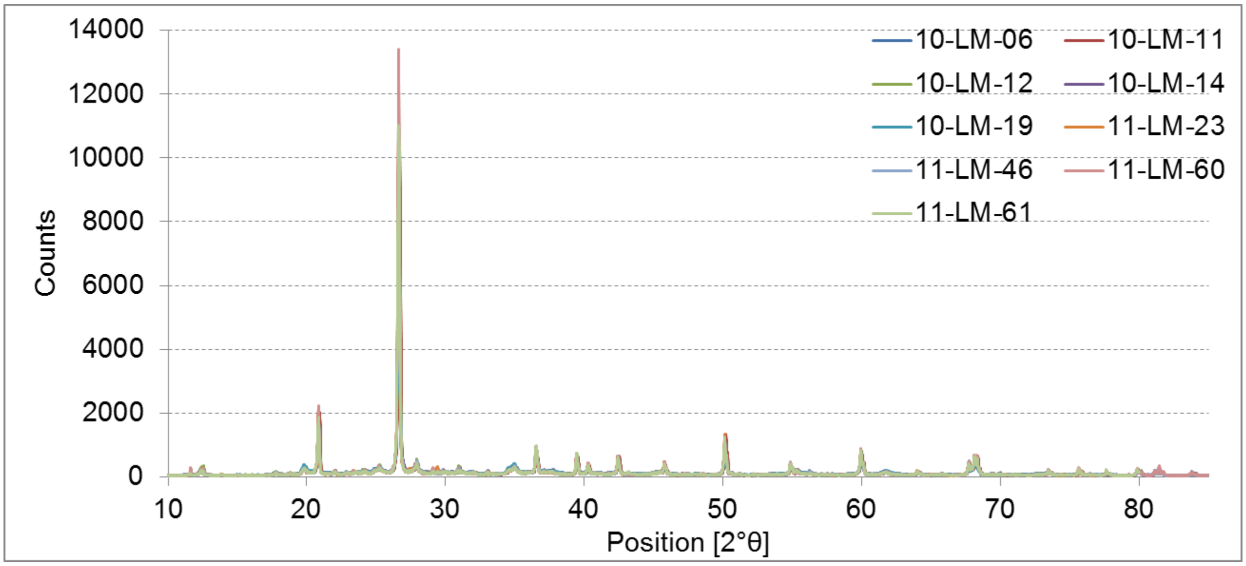

Figure 24. XRD spectra for suspended sediments from both the Charas (10-LM-06, 11, 12, 11-LM-23, 46, 60, 61) and Melanie slump (10-LM-14, 19).

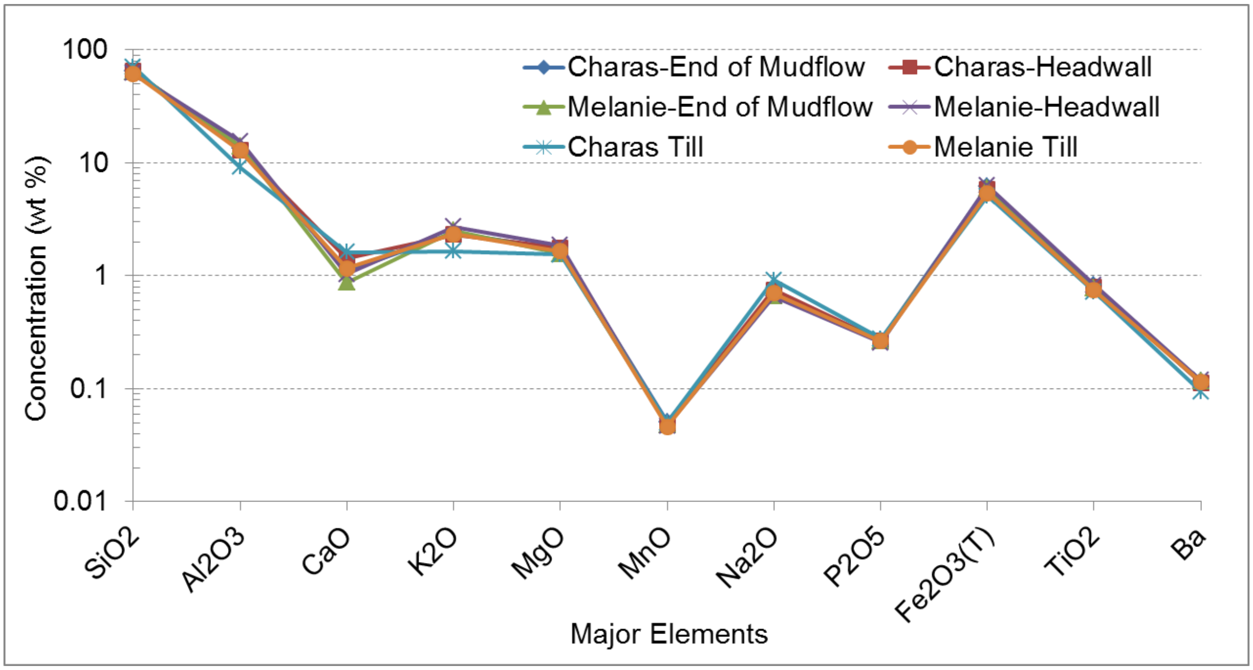

Figure 25. Major element concentrations of suspended slump runoff sediments, analyzed by XRF.

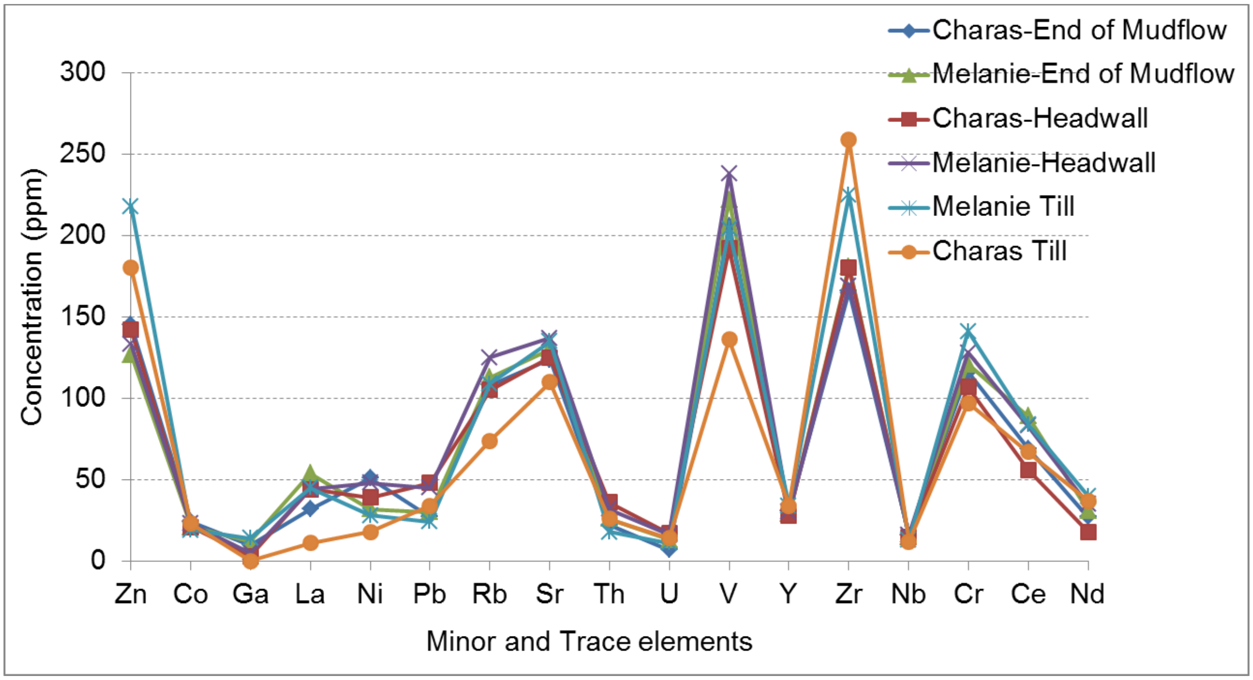

Figure 26. Minor and trace element concentrations of suspended slump runoff sediments, analyzed by XRF.

The SEM imaging and EDS analysis revealed the presence of framboidal pyrite (Figure 27), barite, Fe-hydroxides, mica, and quartz in the ice-rich permafrost exposed in the headwall and suspended sediment samples from the Charas thaw slump (Figure 28). The framboidal pyrite is covered in a thin layer of organics, which gives it the appearance of being in an organic sac and is therefore post-depositional (Figure 27). The Fe-hydroxides showed a texture similar to the framboidal pyrite (Figure 29). Euhedral-subhedral barite crystals were found in all samples, which explains the high concentrations of Ba detected in the XRF analysis. However, due to the insoluble nature of barite ($Ksp=10^{-10}$) it is not likely to be the source of SO_4^{2-} found in the slump runoff waters and the concentration of Ba in our stream samples was low (maximum 0.06 mg/L). None of the samples analyzed by SEM showed any anhydrite or gypsum crystals and compositional mapping revealed no zones where high Ca^{2+} correlated with high S. This is attributed to the high solubility of gypsum ($Ksp=10^{-4.60}$) and anhydrite ($Ksp=10^{-4.50}$) in water.

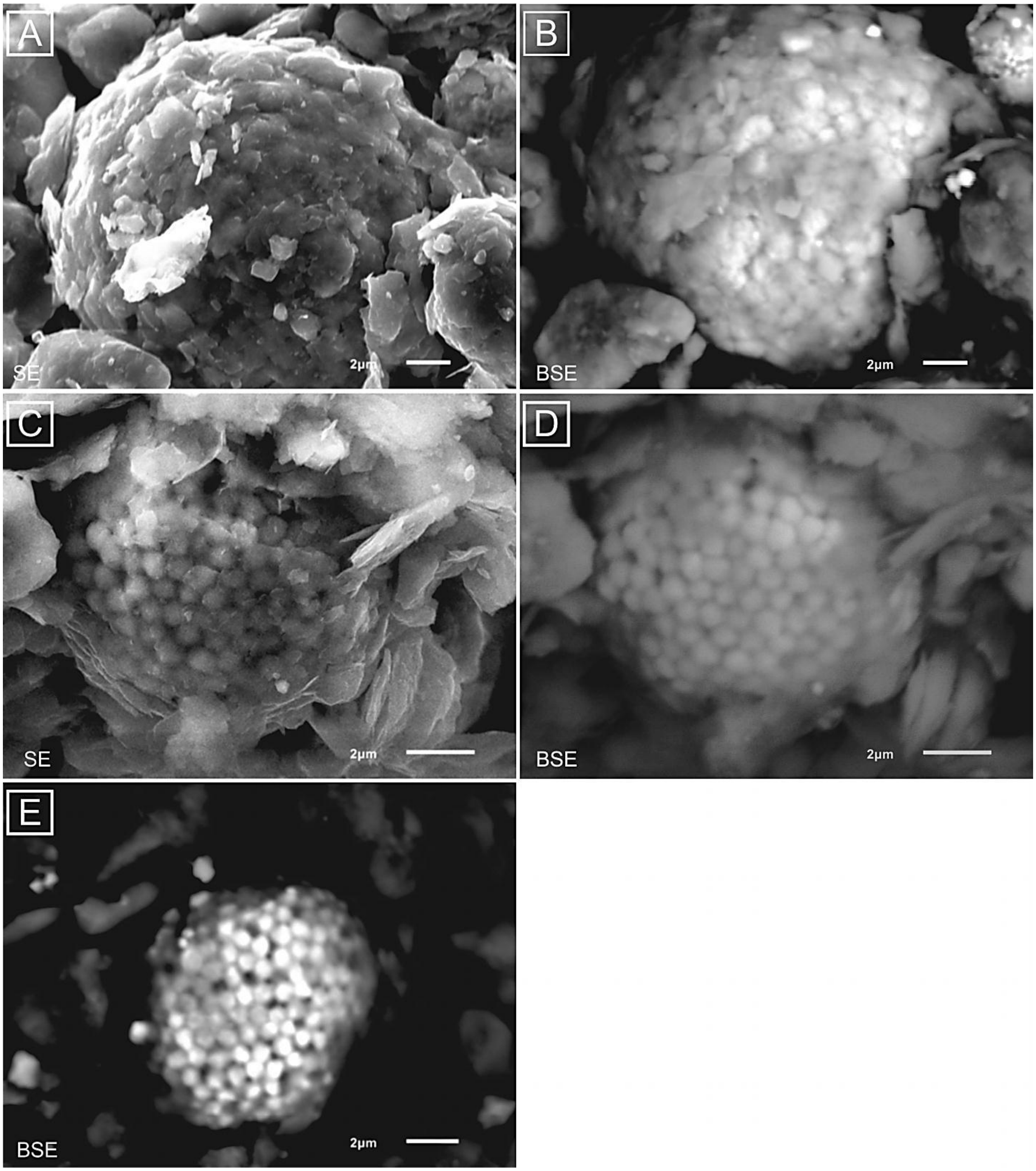

Figure 27. SEM images of three framboidal pyrite grains found in an ice sample from the Charas headwall. (A) and (C) SE images, (B), (D), (E) BSE images.

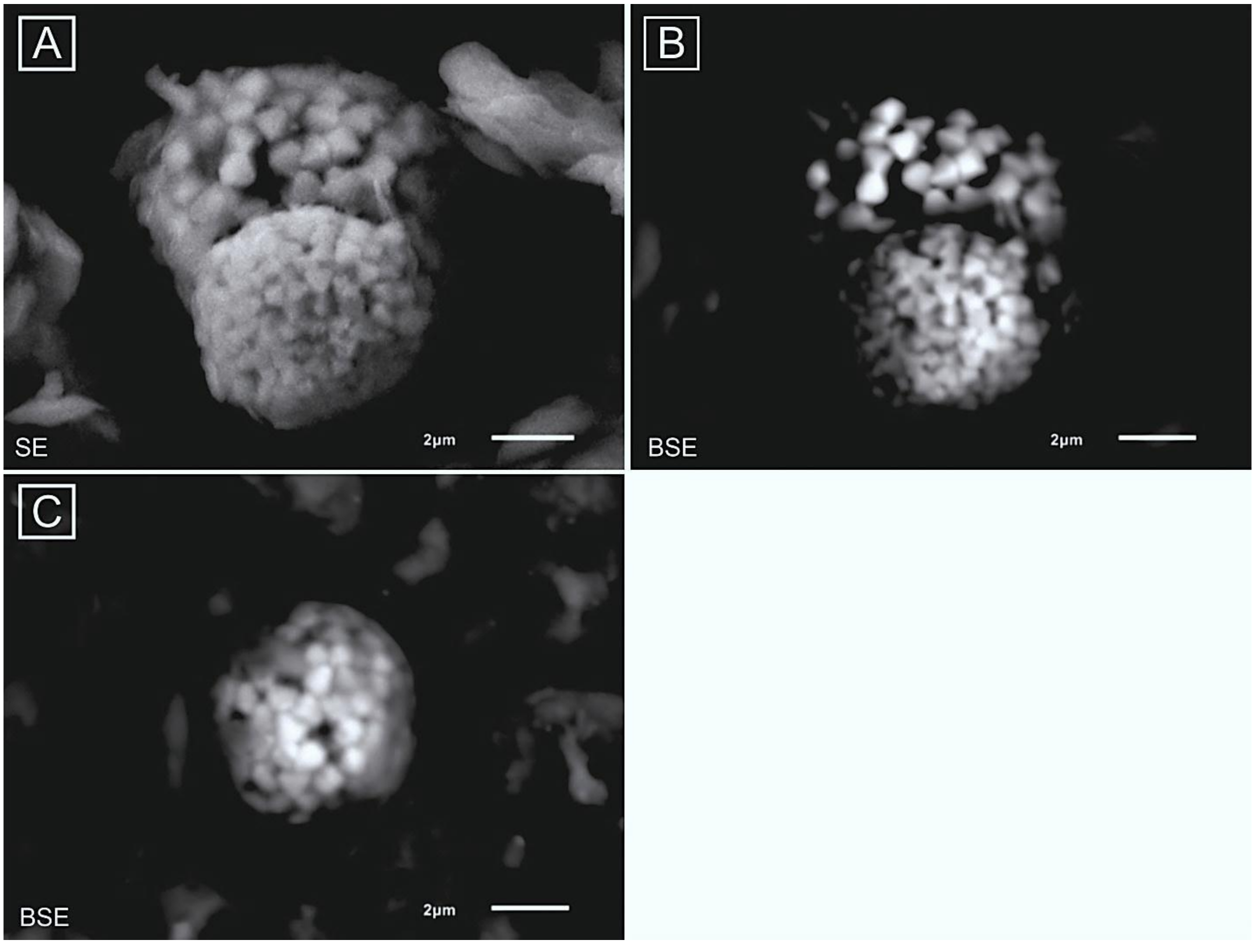

Figure 28. SEM images of framboidal pyrite in suspended sediment sample (11-LM-60).

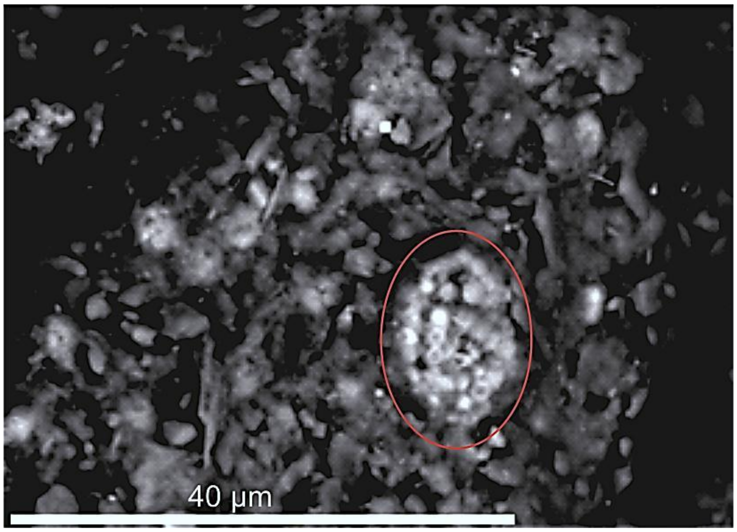

Figure 29. BSE image of Fe-hydroxide grain (circled) found in the unleached sample of 11-LM-60.

4.5 Leaching experiments and source of SO_4^{2-}

The first leaching experiment ran for 5 weeks and showed that concentrations of Ca^{2+} and SO_4^{2-} decrease at day 3 and then progressively increase until the end of the experiment to reach concentration of (Experiment 1: 11-LM-23 =560.37, 11-LM-46 =527.81, 11-LM-61 = 519.73mg/L Ca^{2+}) and (1718.61, 1380.98, 1523.18 mg/L SO_4^{2-}, respectively); the concentrations of Fe_{tot} reached a maximum value of 0.54 mg/L and was below detection limit in most leachate samples (Figure 30). This suggests that although pyrite has been identified by SEM-EDS analysis, pyrite oxidation is not occuring as Fe_{tot} and H^+ concentrations would be much higher (i.e., Lacelle et al., 2007; 2009). We suggest that the dissolution of deliquescent sulfate salts contained in the ice-rich tills are most likely the source of high SO_4^{2-} in slump runoff. The linear relation between SO_4^{2-} and Ca^{2+} further supports this hypothesis and shows that sulfate minerals remain undersaturated in the waters, as a decrease in the slope of the line is not observed (Figure 34).

The second experiment was done to improve the timing intervals, and shows similar results as the first experiment (Figure 31, Figure 33). The Ca^{2+} and SO_4^{2-} profiles are once again the same, and we see similar trends between K^+ and Na^+ in samples 11-LM-23 and 11-LM-60 (Figure 33 A, D).

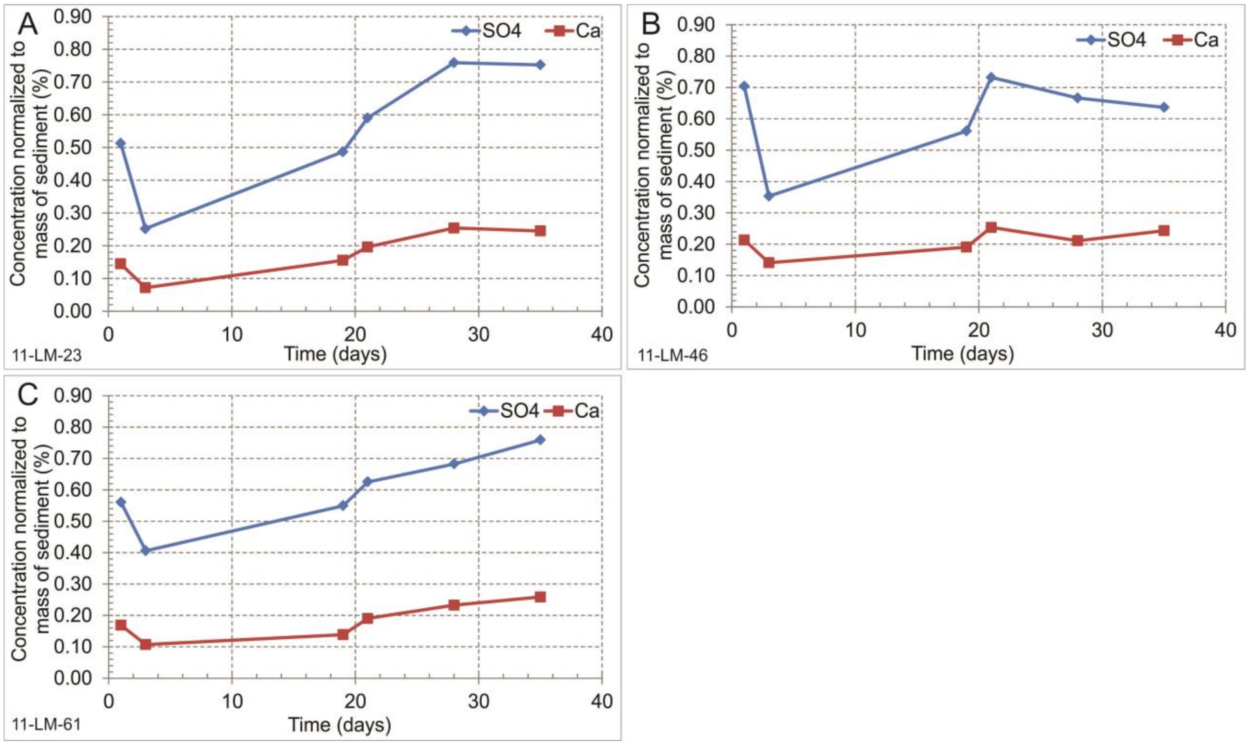

Figure 30. SO_4^{2-} and Ca^{2+} results from leaching experiment #1 for samples (A) 11-LM-23, (B) 11-LM-46, and (C) 11-LM-61.

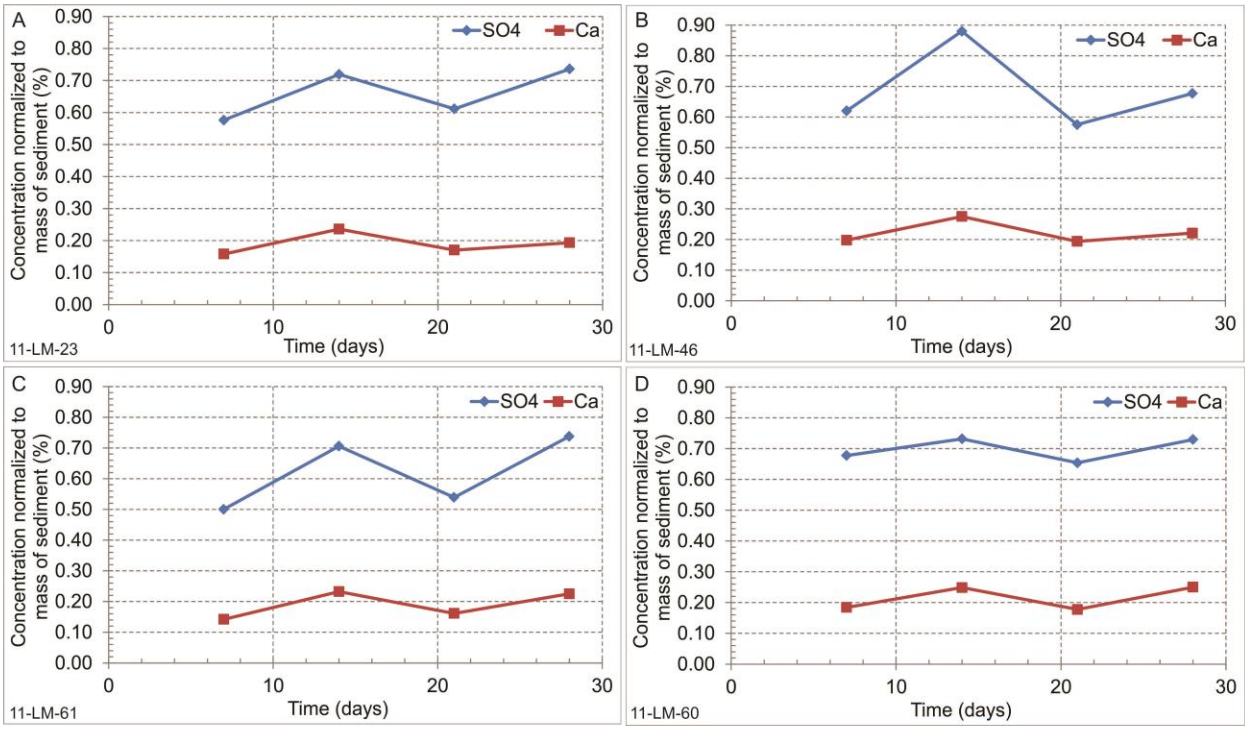

Figure 31 SO_4^{2-} and Ca^{2+} results of the second leaching experiment of samples (A) 11-LM-23, (B) 11-LM-46, (C) 11-LM-61 and (D) 11-LM-60

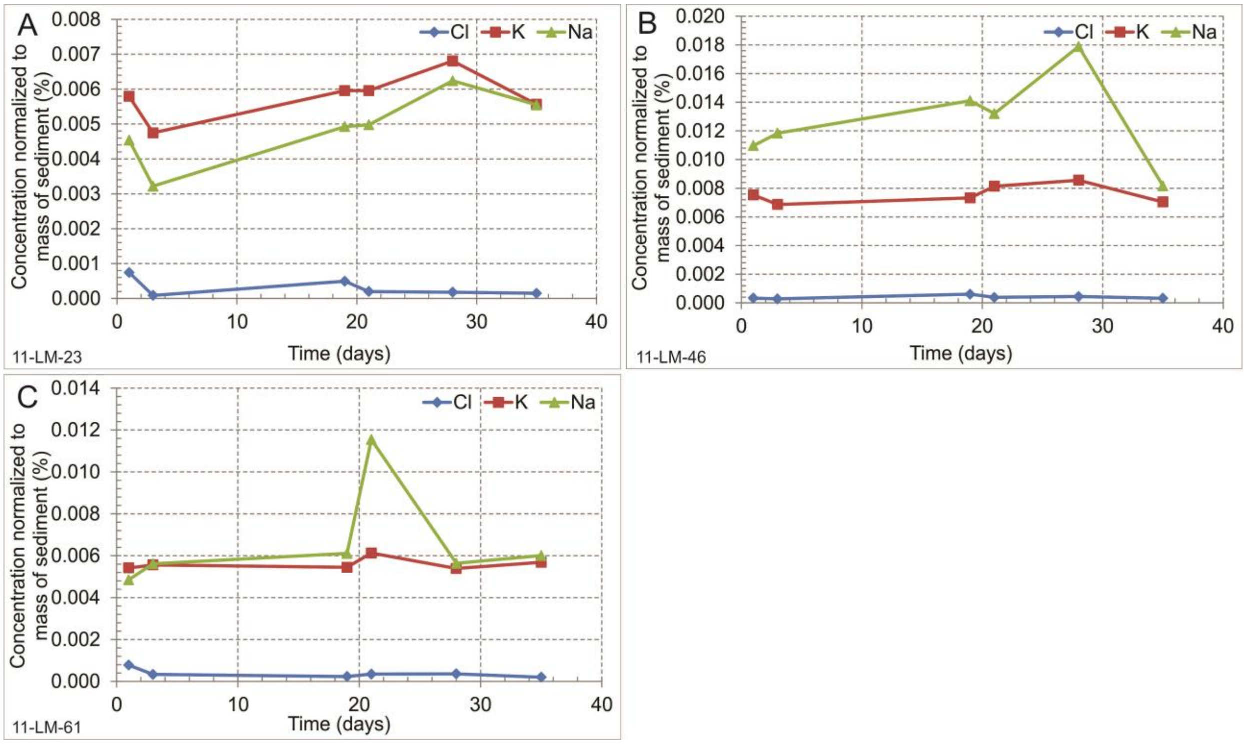

Figure 32. K^+, Na^+ and Cl^- results of leaching experiment #1 for samples (A) 11-LM-23 (B) 11-LM-46 and (C) 11-LM-61.

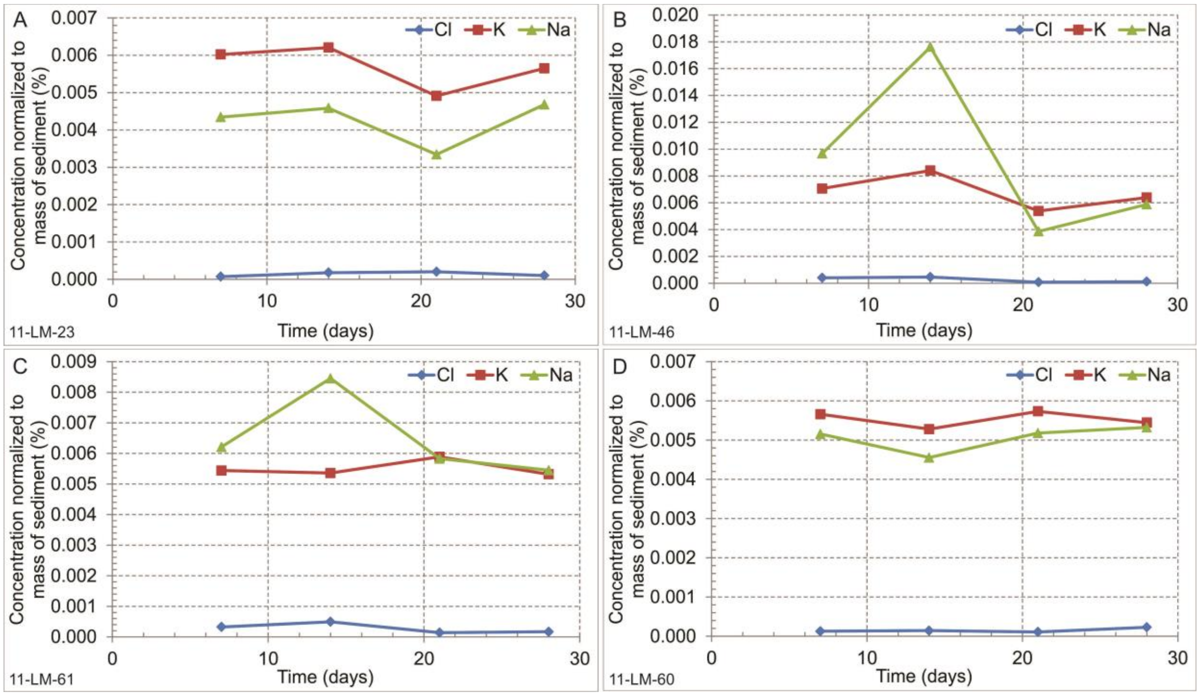

Figure 33. K^+, Na^+ and Cl^- results from the second leaching experiment of samples (A) 11-LM-23, (B) 11-LM-46, (C) 11-LM-61 and (D) 11-LM-60.

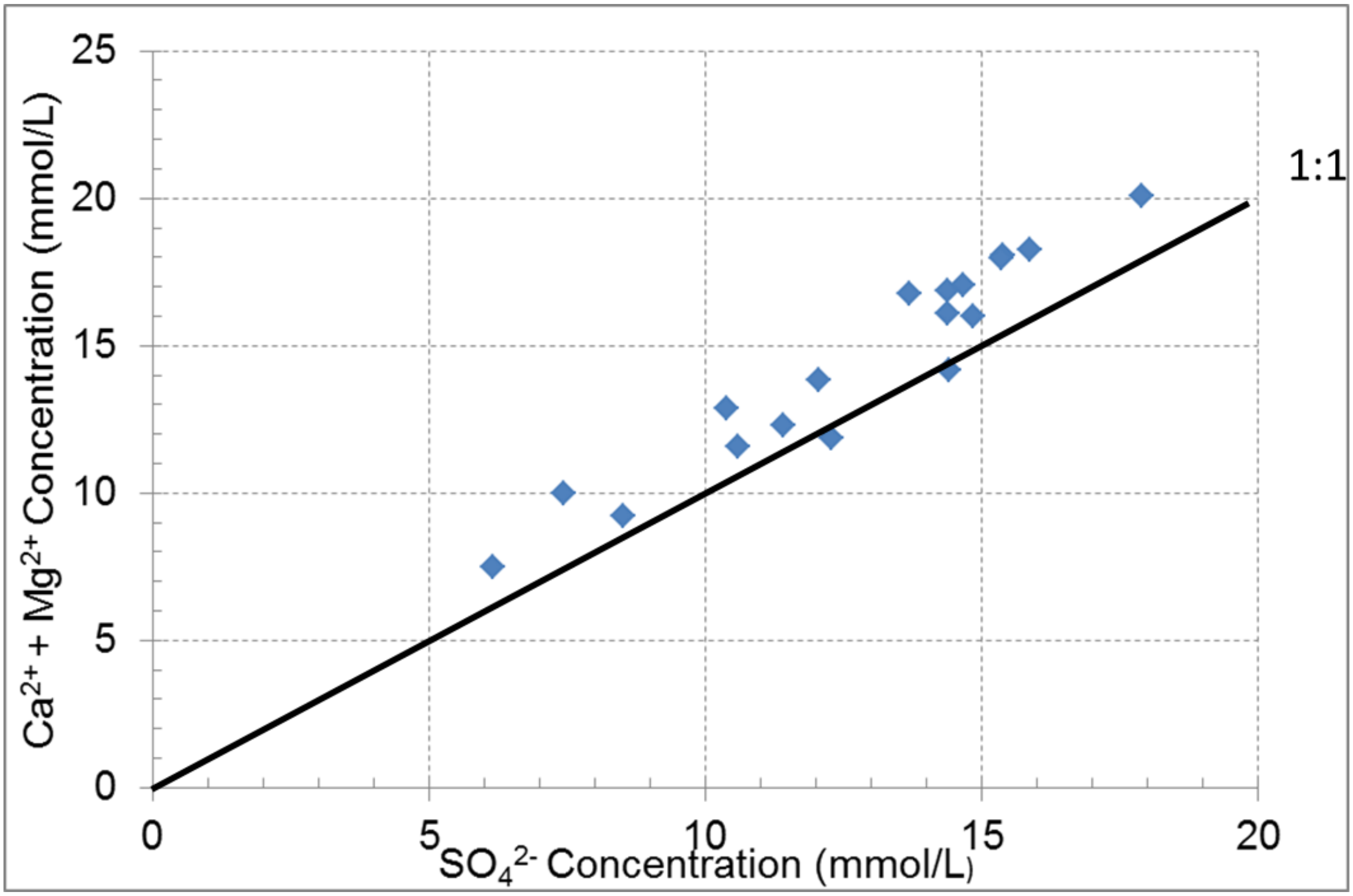

Figure 34. Concentration of Ca^{2+} vs. SO_4^{2-} in leachate samples of the second leaching experiment.

To estimate the percentage of SO_4^{2-} salts, as gypsum, that is present in the suspended sediment samples, the concentration of SO_4^{2-} to unit mass of soils that was released during leaching was calcualted using the following equation:

$$\text{corrected [ion] (mg/g)} = \frac{\text{[ion]} \times \text{ mass water}}{\text{mass sediments}} \quad [1]$$

For sample 11-LM-23, where 1718 mg/L of SO_4^{2-} was leached after 5 weeks from 10 g of soil, this provides a corrected SO_4^{2-} concentration of 85.9 mg/g. The mass of gypsum present in a 10 g sample is then 0.150 g $CaSO_4$ (0.0859 g /96 g/mol x 168 g/mol =0.150 g $CaSO_4$).

Suspended sediment samples that were used in leaching experiments were also analyzed by SEM to determine the sources of the solutes found in the leachate waters. The SEM imaging and

EDS analysis revealed the presence of framboidal pyrite in both the unleached and leached samples and the leached sample 11-LM-60 also contained a nearly perfect euhedral pyrite crystal (Figure 35). This confirms the geochemical analysis of leachate waters that although pyrite is found in our sample, its oxidation is not contributing to geochemical evolution of slump runoff waters (low Fe_{tot} concentration).

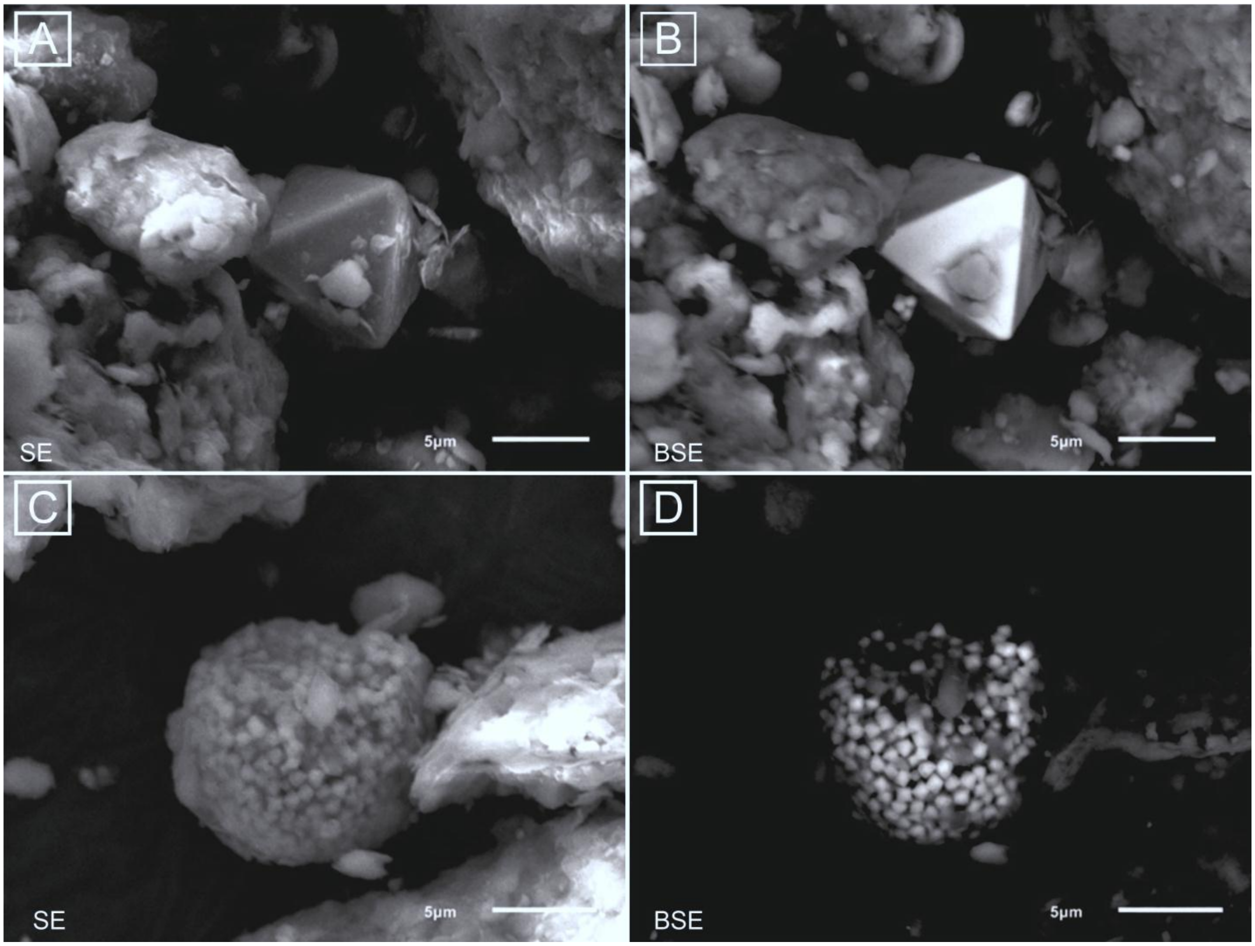

Figure 35. SEM images of euhedral (A and B) and framboidal pyrite (C and D) in the 2 week leached sample of 11-LM-60.

Since we suggest that the dissolution of deliquescent sulfate salts, gypsum, plays a key role in changing the geochemical composition of slump runoff, and that their presence was not identified in our mineralogical analysis and SEM-EDS composition, we tested the detection limit of XRD to identify gypsum. Five gypsum standards were also prepared to assess the presence of a gypsum at different concentrations. The standards included a 100% gypsum sample, as well as

0.5%, 1%, 2% and 5% gypsum concentrations mixed with quartz. Figure 36 shows that the 5% gypsum spike sample does not match the known gypsum spectra. This suggests that if any of the analyzed samples contained less than 5% gypsum salts, they would not be detected by XRD. Considering that our leaching experiment allowed us to calculate that our sample contains 1.5% gypsum, which is well below the 5% detection limit of XRD, and explains why gypsum was not detected in our XRD analysis of these sediments.

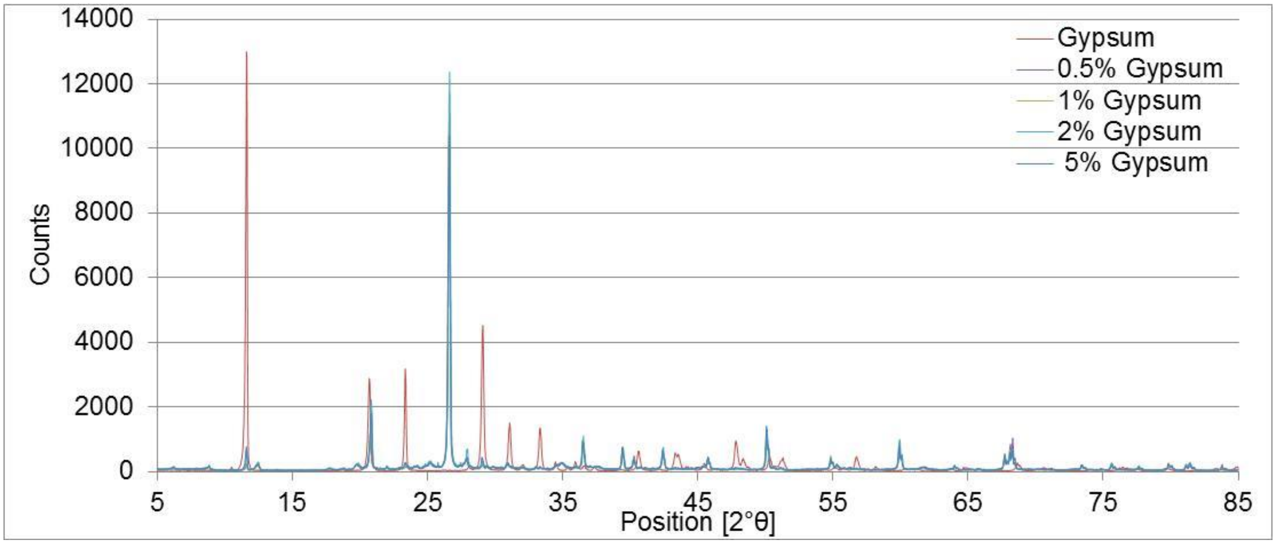

Figure 36. XRD spectra of a known gypsum sample, and known percentages of gypsum mixed with quartz

5. **DISCUSSION**

The goals of this project are to (1) characterize the geochemistry of the slump runoff, and the factors that influence its composition, (2) determine how the slump runoff is affecting pristine streams in the watershed and finally (3) to determine the extent, if any, of these impacts. This chapter will discuss the results presented in the previous chapter in an attempt to fulfill the three goals identified above.

5.1 Geochemical characterization and source of SO_4^{2-} in slump runoff

Runoff derived from thaw slumps is characterized by high conductivity and high solute concentrations and high sediment load. As the slump runoff travels down the mudflow, the conductivity and solute concentrations continue to increase (as surface waters equilibrate with high soil solute concentrations in the mudflow deposits) until some distance downstream where waters from pristine tundra streams dilute concentrations. The increase in solute concentrations of the slump runoff over the mudlobe is attributed to the leaching of deliquescent salts (i.e., gypsum). These sulfate salts potentially originated from the anhydrite unit (Bear Rock Fm) to the southeast, in the Fort Good Hope area and were incorporated into the till that was transported by the LIS and deposited in the study area.

5.1.1 SO_4/Cl: a potential geochemical tracer of slump runoff in the Peel River watershed

To evaluate the relative contribution of slump runoff in the watershed, Cl^- was chosen as a conservative tracer, and its relation with SO_4^{2-}, the dominant ion released in slump runoff, was investigated. There is a positive relationship between SO_4^{2-} and Cl^- that demonstrates mixing between the slump runoff and unaffected waters (Figure 37). SO_4/Cl ratios for Charas slump are up to 6 times higher than the ratios for unaffected waters, and Melanie slump (Figure 38). Variation in the contribution of slump runoff to streams contributes to the expected overlap between unaffected and affected waters. Since there is a statistical difference between the Charas slump runoff and unaffected streams, the use of this tracer is ideal in this environment (Table 1).

Considering that the concentration of solutes in affected streams represents mixing between two end-members, slump runoff and unaffected streams (Figure 39), we use SO_4/Cl to determine relative mixing proportions. Our calculations are based on the assumption that SO_4^{2-} originates mainly from ablating ice-rich permafrost exposed in the headwalls of thaw slumps. Even though an increase in active layer thickness has been found to contribute to increase solute concentration in surface runoff in northern Alaskan streams, no evidence of such a response of active layers is found along the Peel Plateau and surrounding areas in large part because the annual thaw-degree days have been decreasing since the mid-1980's. Further, Kokelj and Burn (2005) found that cation concentrations in the top of permafrost were up to 2.5 times greater than in the overlying active layer. The solution concentrations released from thawing ice-rich permafrost and in the slump runoff are 100 times higher than in unaffected streams, and accordingly, the potential solute release from increasing active layer would be unnoticeable in an environment where thaw slumps are impacting the aquatic ecosystem.

The two end members chosen for the calculation of mixing ratios were a slump runoff sample from the Charas slump with the highest value for SO_4/Cl (11-LM-44: 1532) and the minimum value for all unaffected samples (11-LM-12=2.88). A profile assuming that slump runoff is only being contributed by the Charas slump, shows that the fraction of slump runoff in the affected water decreases to 6% at 11 km away, and fluctuates slightly between 0 and 10% up to 22 km distance (Figure 40). These fluctuations are the result of possible contributions to Stony Creek coming from other thaw slump activity. The contribution from Melanie's slump (slump end member: 10-LM-62=387, unaffected= 2.88) into the Charas slump runoff decreases to 1.8% at 1.45 km away from the headwall. At 2 km from the Melanie headwall, the runoff is running alongside the Charas mudflow, explaining the increase in the slump runoff contribution at this point, as it could be leaching the Charas mudflow as it travels.

Using the SO_4/Cl ratio in two end member mixing calculations, and assuming that all the slump runoff is coming from the Charas slump, the fraction of slump runoff in the Peel River was determined for 1960-2009 (Figure 42). This figure shows the high and low end extremes of the mixing calculation, to show the possible variation within the results. Using the lowest ratio of SO_4/Cl at the headwall as an end member and minimum SO_4/Cl of unaffected streams, would suggest that the percentage of slump runoff making up the Peel River rose from ~ 0.7% to 48% from 1960-2009. This scenario is unlikely, however it does emphasize the importance of using well-defined end members. Using the highest SO_4/Cl ratio measured at the Charas headwall (ice-rich sediments), and the minimum value as unaffected end member, we see that the percentage of slump runoff in the Peel increases from 0.2% in the 1960s to 1.5% in 2009. Given the significant role that slumps can play in liberating solutes previously trapped in deep permafrost, the extremely high solute concentrations from these disturbances can have a discernable impact on the water chemistry of the Peel River. This analysis suggests that there has been an increase in the contribution of slump runoff to the Peel River over the last 50 years and even a contribution as small as 1.5% of slump runoff can be detected at the 67,000 km^2 watershed-scale.

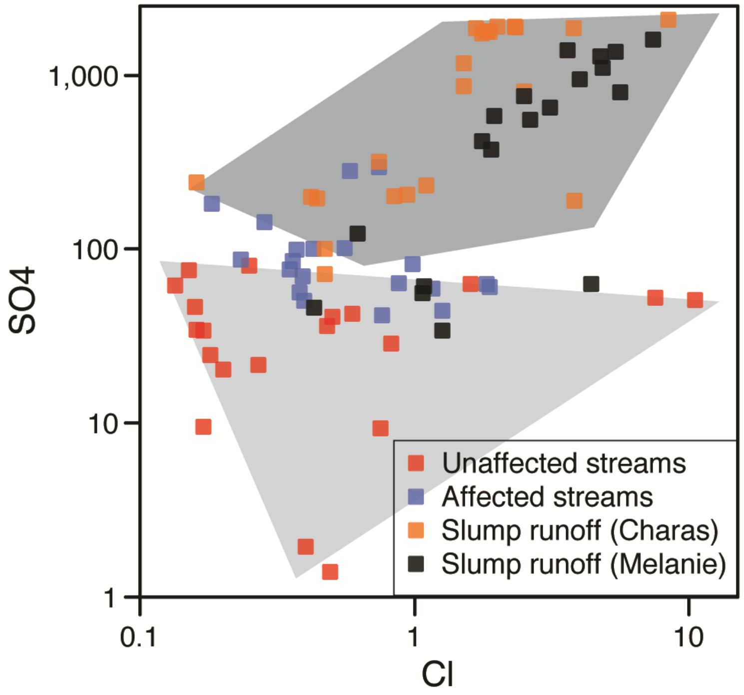

Figure 37. Relationship between SO_4^{2-} and Cl^- concentrations showing mixing between slump runoff and unaffected streams.

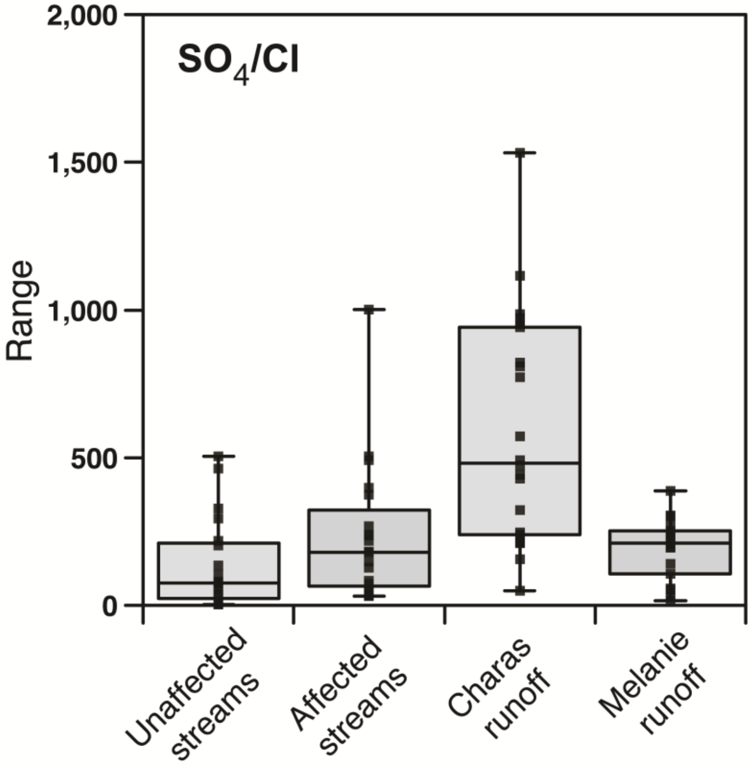

Figure 38. Box and Whisker plot showing the SO_4^{2-}/Cl ratios for unaffected and affected waters, Charas slump and Melanie slump runoff.

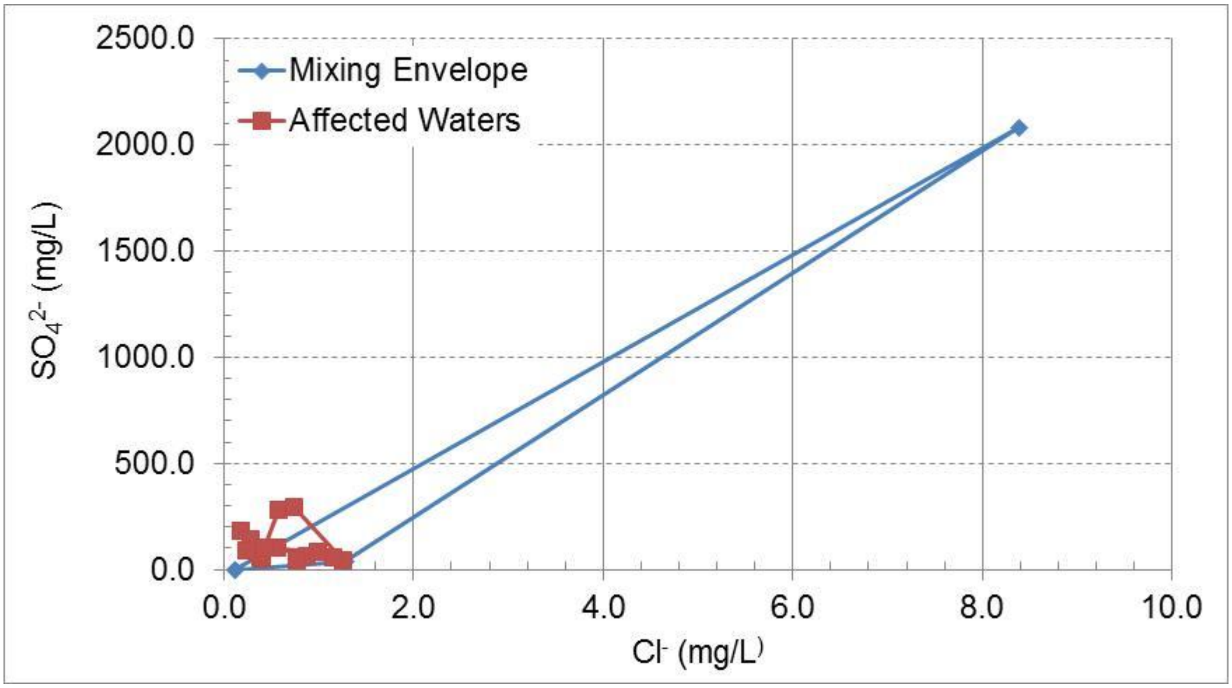

Figure 39. Example of three end member mixing envelope showing that the model involves only two end members (slump runoff and unaffected streams).

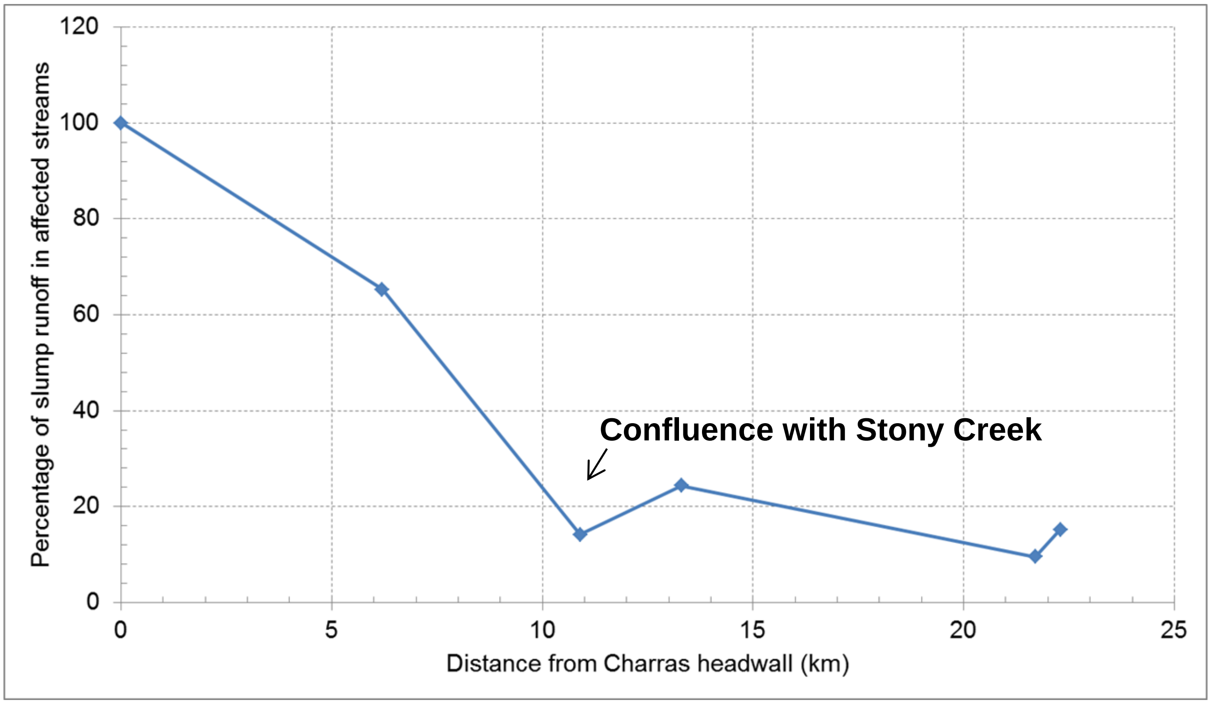

Figure 40. Percentage of slump runoff in affected waters with distance from headwall of Charas slump to a point 26 km downstream, in the Peel River. The fraction plotted at 0 distance represents the end member taken at the headwall.

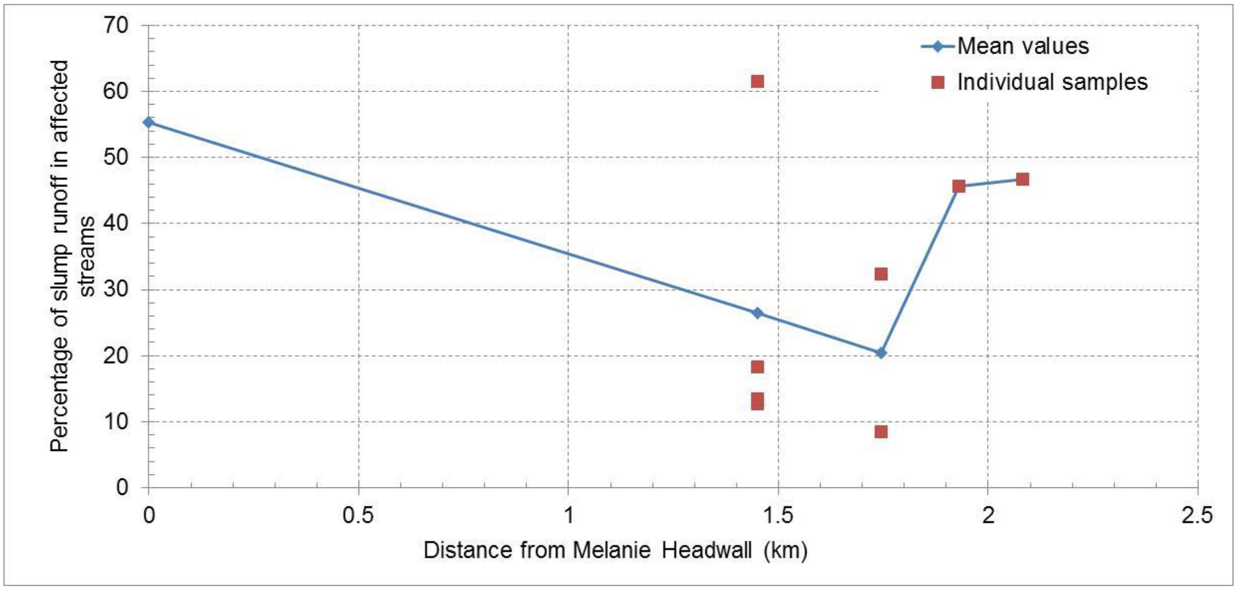

Figure 41. Percentage of slump runoff in streams with distance from Melanie slump headwall to discharge from lake at Charas mudflow. Average values at each distance are shown, with individual sample values. The fraction plotted at 0 distance represents the end member taken at the headwall.

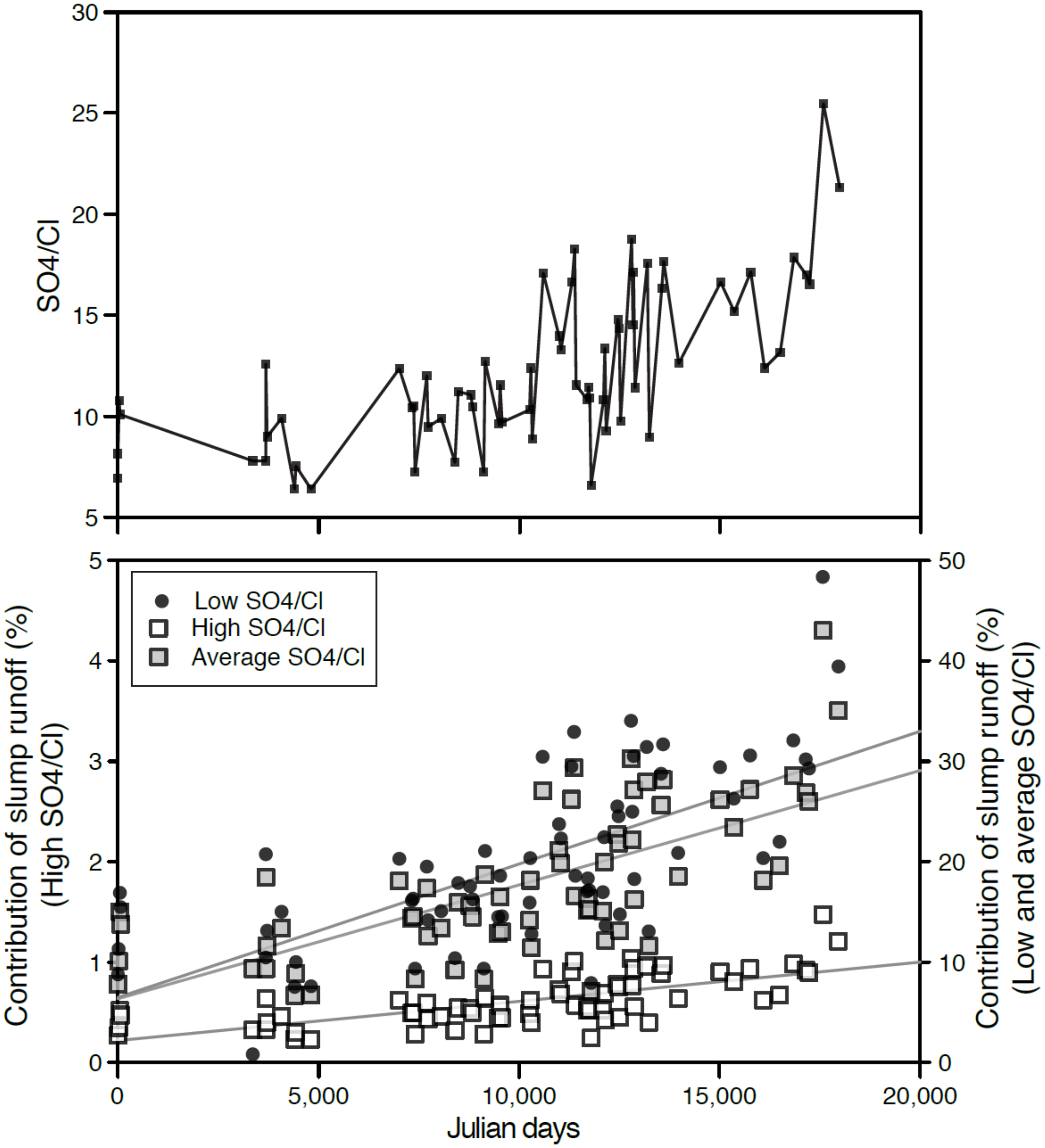

Figure 42. SO_4/Cl ratio in the Peel River during the summer months (July-October) from 1960-2009 (top). Percentage of slump runoff in the Peel River as determined by a two end member mixing model. Maximum and minimum SO_4/Cl concentrations at the headwall were used to show the possible variability in the calculations on either side of the average SO_4/Cl concentration in the slump runoff. The minimum SO_4/Cl was used as the unaffected end member. (Data from Environmental water quality monitoring data, 2010).

5.1.3 Comparing the impacts of slumps on the geochemistry of streams and lakes

The results of this study can be compared to those of Kokelj et al. (2005) who investigated the impacts of slumps on lake water geochemistry in the Mackenzie Delta region. This region has a similar surface material and is also underlain by carbonate and shale bedrock of the Mackenzie Basin. The pH of the lakes for both pristine and slump disturbed lakes was found to be neutral to slightly alkaline, with no statistical differences, however, the conductivity of disturbed lakes (274 to 1680 µS/cm) was significantly higher than that of undisturbed lakes (35 to 174 µS/cm). The relative proportion of dissolved cations for undisturbed and disturbed lakes was $Ca^{2+} > Mg^{2+} > Na^{+} > K^{+}$, but the absolute amounts are significantly higher in the disturbed lakes. The mean Ca^{2+} and Mg^{2+} concentrations in lakes with thermokarst influence were 72.6 and 26.8 mg/L respectively. Sulphate was found to be the dominant anion in the lake studies. In undisturbed lakes, concentrations ranged from 1 to 47 mg/L, but in disturbed lakes, the range was 35 to 836 mg/L.

These results from disturbed lake basins appear to be comparable to our results of slump runoff. For example, the conductivity of slump runoff is one order of magnitude higher than in unaffected streams (similar to the difference between pristine and disturbed lakes). However, the conductivity values in slump runoff reach values up to 3000 µS/cm, which is nearly twice the value in disturbed lakes. A similar observation can be made regarding the maximum concentration of SO_4^{2-}, Ca^{2+}, and Mg^{2+} in slump runoff compared to disturbed lakes. This difference in maximum dissolved ion concentration is attributed to the fact that slump runoff of hillslope slumps has to travel longer distances over the mudflow, which can reach up to 1.8km (this is a dynamic value). Conversely, direct runoff from lake-side slumps only has to travel over the slump floor which terminates at the lake. Here, the distance traveled by slump runoff is generally less than 500m and the soluble ions in the mudflow have less time to leach as the runoff flows over it. The slumps that form around lakes are also an order of magnitude smaller than those studied on the Peel Plateau.

Streams affected by slumps, however, have a different geochemical response to disturbed lakes. The dissolved ions in affected streams are much lower than in disturbed lakes and the local environment can affect the magnitude of impacts of slumps on water quality. Lakes, especially closed-basin lakes, receive meteoric inputs of freshwater mainly from precipitation. As such, lakes with thaw slumps along their shoreline can be viewed as sinks of direct slump runoff and the water quality will degrade progressively over the period when the slump is active. However, affected streams receive variying contributions from slump runoff, 2nd or higher level pristine streams that join the affected streams, and meteoric precipitation. It has been shown that the slump runoff contribution to affected streams varies diurnally by up to an order of magnitude and follow the patterns of net radiation and ground ice ablation in mega slumps (Kokelj et al., 2013).

5.2 Potential environmental impacts of hillslope thaw slumps

5.2.1 Slump runoff suspended sediments

The Canadian Environmental Quality Guidelines (CEQG) state that with respect to suspended sediments and the protection of aquatic life, a clear flowing freshwater body can only experience a maximum increase of 25mg/L from background level for short-term exposure (e.g., 24 hours). The maximum average increase is 5 mg/L from background levels for longer term exposures (24 hours-30 days) (CEQG, 1999).

For high flowing freshwater bodies, the maximum increase from background levels (25-50 mg/L) at any time is 25 mg/L. Suspended sediments should not increase more than 10% of background levels when background is ≥ 250 mg/L (CEQG, 1999).

The increase in suspended sediment from unaffected waters in the Stony Creek Watershed, to affected waters downstream of thaw slumps, is from ≤ 50 mg/L to an average 34 000 mg/L. This far exceeds guidelines for both clear flowing, and high flowing freshwater. With increasing distance from the slumps, suspended sediment drops out of the water column, so that by the time the water has travelled ~10 km , the suspended sediment concentration has dropped from 880 000 mg/L at the headwall to ~9000 mg/L (Figure 22). At 22 km away from the Charas headwall, the sediment load is 8800 mg/L, which is still more than the CEQG limit of 25 mg/L above background levels.

5.2.2 High SO_4^{2-} concentrations

The Canadian Environmental Quality Guidelines (CEQG) Summary Table states that the maximum concentration of SO_4^{2-} in water for the protection of agriculture is 1 000 000 ug/L or 1000 mg/L (CCME, 1987). The slump runoff values in this study were recorded to be up to more than double these guidelines.

The Government of British Columbia's Ambient Water Quality Guidelines for sulphate state that the maximum level for drinking water is 500 mg/L and that for freshwater aquatic life, the maximum concentration, not to be exceeded at any time is 100 mg/L. The level in the Peel River at 22km away from the Charas headwall is 100 mg/L, and the 2010 sample from 26 km away was 63 mg/L. Although the CCME does not have any sulphate guidelines for the protection of aquatic life, comparing the concentrations in the Peel River to the British Columbia guidelines indicates that sulphate levels could be cause for concern in the future.

6. SUMMARY AND CONCLUSIONS

A detailed study on the impacts of active thaw slump runoff on periglacial streams has assisted in understanding the geochemistry of the runoff and the processes that influence it. This study characterizes slump runoff as having elevated suspended sediments (911 g/L), high conductivity (2700 µS/cm), and high SO_4^{2-} (max. 2078 ppm). Slump runoff originates as a solute-rich meltwater near the slump headwall, and leaches and re-dissolves soluble salts (e.g. gypsum) as it flows along the mudflow, a process which results in the exceptionally high SO_4^{2-} concentrations. Conductivity increases until the runoff mixes with pristine waters which dilute the slump runoff signal.

Beyond the end of the mudflow, the concentrations of SO_4^{2-} and sediment load drop off fairly quickly with distance travelled. However, even at distances as far as 22 km downstream in the Peel River, the impacts of slump activity can still be observed. At this point in the Peel River, concentrations of SO_4^{2-} and suspended sediments are approaching environmental guidelines, posing a potential risk to fish habitats as well as other fragile parts of the stream ecosystem.

In areas hosting marine shales, SO_4/Cl can be used as a tracer in a two end member mixing calculation between slump runoff and pristine tundra streams to isolate the slump runoff signal in impacted waters, and determine its contribution in affected streams. The use of this ratio as a tracer in the Peel River shows that the contribution of slump runoff to the Peel River has been increasing since the 1960s. This study suggests that SO_4/Cl can be used as a tracer for thaw slump runoff in periglacial streams on the Peel Plateau.

Although the active thaw slumps in this study released significant amounts of solutes, particularly SO_4^{2-}, and suspended sediments, other potentially toxic solutes and metals such as arsenic, and zinc were all below detection, indicating that active thaw slumps in the Stony Creek watershed do not pose any threat of leaching these metals into the environment downstream.

7. CHALLENGES/FUTURE STUDIES

The dynamic nature of thaw slump activity posed many challenges in this study. The sheer size of the headwall alone creates a huge amount of inherent variability. Add to this the size and length of the mudflow, the various flowpaths carved into it by the runoff and subsequently abandoned, the constantly growing length of the mudflow leading to the incorporation of more and more unaffected water, the convergence and divergence of this water with the runoff several times over the length of the mudflow, as well as many other factors make the characterization of thaw slumps, and their processes an extremely difficult task. In order to obtain a truly quantitative understanding of the geochemistry of these two thaw slumps, and determine things like the solute flux emerging from them, an incredibly intense sampling protocol must be established. Sampling would have to be done on an hourly schedule from a significant number of sampling points along the width and length of the entire slump floor and mudflow. This would also help to obtain data on any diurnal fluctuations occurring within the slump mudflow. These diurnal variations have been shown to occur downstream of slumps (Kokelj et al., 2013) but due to the difficulties mentioned above, it is virtually impossible to install a data logger in the mudflow, and these measurements have not been possible to date.

Another aspect of the study to be improved upon in future, is to obtain accurate discharge measurements. The nature of the slump mudflow poses challenges for flow meters, as they become clogged with sediment, weirs, as the mud is too unstable for them to remain in place, and coloured dyes which would not be seen. Finally, chemical tracers such as chloride are not effective as part of the project is to determine the composition of the water within and downstream from the slump.

Finally, samples should be analyzed for sulfur isotopes to confirm the source of the SO_4^{2-}.

References

Aré, F.E., 1988. Thermal abrasion of sea coast, *Polar Geography and Geology*, 12: 1–157.

Bartleman, A-P., Miyanishi, K., Burn, C.R., Cote, M.M., 2001. Development of Vegetation Communities in a Retrogressive Thaw Slump near Mayo, Yukon Territory: A 10-Year Assessment, *Arctic*, 54 (2): 149-156.

Bowden, W.B., Gooseff, M.N., Balser, A., Green, A., Peterson, B.J. and Bradford, J., 2008. Sediment and nutrient delivery from thermokarst features in the foothills of the North Slope, Alaska: Potential impacts on headwater stream ecosystems. *Journal of Geophysical Research*, 113, doi:10.1029/2007JG000470

Burn, C.R., Kokelj, S.V., 2009. The Environment and Permafrost of the Mackenzie Delta Area, *Permafrost and Periglacial Processes*, 20: 83-105.

Burn, C.R., Friele, P.A., 1989. Geomorphology, vegetation succession, soil characteristics and permafrost in retrogressive thaw slumps near Mayo, Yukon Territory, *Arctic*, 42: 31-40.

Burn, C.R., Lewkowicz, A.G., 1990. Canadian Landform Examples-17 Retrogressive Thaw Slumps, The Canadian Geographer, 34(3): 273-276.

Burn, C.R., 2000. The thermal regime of a retrogressive thaw slump near Mayo, Yukon Territory, Canadian Journal of Earth Sciences, 37: 967-981.

Carey S.K., Woo, M.-K., 2001. Slope runoff processes and flow generation in a subarctic, subalpine environment, Journal of Hydrology, 253:110–129.

Carson, M.A., Malcolm Conly, F., Jasper, J.N., 1999. Riverine sediment balance of the Mackenzie Delta, Northwest Territories, Canada, *Hydrological Processes*, 13: 2499-2518.

Canadian Environmental Quality Guidelines, 1999. CCME. http://st-ts.ccme.ca/ April,2012

Coté, M.M., Burn, C.R., 2002. The oriented lakes of Tuktoyaktuk Peninsula, Western Arctic Coast, Canada: a GIS based analysis, *Permafrost and Periglacial Processes,* 13(1): 61-70.

Dugan, H.A., Lamoureux, S.F., Lewis, T., Lafreniere, M.J., 2012 The Impact of Permafrost Disturbances and Sediment Loading on the Limnological Characteristics of Two High Arctic Lakes, *Permafrost and Periglacial Processes*, 23(2): 119-126.

Duk-Rodkin, A., Lemmen, D.S. 2000. Glacial history of the Mackenzie region; in The Physical Environment of the Mackenzie Valley, Northwest Territories: a Base Line for the Assessment of Environmental Change, (eds.) L.D. Dyke and G.R. Brooks; Geological Survey of Canada, Bulletin 547, p. 11-20.

Duk-Rodkin, A., Hughes, O.L., 1995. Quaternary geology of the northeastern part of the central Mackenzie valley corridor, District of Mackenzie, Northwest Territories. Geological Survey of Canada Bulletin 458. Natural Resources Canada, Ottawa.

Dyke, A.S., Andrews, J.T., Clark, P.U., England, J.H., Miller, G.H., Shaw, J., Veillette, J.J., 2002. The Laurentian and Innuitian ice sheets during the last glacial maximum, *Quaternary Science Reviews*, 21: 9–31.

Environment Canada 2010, Hydroclimatological Data Retrieval Program (HYDAT) [http://ec.gc.ca/rhc-wsc/default.asp?lang=En&n=9018B5EC-1]. September 2011.

Environment Canada, Vegetation Types of the Mackenzie Corridor, prepared for Forest Management Institute, Canadian Forestry Service, 1974.

Frey, K. E. & McClelland, J. W., 2009. Impacts of permafrost degradation on arctic river biogeochemistry, *Hydrological Processes*, 23 (1), 169-182.

French, H.M., Egginton, P.A., 1973. Thermokarst development, Banks Island, western Canadian Arctic. The North American Contribution to the 2nd International Permafrost Conference, National Academy of Sciences, Washington, DC, Publication 2115, p. 203-212.

Héquette, A., Barnes, P.W., 1990. Coastal retreat and shoreface profile variations in the Canadian Beaufort Sea, *Marine Geology*, 91**:** 113–132.

Jorgenson, M.T., Shur, Y.L., Pullman, E.R., 2006. Abrupt increase in permafrost degradation in Arctic Alaska, *Geophysical Research Letters*, 33: doi:10.1029/2005GL024960.

Keller, K., Blum, J.D., Kling, G.W., 2010. Stream geochemistry as an indicator of increasing permafrost thaw depth in an arctic watershed, *Chemical Geology*, 273: 76-81.

Keller, K., Blum, J.D., Kling, G.W., 2007. Geochemistry of soils and streams on surfaces of varying ages in Arctic Alaska, *Arctic, Antarctic and Alpine Research*, 39: 84-98.

Kobayashi, N., 1985. Formation of thermoerosional niches into frozen bluffs due to storm surges on the Beaufort Sea coast, *Journal of Geophysical Research*, 90: 11983–11988, doi:10.1029/JC090iC06p11983

Kokelj, S.V., Burn, C.R., 2005. Geochemistry of the active layer and near-surface permafrost, Mackenzie delta region, Northwest Territories, Canada, *Canadian Journal of Earth Sciences*, 42: 37-48.

Kokelj, S.V., Lantz, T.C., Kanigan, J., Smith, S.L., Coutts, R., 2009a. Origin and Polycyclic behavior of thaw slumps, Mackenzie Delta region, *Permafrost and Periglacial Processes,* 20(2): 173-184.

Kokelj, S.V., Lewkowicz, A.G., 1999. Salinization of permafrost terrain due to natural geomorphic disturbance, Fosheim Peninsula, Ellesmere Island, *Arctic*, 52: 372-385.

Kokelj, S.V., Lacelle, D., Lantz, T.C., Malone, L., Tunnicliffe, J., Clark, I.D., Chin, K., 2013. Thawing of massive ground ice in mega thaw slumps drives the emergence of a new northern fluvial regime, *Journal of Geophysical Research*, submitted.

Kokelj, S.V., Zajdlik, B., Thompson, M.S., 2009b. The impacts of thawing permafrost on the chemistry of lakes across the subarctic boreal tundra transition, Mackenzie Delta region, Canada, *Permafrost and Periglacial Processes*, 20(2): 185-200.

Lacelle D., Bjornson, J. and Lauriol, B., 2010. Climatic and geomorphic factors affecting contemporary (1950-2004) activity of retrogressive thaw slumps on the Aklavik Plateau, Richardson Mountains, NWT, Canada, *Permafrost and Periglacial Processes*, 21: 1-15.

Lacelle, D.L., Bjornson, J., Lauriol, B., Clark, I.D., Troutet, Y., 2004. Segregated-intrusive ice of subglacial meltwater origin in retrogressive thaw flow headwalls, Richardson Mountains, NWT, Canada, *Quaternary Science Reviews*, 23: 681-696.

Lacelle, D., Doucet, A., Clark, I.D., Lauriol, B., 2007. Acid drainage generation and seasonal recycling in disturbed permafrost near Eagle Plains, northern Yukon Territory, Canada, *Chemical Geology*, 243: 157-177.

Lacelle, D., St-Jean, M., Lauriol, B., Clark, I.D., Lewkowicz, A., Froese, D., Kuehn, SC., Zazula, G., 2009. Burial and preservation a 30,000 year old perennial snowbank in Red Creek valley, Ogilvie Mountains, central Yukon, Canada, *Quaternary Science Reviews* 28: 3401-3413.

Lamoureux, S. F. & Lafrenière, M. J., 2009. Fluvial impact of extensive active layer detachments, Cape Bounty, Melville Island, Canada, *Arctic and Antarctic Alpine Research*, 4, 59-68.

Lantuit, H., Pollard, W.H., 2005. Temporal stereophotogrammetric analysis of retrogressive thaw slumps on Herschel Island, Yukon Territory, *Natural Hazards and Earth System Sciences,* 5: 413-423.

Lantuit, H. and Pollard, W.H., 2008. Fifty years of coastal erosion and retrogressive thaw slump activity on Herschel Island, southern Beaufort Sea, Yukon Territory, Canada, *Geomorphology,* 95: 84-102.

Lantz, T.C., and Kokelj, S.V., 2008. Increasing rates of retrogressive thaw slump activity in the Mackenzie delta region, N.W.T. Canada, *Geophysical Research Letters*, 35, doi:10.1029/2007GL032433.

Lewkowicz, A.G., and Kokelj, S.V., 2002. Slope sediment yield in arid lowland continuous permafrost environments, Canadian arctic Archipelago, *Catena*, 46: 261-283.

Lewkowicz, A.G., 1987a. Headwall retreat of ground-ice slumps, Banks Island, Northwest Territories, *Canadian Journal of Earth Sciences*, 24: 1077-1085.

Lewkowicz, A.G., 1987b. Nature and importance of thermokarst processes, Sand Hills moraine, Banks Island, Canada, *Geografiska Annaler*, 69A: 321-327.

Lewkowicz, A.G., 1990. Morphology, Frequency and Magnitude of Active Layer Detachment Slides, Fosheim Peninsula, Ellesmere Island, N.W.T. Final Proceedings, Fifth Canadian Permafrost Conference. Université Laval, Quebec City, 111-118.

Lewkowicz, A.G., 1991. Climatic change and the permafrost landscape, *in* Woo, M.K., Gregor, D.J. (eds.), Arctic Environment: Past, Present and Future, Proceedings of a Symposium, Nov 14–15, 1991. Dept. of Geography, McMaster University, Hamilton, p. 91–104.

Lim, D.S.S, Douglas, M.S.V., 2003. Limnological characteristics of the Haughton Crater, Devon Island, Nunavut, *Arctic, Antarctic and Alpine Research*, 35: 509-519.

Lis, G., Wassenaar, L.I., Hendry, M.J., 2008. High-Precision Laser Spectroscopy D/H and 18O/16O Measurements of Microliter Natural Water Samples, *Analytical Chemistry*, 80 (1): 287-293.

Mackay, J.R., 1995. Active layer changes (1968 to 1993) following the forest-tundra fire near Inuvik, N.W.T., Canada, *Arctic and Alpine Research*, 27: 323-336.

Mackay, J.R., 1966. Segregated epigenetic ice and slumps in permafrost, Mackenzie Delta, N.W.T., *Geographical Bulletin*, 8: 59-80.

McGillivray, D.G., Agnew, T.A., McKay, G.A., Pilkington, G.R., Hill, M.C., 1993. Impacts of climatic change on the Beaufort sea-ice regime: Implications for the arctic petroleum industry, Climate Change Digest CCD 93-01, Environment Canada, Downsview, Ontario 36.

Norris, D.K., 1984. Geology of the northern Yukon and northwestern District of Mackenzie. Geological Survey of Canada, Map 1581A, scale 1 : 500 000.

Osterkamp, T.E. and Romanovsky, V.E., 1999. Evidence for warming and thawing of discontinuous permafrost in Alaska, *Permafrost and Periglacial Processes*, 10: 17-37.

Parkhurst, D.L., Appelo, C.A.J., 1999. User’s guide to PHREEQC (version 2) - -a computer program for speciation, batch-reaction, one-dimensional transport, and inverse geochemical calculations: U.S. Geological Survey Water-Resources Investigations Report 99-4259.

Quinton, W.L., and Marsh, P., 1999. A conceptual framework for runoff generation in a permafrost environment, *Hydrological Processes*, 13: 2563-2581.

Raymond, P. A., McClelland, J. W., Holmes, R. M., Zhulidov, A. V., Mull, K., Peterson, B. J., Striegl, R. G., Aiken, G. R. & Gurtovaya, T. Y., 2007. Flux and age of dissolved organic carbon exported to the Arctic Ocean: A carbon isotopic study of the five largest arctic rivers, *Global Biogeochemical Cycles,* 21, GB4011.

Serreze, M.C., Walsh, J.E., Chapin, F.S., Osterkamp, T., Dyurgerov, M., Romanovsky, V., Oechel, W.C., Morison, J., Zhang, T., Barry, R.G., 2000. Observational Evidence of Recent Change in the Northern High-Latitude Environment, *Climatic Change*, 46: 159-207.

Smith, C.A.S., Meikle, J.C. and Roots, C.F. (eds), 2004. Ecoregions of the Yukon Territory - Biophysical Properties of Yukon Landscapes. Agriculture and Agri-Food Canada, PARC Technical Bulletin 04-01, Summerland, British Columbia.

Smith, S.L., Burgess, M.M., 2000. Ground temperature database for northern Canada; Geological Survey of Canada Open File Report #3954.

Stewart, K.A., Lamoureux, S.F., 2011. Connections between river runoff and limnological conditions in adjacent High Arctic lakes: Cape Bounty, Melville Island, Nunavut, Arctic, 64(2): 137-268.

Solomon, S.M., 2005. Spatial and temporal variability of shoreline change in the Beaufort–Mackenzie region, Northwest Territories, Canada, *Geo-Marine Letters*, 25 (2–3): 127–137.

Wolfe, S.A., Kotler, E., Nixon, M.F., 2000. Recent warming impacts in the Mackenzie Delta, Northwest Territories, and northern Yukon Territory coastal areas. Current Research, Geological Survey of Canada Paper, 2000-B1: 1-9.

Zazula, G.D., Mackay, G., Andrews, T.D., Shapiro, B., Letts, B., and Brock, F., 2009. A late Pleistocene steppe bison (Bison priscus) partial carcass from Tsiigehtchic, Northwest Territories, Canada, *Quaternary Science Reviews*, 28(25–26): 2734–2742.

Appendix A: Ice-Rich Permafrost Geochemistry Results

Sample name	Type of Ice	Alkalinity (ppm HCO_3^-)	Cl (mg/L)	SO_4 (mg/L)	NO_3 (mg/L)	Al (mg/L)	As (mg/L)	Ba (mg/L)	Ca (mg/L)	Fe (mg/L)	K (mg/L)	Mg (mg/L)	Mn (mg/L)	Na (mg/L)	S (mg/L)	Si (mg/L)	Zn (mg/L)	Sr (mg/L)	Saturation Indices						
MELANIE																			$KAl_3(SO_4)_2(OH)_6$	$CaSO_4$	$BaSO_4$	$CaSO_4{\cdot}H2O$	NaCl	FeOH(a)	$Fe(OH)_3$
FMM-2	Diamicton and Frozen Diacton	0.49	5.53	2167.29	0.10	0.07	0.02	0.01	538.26	<0.012	23.36	160.58	3.59	226.92	836.17	2.23	0.01	0.28	7.34	-0.17	0.43	0.08	-7.53		
FMM-8		0.14	7.20	1489.37	<0.065	0.02	0.04	0.02	323.44	<0.012	19.84	108.63	1.25	183.00	533.80	2.37	<0.005	0.25	5.51	-0.43	0.71	-0.18	-7.48		
FMM-9		0.56	7.84	2177.02	0.33	0.08	0.01	0.02	638.60	<0.012	32.11	177.71	2.61	273.09	952.09	1.69	0.02	0.36	7.59	-0.12	0.72	0.13	-7.3		
FMM-11		0.56	8.05	2180.11	<0.065	0.08	0.00	0.01	567.41	<0.012	27.16	164.64	2.73	238.35	876.96	2.21	0.02	0.30	7.57	-0.15	0.43	0.1	-7.35		
FMM-12		0.56	7.21	1967.76	0.59	0.08	0.05	0.02	525.55	<0.012	22.24	137.44	2.12	202.42	768.54	2.11	0.02	0.36	7.44	-0.2	0.72	0.05	-7.46		
FMM-13		0.00	3.62	704.56	<0.065	0.02	0.04	0.02	180.88	<0.012	12.91	53.74	0.05	107.30	279.29	2.32	<0.005	0.20		-0.87	0.1	-0.65	-8.04		
FMM-14		-	1.36	2229.73	<0.065	0.07	0.12	0.01	587.30	<0.012	30.16	164.17	3.64	223.71	900.83	1.27	0.04	0.29							
FMM-14B		-	5.03	2143.31	16.08	0.07	0.16	0.02	536.14	<0.012	23.79	159.53	3.47	208.24	835.25	2.22	0.02	0.26							
FMM-17		-	9.68	2306.42	<0.065	0.08	<0.023	0.01	553.24	<0.012	30.43	194.93	3.54	269.53	928.80	3.22	0.03	0.20							
FMM-A		-	5.12	2254.65	0.30	0.15	0.08	0.01	543.42	<0.012	29.62	193.03	3.64	207.85	881.18	2.38	<0.005	0.26							
FMM-18		-	4.98	1829.67	<0.065	0.09	0.00	0.02	521.36	<0.012	21.69	128.29	1.52	147.20	718.41	1.88	<0.005	0.29							
M1		0.57	6.59	2144.47	6.38	0.08	0.07	0.02	558.29	<0.012	24.41	154.69	1.71	254.19	862.49	1.80	<0.005	0.36	7.34	-0.17	0.7	0.08	-7.41		
M2		0.65	5.07	2143.16	<0.065	0.09	0.00	0.01	554.37	0.034	26.40	161.52	2.22	240.96	871.94	2.65	<0.005	0.29	7.53	-0.17	0.4	0.08	-7.54	-0.27	4.69
M3		-	6.50	2219.23	<0.065	0.20	0.08	0.03	559.60	2.141	26.97	168.67	3.55	270.94	902.68	2.81	0.05	0.24							
M4		-	3.84	985.44	<0.065	0.03	<0.023	0.01	290.45	0.139	17.00	83.08	0.25	160.08	448.68	2.83	<0.005	0.26							
M5		-	7.05	1520.62	<0.065	0.05	<0.023	0.01	357.38	<0.012	20.49	110.02	0.48	187.97	570.87	2.30	<0.005	0.25							
M6		-	8.33	2058.31	3.19	0.12	0.04	0.01	576.44	0.645	25.09	155.24	1.05	226.25	841.64	1.76	<0.005	0.36							
M7		-	8.08	2097.80	22.59	0.08	0.04	0.01	582.69	0.282	25.94	165.70	1.89	223.85	864.14	2.33	<0.005	0.34							
M15		-	6.42	2117.07	<0.065	0.08	0.01	0.01	543.38	<0.012	26.27	158.69	2.42	274.28	872.67	3.03	0.02	0.25							
M16		-	7.09	2052.72	<0.065	0.07	<0.023	0.01	553.96	<0.012	25.12	151.08	2.35	237.02	845.57	2.09	<0.005	0.35							
M17		-	7.72	2168.14	<0.065	0.11	0.08	0.01	552.62	<0.012	27.85	181.23	1.84	243.46	891.11	3.45	<0.005	0.23							
MB		-	5.07	2046.74	<0.065	0.08	<0.023	0.01	596.76	<0.012	36.67	205.90	4.00	235.98	964.51	2.35	0.01	0.28							
MC		-	6.41	2356.24	<0.065	0.05	<0.023	0.01	533.39	<0.012	35.99	203.09	4.08	245.98	928.13	2.59	<0.005	0.28							
Mean		0.44	6.25	1972.17	6.19	0.08	0.05	0.01	511.95	0.65	25.72	153.98	2.35	221.24	798.94	2.34	0.02	0.28							
StDev		0.24	1.85	416.17	8.56	0.04	0.04	0.00	111.72	0.87	5.54	37.14	1.22	42.21	175.18	0.51	0.01	0.05							
CHARAS																									
Coin de glace festival	Ice veins/silt + sediments	0.9882	3.04	12.42	7.27	0.13	0.05	0.11	9.47	0.70	0.95	1.51	0.06	2.84	5.29	0.42	0.03	0.03	3.34	-3.3	0.31	-3.05		1.5	6.46
C-A		0.070455	0.47	287.25	<0.065	0.01	<0.023	0.03	107.27	<0.012	4.15	23.65	0.00	16.73	114.12	2.18	<0.005	0.55	2.85	-1.24	0.64	-0.99	-9.63		
C-C		0	0.41	180.37	<0.065	0.00	0.11	0.04	74.85	0.14	4.03	18.62	0.02	15.57	71.77	2.02	<0.005	0.40		-1.52	0.67	-1.27	-9.71	0.68	5.64
C-D		-	0.72	562.40	<0.065	0.06	<0.023	0.02	226.60	<0.012	5.62	34.98	0.01	22.78	234.18	1.59	<0.005	0.84							
CE		-	0.59	16.40	<0.065	0.02	0.03	0.62	6.64	2.51	0.26	1.35	0.10	1.53	5.32	0.50	0.04	0.03							
C13		4.36E-01	0.98	380.88	<0.065	0.06	0.04	0.03	122.74	<0.012	5.52	28.27	0.00	46.53	153.90	2.00	<0.005	0.65	5.49E+00	-1.12E+00	0.69	-0.86	-8.88		
C14		1.41E-01	1.04	497.99	<0.065	0.02	0.01	0.02	169.56	<0.012	5.64	32.42	0.00	41.54	199.56	1.99	<0.005	0.78							
C15		-	0.35	126.62	<0.065	0.01	0.00	0.05	67.24	<0.012	2.02	11.30	0.00	7.32	49.45	1.24	<0.005	0.34							
C16		-	0.28	247.66	<0.065	<0.023	0.05	0.03	100.80	<0.012	3.96	20.78	0.00	15.91	99.12	1.55	<0.005	0.52		-1.31	0.61	-1.06	-9.88		
Mean		0.33	0.88	256.89	-	0.04	0.04	0.11	98.35	1.12	3.57	19.21	0.02	18.97	103.63	1.50	0.03	0.46							
Stdev		0.41	0.85	196.30	-	0.04	0.04	0.19	70.74	1.24	2.04	12.36	0.04	15.85	80.77	0.66	0.01	0.29							
C17	Silt	0.65331	1.24	538.57	<0.065	0.09	0.04	0.02	130.78	<0.012	8.26	62.94	0.00	46.45	212.88	2.42	<0.005	0.73							
C-9	Laminated Colluvium	-	2.38	761.71	0.37	0.00	0.03	0.01	227.79	<0.012	9.81	64.63	0.01	92.01	335.18	3.63	<0.005	1.04							
C18	Reticulate ice, interspersed with silt	-	1.33	290.60	<0.065	<0.023	0.06	0.02	57.72	<0.012	7.94	46.63	0.00	44.21	112.12	3.12	<0.005	0.52		-1.50E+00	0.47	-1.25	-8.76		
C19		0.42029	9.87	1907.97	0.55	0.06	0.04	0.01	507.15	<0.012	14.58	200.94	1.34	121.06	815.96	3.70	<0.005	1.64							
C21		-	1.31	161.76	0.79	0.02	0.03	0.02	153.29	<0.012	8.01	61.37	0.00	46.89	221.54	2.64	<0.005	0.71							
C22		-	4.61	2066.73	0.45	0.14	<0.023	0.01	615.28	<0.012	15.37	201.66	2.99	104.54	873.16	3.33	<0.005	2.05							
C24		0.492392	3.12	1779.66	0.31	0.07	<0.023	0.02	582.31	0.18	13.15	148.80	1.58	62.69	739.50	2.75	0.02	1.73	6.95E+00	-1.90E-01	0.7	0.06	-8.33	0.51	5.43
C25		-	4.03	1918.60	0.57	0.07	0.01	0.01	556.89	0.15	14.80	202.53	3.60	103.50	834.94	4.07	0.00	1.91							
C26		-	3.34	1910.36	<0.065	0.06	<0.023	0.01	581.88	<0.012	14.01	189.05	0.06	88.59	820.32	3.22	0.03	2.01							
C27		-	4.74	1871.62	0.43	0.08	0.00	0.01	598.56	<0.012	16.05	204.21	1.04	116.86	860.62	4.78	<0.005	1.95							
C28		-	1.86	1862.61	<0.065	0.09	0.03	0.01	653.60	<0.012	13.62	171.01	0.10	79.32	820.74	3.73	0.00	2.09							
C29		-	1.39	1698.36	<0.065	2.81	0.02	0.01	660.27	<0.012	11.79	137.70	0.13	52.79	762.99	3.61	0.19	1.72							
C30		0.63257	4.31	2024.19	<0.065	0.09	0.08	0.01	630.45	<0.012	16.59	204.27	1.47	112.63	887.80	3.57	0.01	2.08	7.41E+00	-1.40E-01	0.41	0.11	-7.94		
C31		-	3.75	2017.20	0.35	0.07	0.06	0.01	612.66	<0.012	16.87	199.01	3.43	106.16	862.87	4.13	0.01	1.95							
C32		-	2.11	1889.83	<0.065	0.08	0.01	0.01	650.97	<0.012	15.27	176.21	1.72	81.47	844.78	3.25	0.01	2.05							
C33		-	1.70	1809.52	1.22	0.06	0.03	0.02	642.52	<0.012	14.72	157.12	2.94	75.78	800.99	3.49	0.01	1.95							
C34		-	0.28	1558.86	<0.065	0.07	0.10	0.01	594.92	<0.012	13.17	121.36	0.66	61.09	683.37	3.68	<0.005	1.92							
C35		-	1.94	1623.43	0.47	0.11	0.01	0.02	579.47	<0.012	13.24	118.35	0.62	80.00	686.09	3.23	<0.005	2.09							
C36		-	1.51	1781.20	<0.065	0.08	0.03	0.01	647.73	<0.012	12.47	122.69	1.32	70.91	743.20	2.44	<0.005	2.22							
C37		0.214171	1.69	608.52	1.69	0.03	0.00	0.02	205.61	<0.012	9.47	52.08	0.02	70.71	259.62	2.99	<0.005	1.00	5.22E+00	-8.10E-01	0.6	-0.56	-8.48		
Mean		0.44	2.94	1598.95	0.68	0.24	0.03	0.01	529.51	0.17	13.39	150.83	1.28	82.18	701.70	3.43	0.03	1.75							
StDev		0.17	2.18	593.01	0.44	0.66	0.03	0.00	185.63	0.02	2.66	54.15	1.24	24.13	240.80	0.57	0.06	0.49							
C39	Ice veins	0.214354	0.60	553.36	1.72	0.03	0.04	0.02	219.65	<0.012	6.88	41.33	0.01	33.64	236.11	2.47	<0.005	0.88	5.02E+00	-8.00E-01	0.58	-0.55			
C40		-	0.72	557.21	0.68	0.04	0.03	0.02	210.99	<0.012	7.58	42.69	0.02	40.75	238.09	2.93	<0.005	0.91							
C41		-	4.22	867.88	0.70	0.03	0.04	0.01	271.51	<0.012	10.77	66.89	0.03	104.98	366.75	3.36	<0.005	1.30							
C42		-	7.34	597.31	<0.065	0.04	0.07	0.01	381.91	<0.012	11.69	90.33	0.05	116.13	496.91	3.26	<0.005	1.56							
C43		0.494344	11.27	1600.11	0.23	0.07	0.02	0.01	474.33	<0.012	15.38	124.13	0.86	199.55	683.55	4.11	<0.005	1.90	6.99E+00	-2.90E-01	0.4	-0.04	-7.26		
Mean		0.35	4.83	835.18	0.84	0.04	0.04	0.01	311.68	-	10.46	73.08	0.19	99.01	404.28	3.23	-	1.31							
StDev		0.20	4.55	447.06	0.63	0.02	0.02	0.00	113.59	-	3.43	34.90	0.37	67.28	189.66	0.60	-	0.43							

Appendix B: Water Chemistry Analysis Results

Table B1. Water Chemistry Analysis Results Unaffected Stream samples

Sample	Sampling Date	Description	Latitude	Longitude	pH	Conductivity (µS/cm)	Sed load (g/L)	Alkalinity (ppm HCO_3^-)	Cl (mg/L)	SO_4 (mg/L)	NO_3 (mg/L)	Al (mg/L)	As (mg/L)	Ba (mg/L)	Ca (mg/L)	Fe (mg/L)	K (mg/L)	Mg (mg/L)	Mn (mg/L)	Na (mg/L)	S (mg/L)	Si (mg/L)	Zn (mg/L)	SO_4/Cl	del D	del18O	Saturation Indices					
UNAFFECTED STREAMS																											**$BaSO_4$**	**$CaSO_4$.2H2O**	**$CaSO_4$**	**$Fe(OH)_3$**	**FeOOH**	**$CaCO_3$**
11-LM-64	2011	Near Charras between slump and stabilized slump (draining into lake)	67.25355	-135.23927	6.77	139.5	<0.01	39.64	0.158	46.63	0.65	0.11	<0.025	-	27.15	0.43	0.49	5.06	0.02	0.49	16.39	1.62	0.0033	294.95	-163.1	-20.3	0.25	-2.41	-2.15	0.77	6.09	-1.74
11-LM-68	2011	Small stream beside Charas mudflow	67.25876	135.23783	5.74	136.6	<0.01	27.90	0.134	61.84	0.34	0.63	<0.025	-	17.75	0.89	0.31	4.99	0.19	4.10	22.79	3.08	0.0698	463.24	-162.2	-21.5	0.36	-2.21	-2.47	-2.00	3.33	-3.11
11-LM-69	2011	Small trickle to North of end of Charras mudflow	67.26056	-135.2356	4.45	154.5	<0.01	8.49	0.150	75.60	4.86	0.51	<0.025	-	22.11	0.76	0.77	5.56	0.24	1.28	25.45	3.90	0.0532	503.68	-166.3	-21.7	0.53	-2.04	-2.29	-6.07	-0.94	-4.81
11-LM-10	2011	Stream at Melanie's slump, drains into 11-LM-12	67.2519	-135.27736	4.89	15.72	<0.01	4.43	0.403	1.96	<0.025	0.15	<0.025	-	1.43	0.43	0.77	0.49	0.1225	0.52	0.86	0.46	0.0136	4.88	-188.6	-24.6	-0.80	-4.61	-4.87	-4.90	0.23	-5.76
11-LM-12	2011	Flows parallel to Melanie slump mudflow	67.25211	-135.27376	5.48	16.77	<0.01	0.68	0.486	1.40	<0.025	0.14	<0.025	-	1.58	0.34	0.92	0.55	0.0724	0.51	0.52	0.42	0.0148	2.88	-187.0	-24.6	-1.05	-4.71	-4.97	-3.09	2.24	-5.93
11-LM-13	2011	Same stream as 11-LM-12 but further downstream, alongside mudflow	67.25181	-135.27275	6.76	39.4	<0.01	5.49	0.747	9.34	<0.025	0.11	<0.025	-	3.51	0.78	0.79	1.41	0.1056	1.12	3.71	0.75	0.0092	12.50	-183.4	-23.8	-0.27	-3.59	-3.84	1.08	6.41	-3.46
11-LM-49	2011	Stream beside Melanie's slump	67.25181	-135.27275	6.82	37.7	<0.01	1.00	0.165	9.51	<0.025	0.13	<0.025	-	3.40	0.48	0.46	1.54	0.0151	1.41	4.59	1.13	0.0056	57.57	-169.5	-22.5	-0.26	-3.59	-3.84	1.05	6.38	-4.84
11-LM-74B	2011	Unaffected lake/pooling to west of Melanie slump mudflow	67.25235	-135.27397	6.08	50.8	<0.01	16.75	0.594	42.61	<0.025	0.18	<0.025	-	6.35	1.14	0.30	2.87	0.0944	1.85	7.06	2.63	0.0108	71.76	-157.6	-20.3	0.27	-2.75	-3.01	-0.84	4.49	-3.41
11-LM-18	2011	Stream to West of Charas slump	67.25196	-135.27377	8.07	248.5	<0.01	15.42	0.246	80.27	<0.025	0.02	<0.025	-	19.85	0.02	0.72	9.86	0.0012	5.30	31.04	0.75	<0.003	326.56	-183.3	-24.2	0.50	-2.07	-2.32	2.26	7.47	-1.05
10-LM-04	2010	Stream Recharge into lake between Melanie and Charas slumps	67.25543	-135.24843	8.1	108.9	<0.01	23.13	0.195	20.38	<0.025	0.05	<0.025	0.05	14.18	0.43	0.55	3.13	0.0016	1.57	-	1.48	-	104.39	-167.0	-22.0	-0.07	-2.72	-2.98	3.42	8.75	-0.89
10-LM-10	2010	Flows downhill to slump runoff on North side of Charas mudflow	67.25862	-135.23763	6.4	77.3	<0.01	*7.98*	0.183	24.53	<0.025	0.02	<0.025	0.03	61.82	0.02	0.59	16.17	0.0023	5.98	-	1.08	-	134.07	-172.7	-22.3	2.60	0.4	0.14	-0.38	4.95	0.27
10-LM-16	2010	Stream flows parallel to Melanie slump mudflow	67.25211	-135.27376	7.07	73.4	<0.01	*3.39*	0.271	21.51	<0.025	0.11	<0.025	0.05	6.79	0.93	0.46	3.01	0.0010	1.29	-	1.83	-	79.40	-166.8	-21.9	2.96	-0.23	-0.48	3.46	8.98	-0.28
10-LM-21	2010	Stream flowing towards Melanie slump	67.25108	-135.27255	7.35	226	<0.01	*4.97*	7.511	52.36	0.04	0.07	<0.025	0.03	14.51	0.34	1.61	11.71	0.0012	13.45	-	1.72	-	6.97	-161.6	-20.8	-0.09	-2.39	-2.64	2.39	7.91	-2.30
10-LM-25	2010	Creek flowing into Stony Creek at its confluence with the Peel River	67.24355	-135.27684	7.36	143.6	<0.01	37.09	0.818	28.59	<0.025	0.12	<0.025	0.07	14.59	1.11	1.53	6.64	0.0174	4.64	-	1.25	-	34.95	-167.9	-20.6	0.08	-2.61	-2.86	2.92	8.44	-1.35
10-LM-26	2010	Peel River upstream of Stony Creek	67.2322	-134.55348	7.67	339	<0.01	119.01	1.602	63.04	0.16	0.02	<0.025	0.06	40.47	<0.006	0.55	15.75	<0.00055	3.36	-	1.28	-	39.36	-178.2	-22.3	0.21	-1.95	-2.2	-	-	-0.15
10-LM-32	2010	Stream North of Stony Creek	67.22854	-134.54942	7.38	166	<0.01	*0.32*	0.167	33.99	0.93	0.03	<0.025	0.06	18.39	0.36	0.76	5.83	0.0067	3.85	-	1.04	-	203.06	-170.7	-22.3	0.19	-2.42	-2.67	2.48	7.81	-4.11
10-LM-36	2010	Stream North of Stony Creek	67.27128	-135.37265	7.78	122.5	<0.01	*0.68*	0.156	34.34	0.13	0.03	<0.025	0.05	11.03	0.46	0.70	4.73	0.0239	3.43	-	1.07	-	219.56	-173.2	-22.1	0.03	-2.62	-2.87	3.07	8.59	-3.51
10-LM-40	2010	Stream flows parallel to Melanie slump mudflow	67.26247	-135.52684	6.86	114.2	<0.01	10.42	0.484	36.04	0.07	0.05	<0.025	0.07	11.74	0.55	0.75	5.31	0.0039	2.69	-	1.57	-	74.41	-166.7	-21.5	0.19	-2.58	-2.83	1.30	6.82	-2.51
10-LM-43	2010	Stream flows parallel to Melanie slump mudflow	67.52029	-135.30344	6.79	362	<0.01	*0.55*	10.538	50.91	0.11	0.06	<0.025	0.08	23.76	10.69	2.45	16.54	0.0361	17.88	-	2.26	-	4.83	-160.1	-20.3	0.28	-2.23	-2.48	2.35	7.88	-4.32
10-LM-64	2010	Stream to West of Melanie mudflow	67.52029	-135.30344	6.88	118.8	<0.01	11.57	0.534	40.72	<0.025	0.09	<0.025	<0.0001	10.67	0.27	0.40	4.40	0.1553	14.65	-	3.00	-	76.29	-160.4	-20.5	0.16	-2.58	-2.83	1.04	6.57	-2.47
Mean					**6.74**	**135**	**-**	**16.95**	**1.277**	**36.78**	**0.81**	**0.13**	**-**	**0.06**	**16.55**	**1.08**	**0.79**	**6.28**	**0.06**	**4.47**	**12.49**	**1.62**	**0.02**	**136**	**-170.3**	**-22.0**	**0.30**	**-2.50**	**-2.72**	**0.54**	**5.92**	**-2.79**
StDev					**0.99**	**97**	**-**	**26.82**	**2.717**	**22.94**	**1.55**	**0.16**	**-**	**0.02**	**14.38**	**2.35**	**0.52**	**5.08**	**0.07**	**5.01**	**11.62**	**0.93**	**0.02**	**152.31**	**9.3**	**1.4**	**0.93**	**1.18**	**1.18**	**2.78**	**2.88**	**1.85**

Notes:

Italicized values were determined using PHREEQC modelling

Average Ba concentrations for each water category were used in PHREEQC

Table B2. Water Chemistry Analysis Results for Affected stream samples

Sample	Sampling Date	Description	Latitude	Longitude	pH	Conductivity (μS/cm)	Sed load (g/L)	Alkalinity (ppm HCO_3^-)	pH	Conductivity (μS/cm)	Cl (mg/L)	SO4 (mg/L)	NO3 (mg/L)	Al (mg/L)	As (mg/L)	Ba (mg/L)	Ca (mg/L)	Fe (mg/L)	K (mg/L)	Mg (mg/L)	Mn (mg/L)	Na (mg/L)	S (mg/L)	Si (mg/L)	Zn (mg/L)	SO4/Cl	del D	del18O	Saturation Indices					
AFFECTED STREAMS																													**$BaSO_4$**	**$CaSO_4$.2H2O**	**$CaSO_4$**	**$Fe(OH)_3$**	**FeOOH**	**$CaCO_3$**
10-LM-01	2010	Charras lake	67.25505	-135.242	7.64	184.4	1.47	14.0	7.64	184.4	0.40	50.38	<0.025	0.13	<0.025	0.074	20.05	0.34	1.83	6.93	0.04	4.61	-	1.62	-	127.24	-169.8	-21.9	0.28	-2.25	-2.5	2.83	8.36	-1.4
10-LM-05	2010	Stream Recharge from Melanie slump	67.25419	-135.24698	7.79	219.6	6.84	27.0	7.79	219.6	0.36	84.99	0.14	0.08	<0.025	0.055	26.96	0.25	2.56	10.28	0.04	7.37	-	1.71	-	238.95	-169.5	-22.6	0.28	-1.95	-2.2	2.8	8.32	-0.85
10-LM-24	2010	Stony Creek datalogger location	67.23465	-135.2367	7.72	230.0	0.20	56.6	7.72	230.0	0.38	56.58	0.02	0.03	<0.025	0.053	25.85	0.06	1.03	7.77	0.00	6.81	-	1.20	-	148.81	-175.6	-22.9	0.15	-2.13	-2.37	2.13	7.66	-0.59
10-LM-27	2010	Peel River downstream of Stony Creek	67.25333	-134.54908	7.94	331.0	0.01	122.0	7.94	331.0	1.83	62.99	0.14	0.03	<0.025	0.056	40.97	<0.0006	0.89	15.92	0.00	3.34	-	1.30	-	34.39	-179.5	-22.6	0.31	-1.94	-2.19	-	-	0.05
10-LM-33	2010	Stream North of Melanie slump	67.27123	-135.2929	7.97	770.0	4.07	123.0	7.97	770.0	0.58	282.38	0.93	0.02	<0.025	0.038	101.67	<0.0006	2.26	30.78	0.03	22.17	-	1.29	-	491.09	-165.7	-21.3	0.42	-1.1	-1.35	-	-	0.43
10-LM-37	2010	Mouth of Poor Man's Creek	67.1368	-135.16803	7.5	682.0	12.25	86.9	7.5	682.0	0.74	295.94	<0.025	0.26	<0.025	0.042	89.82	0.66	2.97	23.91	0.01	27.71	-	1.55	-	399.05	-170.7	-21.8	0.56	-1.1	-1.35	2.88	8.21	-0.32
10-LM-38	2010	Mouth North Stony Creek	67.3242	-135.1416	7.83	267.0	0.00	*60.0*	7.83	267.0	1.87	60.43	<0.025	0.08	<0.025	0.068	31.96	0.22	1.09	8.64	0.00	7.04	-	1.11	-	32.33	-171.3	-21.6	0.3	-2.02	-2.27	2.76	8.28	-0.38
11-LM-55	2011	Charas Lake	67.25505	-135.242	6.8	168.5	1.52	15.7	6.8	168.5	1.26	44.43	0.45	0.12	<0.025	-	14.38	0.52	1.70	4.10	0.11	2.41	15.20	1.33	0.0070	35.35	-169.4	-22.4	0.22	-2.41	-2.66	1.02	6.42	-2.35
11-LM-56	2011	Melanie slump runoff (by Charas lake)	67.25419	-135.24698	6.76	157.1	9.61	24.6	6.76	157.1	1.16	59.53	0.65	0.19	<0.025	-	16.76	0.64	1.59	5.58	0.17	4.05	20.67	1.44	0.0035	51.39	-163.2	-21.4	0.3	-2.25	-2.5	0.97	6.37	-2.15
11-LM-63	2011	Logger location upstream of lake	67.25419	-135.24698	6.41	133.6	3.46	6.4	6.41	133.6	0.87	64.01	0.46	0.09	<0.025	-	18.27	0.40	1.17	7.02	0.24	6.03	24.48	2.57	0.0189	73.23	-153.9	-19.1	0.32	-2.19	-2.44	-0.27	5.13	-3.05
11-LM-65	2011	Discharge from lake, running beside mudflow	67.25662	-135.24024	5.84	180.3	3.90	6.4	5.84	180.3	0.56	101.38	0.39	0.15	<0.025	-	28.36	0.30	0.99	8.19	0.35	4.90	36.27	2.53	0.0362	182.18	-158.4	-20.8	0.46	-1.88	-2.14	-2.20	3.13	-3.51
11-LM-71	2011	Charas Lake Discharge	67.25596	-135.24029	6.71	200.3	3.51	17.3	6.71	200.3	0.37	99.04	0.38	0.10	<0.025	-	31.70	0.35	0.98	8.59	0.20	4.95	35.65	2.40	0.0080	267.17	-154.8	-20.0	0.44	-1.82	-2.07	0.53	5.94	-2.1
11-LM-73	2011	Discharge from lake, right at lake	67.25596	-135.24029	7.17	155.8	1.01	17.7	7.17	155.8	0.39	69.80	<0.025	0.07	<0.025	-	25.47	0.43	0.97	7.12	0.13	4.84	25.88	2.55	0.0075	178.30	-160.8	-21.0	0.34	-2.03	-2.28	1.98	7.39	-1.7
11-LM-75	2011	Point A in watershed transect downstream	67.2961	-135.1745	7.64	352.0	550.46	76.5	7.64	352.0	0.18	182.76	0.11	0.01	<0.025	-	81.80	0.02	3.29	15.77	0.09	13.64	71.38	1.53	0.0009	1001.43	-160.8	-20.5	0.54	-1.28	-1.54	1.65	7.05	-0.19
11-LM-77	2011	Point A stream 2-Poor Man's Creek	67.2961	-135.17451	7.66	300.0	31.07	55.7	7.66	300.0	0.28	143.17	0.34	0.02	<0.025	-	69.59	0.06	2.88	13.35	0.05	11.36	57.43	1.61	0.0001	504.46	-161.6	-20.9	0.49	-1.42	-1.67	2.17	7.57	-0.35
11-LM-78	2011	Point B Confluence with Stony Creek	67.3275	-135.122	7.57	169.5	9.39	59.1	7.57	169.5	0.35	76.56	0.34	0.05	<0.025	-	39.61	0.20	1.50	8.02	0.01	7.00	29.44	1.91	0.0014	219.30	-160.0	-20.7	0.33	-1.84	-2.1	2.57	7.97	-0.6
11-LM-80	2011	Point C in watershed downstream of slump	67.3373	-135.0825	7.62	180.3	7.79	31.0	7.62	180.3	0.23	87.36	0.33	0.04	<0.025	-	37.48	0.14	1.42	10.21	0.02	5.74	34.05	1.86	0.0025	375.74	-155.3	-19.8	0.38	-1.81	-2.07	2.5	7.91	-0.86
11-LM-81	2011	Point D-Mouth of Stony at Peel	67.3878	-134.924	7.49	208.6	8.86	35.4	7.49	208.6	0.43	100.35	0.45	0.02	<0.025	-	44.66	0.07	1.54	11.22	0.04	7.06	39.55	1.73	0.0028	235.39	-155.7	-20.3	0.41	-1.7	-1.95	1.96	7.37	-0.87
11-LM-82	2011	Peel River at Ferry	67.33799	-134.87365	7.82	261.7	0.71	113.6	7.82	261.7	0.98	81.84	0.19	0.03	<0.025	-	59.00	0.02	0.78	15.74	0.01	5.54	31.67	1.59	-0.0005	83.17	-160.9	-20.7	0.3	-1.71	-1.96	1.85	7.25	0.07
11-LM-53	2011	Logger location upstream of lake	67.25419	-135.24698	5.86	122.7	0.01	20.9	5.86	122.7	0.76	41.54	0.35	0.17	<0.025	-	13.48	0.50	1.49	4.57	0.16	3.76	16.49	1.54	0.0055	54.35	-167.0	-22.3	0.19	-2.47	-2.72	-1.82	3.59	-3.18
Mean					**7.29**	**263.7**	**32.81**	**48.5**	**7.29**	**263.7**	**0.70**	**102.27**	**0.37**	**0.08**	**-**	**0.055**	**40.89**	**0.29**	**1.65**	**11.19**	**0.09**	**8.02**	**33.70**	**1.72**	**0.0072**	**236.67**	**-160.1**	**-20.8**	**0.35**	**-1.87**	**-2.12**	**1.46**	**6.88**	**-1.20**
StDev					**0.66**	**170.6**	**122.05**	**38.3**	**0.66**	**170.6**	**0.50**	**72.24**	**0.22**	**0.07**	**-**	**0.013**	**26.06**	**0.21**	**0.76**	**6.64**	**0.10**	**6.40**	**15.82**	**0.46**	**0.0101**	**233.44**	**4.6**	**0.9**	**0.11**	**0.40**	**0.39**	**1.53**	**1.56**	**1.17**

Notes:

Italicized values were determined using PHREEQC modelling

Average Ba concentrations for each water category were used in PHREEQC

Table B3. Water Chemistry Analysis Results for Slump Runoff samples

Sample	Sampling Date	Description	Latitude	Longitude	pH	Conductivity (µS/cm)	Sed load (g/L)	Alkalinity (ppm HCO_3-)	Cl (mg/L)	SO_4 (mg/L)	NO_3 (mg/L)	Al (mg/L)	As (mg/L)	Ba (mg/L)	Ca (mg/L)	Fe (mg/L)	K (mg/L)	Mg (mg/L)	Mn (mg/L)	Na (mg/L)	S (mg/L)	Si (mg/L)	Zn (mg/L)	SO_4/Cl	δ D	$\delta^{18}O$	Saturation Indices					
CHARAS SLUMP																											$BaSO_4$	$CaSO_4.2H2O$	$CaSO_4$	$Fe(OH)_3$	FeOOH	$CaCO_3$
10-LM-06	2010	End of mudflow	67.2635	-135.219	7.06	664	49.29	92.4	0.74	318	1.01	0.03	<0.025	0.03	107.37	<0.006	3.46	24.62	0.0036	21.18	-	1.47	-	430.36	-173.2	-22.8	0.56	-0.99	-1.25	-	-	-0.73
10-LM-12	2010	Headwall	67.25456	-135.23066	6.82	1326	515.10	142.3	1.51	865	0.16	0.04	<0.025	0.02	246.57	0.009	9.14	63.34	0.6698	45.03	-	1.94	-	572.59	-219.5	-27.4	0.52	-0.43	-0.68	-0.4	4.73	-0.33
10-LM-31	2010	Headwall	67.25456	-135.23066	7.03	1700	499.43	170.2	1.51	1167	0.07	0.04	<0.025	0.02	326.46	<0.006	10.28	80.50	1.0066	45.96	-	2.19	-	772.68	-216.4	-26.9	0.56	-0.25	-0.51	-	-	-0.21
10-LM-11	2010	Halfway down mudflow	67.2568	-135.2367	6.92	2025	459.92	129.7	1.83	1782	3.54	0.06	<0.025	0.02	517.63	0.016	11.14	118.38	1.3752	57.15	-	2.15	-	973.31	-205.8	-25.7	0.59	-	-0.25	-0.59	4.54	-0.31
10-LM-30	2010	Halfway down mudflow	67.2568	-135.2367	6.86	2700	697.52	175.9	3.80	1866	0.11	0.06	<0.025	0.02	537.01	<0.006	11.33	130.18	2.3901	61.20	-	2.67	-	490.84	-192.8	-24.5	0.62	0.06	-0.2	-	-	-0.23
10-LM-29	2010	End of mudflow	67.2635	-135.219	6.78	1464	132.51	138.3	2.50	807	0.07	0.04	<0.025	0.02	232.02	<0.006	6.16	55.55	0.8963	57.18	-	1.81	-	322.42	-175.6	-22.6	0.52	-0.46	-0.72	-	-	-0.63
11-LM-20	2011	End of mudflow	67.26443	-135.21587	7.76	537	21.19	58.1	0.94	206	0.43	0.01	<0.025	-	60.32	<0.006	2.44	17.30	0.1550	12.21	77.62	0.81	0.0034	218.72	-175.4	-23.0	0.49	-1.33	-1.58	-	-	-0.43
11-LM-21	2011	1/3 down mudflow	67.26207	-135.23082	8.12	179.7	4.69	28.8	0.47	72	0.36	0.05	<0.025	-	28.00	0.211	1.29	6.14	0.0223	3.45	27.60	1.23	<0.003	155.12	-182.7	-23.8	0.06	-1.96	-2.21	3.41	8.54	-0.62
11-LM-22	2011	Halfway down mudflow	67.25687	-135.23694	7.3	1943	691.15	69.4	2.00	1897	0.27	0.06	<0.025	-	609.56	<0.006	11.86	117.46	0.9540	65.98	756.03	1.43	0.0204	950.65	-210.3	-26.1	0.59	0.08	-0.17	-	-	-0.14
11-LM-23	2011	Headwall	67.25415	-135.23106	7.23	1841	832.16	128.9	2.32	1905	0.27	0.06	<0.025	-	606.58	0.007	11.59	138.97	1.0804	69.34	777.62	1.94	0.0032	821.16	-205.9	-25.5	0.59	0.07	-0.19	0.02	5.15	0.05
11-LM-41	2011	End of Mudflow	67.26443	-135.21587	8.01	519	37.64	50.7	0.84	201	0.39	0.01	<0.025	-	64.08	<0.006	2.77	14.18	0.1663	11.44	76.37	0.88	<0.003	238.09	-177.2	-22.7	0.31	-1.3	-1.56	-	-	-0.21
11-LM-43	2011	Left stream end of mudflow	67.26443	-135.21587	7.79	500	37.68	100.0	1.10	232	0.85	0.01	<0.025	-	78.92	<0.006	2.52	15.90	0.1120	18.29	89.73	1.10	<0.003	211.54	-176.2	-22.7	0.33	-1.19	-1.45	-	-	-0.06
11-LM-44	2011	Right stream end of mudflow	67.26443	-135.21587	8.2	620	2.88	27.9	0.16	242	0.44	0.02	<0.025	-	60.01	0.127	1.65	25.20	0.0156	12.72	94.76	1.12	<0.003	1532.23	-167.4	-21.4	0.35	-1.28	-1.54	3.23	8.35	-0.33
11-LM-45	2011	Point in mudflow where 2 streams converge	67.25885	-135.23621	7.71	389	22.64	57.6	3.81	189	0.55	0.01	<0.025	-	57.62	0.049	2.08	12.25	0.1246	8.04	60.76	1.09	<0.003	49.61	-177.6	-23.0	0.3	-1.36	-1.62	2.27	7.39	-0.49
11-LM-46	2011	Halfway down mudflow	67.25687	-135.23694	7.47	2075	508.30	127.2	1.76	1738	0.31	0.05	<0.025	-	610.04	<0.006	11.09	112.70	0.7616	59.62	730.97	1.67	0.0057	986.24	-194.2	-23.9	0.58	0.06	-0.20	-	-	0.30
11-LM-60	2011	Halfway down mudflow	67.25687	-135.23694	7.14	1920	859.00	169.5	2.33	1883	0.25	0.06	<0.025	-	605.85	<0.006	10.88	130.92	1.6028	64.16	763.67	2.10	<0.003	808.01	-204.4	-25.5	0.59	0.06	0.06	-0.19	-	-0.12
11-LM-61	2011	Headwall	67.25415	-135.23106	6.77	1829	880.55	183.0	8.3746	2078	1.01	0.06	<0.025	-	614.65	<0.006	20.72	133.37	0.1627	66.24	770.11	2.07	0.0087	248.09	-196.4	-24.6	0.6	0.09	-0.16	-	-	0.1
11-LM-66	2011	Halfway down mudflow	67.25687	-135.23694	7.40	1330	911.45	178.5	1.6683	1863	<0.025	0.05	<0.025	-	605.40	0.018	12.81	124.58	1.3585	72.68	756.29	2.12	0.0067	1116.69	-200.2	-24.1	0.59	0.06	-0.19	-1.06	4.07	-0.27
11-LM-67	2011	Confluence of lake discharge and slump runoff	67.25784	-135.23791	7.03	342	38.85	60.4	0.4192	199	0.41	0.01	<0.025	-	76.74	0.010	2.50	14.95	0.1035	7.54	73.12	1.67	<0.003	473.72	-159.9	-21.3	0.29	-1.25	-1.5	0.77	5.9	-0.66
11-LM-70	2011	Confluence of lake discharge and slump runoff	67.25784	-135.23791	6.75	203.8	5.11	22.9	0.4697	100	0.41	0.07	<0.025	-	32.74	0.286	1.15	8.96	0.1190	5.07	35.52	2.29	0.0044	211.90	-159.7	-21.2	0.15	-1.79	-2.04	1.22	6.35	-1.76
11-LM-72	2011	Slump runoff at confluence with lake discharge	67.25784	-135.23791	7.18	2214	723.72	143.6	1.8775	1770	<0.025	0.06	<0.025	-	583.28	0.015	12.63	118.42	0.8414	67.75	725.21	1.68	0.0079	942.71	-194.0	-24.8	0.58	0.04	-0.22	-1.4	3.72	-0.39
11-LM-58	2011	End of mudflow	67.26443	-135.21587	6.94	460	44.31	65.4	0.44	195	0.22	0.04	<0.025	-	67.03	0.086	2.69	13.00	0.2017	8.64	69.99	1.15	<0.003	443.01	-168.7	-22.0	0.3	-1.3	-1.56	1.08	6.21	-0.9
Mean					**7.29**	**1217.34**	**362.50**	**105.50**	**1.86**	**980.61**	**0.56**	**0.04**	**-**	**0.02**	**305.81**	**0.08**	**7.37**	**67.13**	**0.64**	**38.22**	**367.83**	**1.66**	**0.01**	**589.53**	**-187.9**	**-23.9**	**0.46**	**-0.68**	**-0.90**	**0.70**	**5.90**	**-0.38**
StDev					**0.46**	**784.95**	**354.93**	**54.10**	**1.77**	**798.93**	**0.75**	**0.02**	**-**	**0.00**	**251.47**	**0.10**	**5.38**	**52.70**	**0.65**	**26.58**	**352.59**	**0.51**	**0.01**	**387.06**	**18.0**	**1.8**	**0.16**	**0.70**	**0.71**	**1.53**	**1.58**	**0.41**
MELANIE SLUMP																																
11-LM-14	2011	End of Mudflow	67.25184	-135.26187	6.96	135.4	15.34	41.6	1.08	61	1.02	0.08	<0.025	-	23.74	0.283	2.53	7.51	0.0763	6.23	24.33	1.12	<0.003	56.51633	-184.6	-23.6	0.18	-2.1	-2.35	1	6.13	-1.68
11-LM-15	2011	Halfway down mudflow	67.25201	-135.26555	7.15	140	10.87	42.3	1.07	56	1.23	0.06	<0.025	-	21.11	0.237	2.19	7.28	0.0254	5.85	21.53	1.00	<0.003	52.51573	-182.3	-23.5	0.15	-2.17	-2.43	1.51	6.63	-1.52
11-LM-16	2011	Headwall	67.25216	-135.27213	6.89	813	80.07	36.0	1.90	373	0.38	0.02	<0.025	-	90.21	0.008	8.59	25.03	0.1409	42.50	156.40	0.48	<0.003	196.0961	-209.9	-26.8	0.6	-1	-1.26	-0.77	4.36	-1.4
11-LM-17	2011	Base of headwall-sheet flow	67.25451	-135.27377	6.88	1062	0.00	60.4	2.64	554	0.34	0.02	<0.025	-	118.05	<0.006	10.66	36.48	0.3121	69.66	217.23	0.71	0.0041	210.1699	-218.1	-27.9	0.66	-0.8	-1.06	-	-	-1.12
11-LM-50	2011	Upper mudflow	67.25451	-135.27377	8.01	2379	1.24	67.4	4.76	1287	5.04	0.04	<0.025	-	332.50	<0.006	10.48	92.41	1.6512	93.02	499.76	1.02	0.0075	270.3458	-181.9	-22.9	0.74	-0.23	-0.48	-	-	0.35
11-LM-51	2011	Halfway down mudflow	67.25201	-135.26555	8.14	1219	5.24	47.0	1.95	585	0.25	0.02	<0.025	-	152.28	0.007	4.98	42.72	0.8432	34.03	223.15	0.82	0.0067	300.4577	-173.1	-22.4	0.66	-0.69	-0.94	2.08	7.2	0.12
11-LM-52	2011	End of mudflow	67.25184	-135.26187	8.56	112	4.75	22.1	0.43	46	0.29	0.14	<0.025	-	14.23	0.465	1.30	5.06	0.1238	3.24	15.97	1.39	0.0037	106.435	-172.3	-23.3	0.12	-2.39	-2.65	3.82	8.95	-0.59
11-LM-74	2011	Melanie site, below lobes on mudflow	67.25279	-135.2717	6.72	1121	1.13	18.5	2.50	757	2.76	0.04	<0.025	-	199.38	0.007	9.79	61.50	1.1761	62.56	319.16	1.97	0.0549	303.1629	-159.8	-20.0	0.69	-0.53	-0.79	-1.35	3.78	-1.62
11-LM-74C	2011	Top of Mudflow- left of lobe	67.25298	-135.27299	5.78	1317	2.36	2.2	3.99	942	2.22	0.13	<0.025	-	233.34	0.010	12.36	70.09	1.9725	81.93	390.84	1.96	0.1500	236.266	-177.1	-22.1	0.72	-0.42	-0.68	-4.19	0.94	-3.44
10-LM-14	2010	End of Mudflow	67.2519	-135.26321	7.8	302	15.32	46.0	0.62	123	1.24	0.03	<0.025	0.05	46.19	0.073	2.98	16.01	0.0720	8.96	-	1.51	-	198.621	-172.2	-22.8	0.58	-1.6	-1.86	2.64	7.77	-0.54
10-LM-17	2010	Halfway down mudflow	67.25361	-135.27319	7.10	95	2.51	23.4	1.26	34	0.57	0.06	<0.025	0.09	14.28	0.557	1.16	6.23	0.0116	3.39	-	1.68	-	27.32087	-168.6	-21.9	0.37	-2.52	-2.78	1.88	7.21	-1.89
10-LM-19	2010	Headwall	67.25297	-135.27179	6.68	1352.5	227.55	163.3	3.11	648	0.06	0.04	<0.025	0.02	167.75	0.013	12.66	54.32	0.9508	70.71	-	1.79	-	208.4588	-234.6	-29.3	0.49	-0.65	-0.9	-1.53	3.6	-0.78
10-LM-20	2010	Halfway down mudflow	67.25361	-135.27319	7.21	2017	2.50	*0.3*	4.85	1100	0.07	0.04	<0.025	0.06	250.54	0.077	11.18	86.48	1.3228	84.91	-	1.20	-	226.6051	-192.1	-23.3	1.04	-0.36	-0.62	0.98	6.11	-4.09
10-LM-39	2010	End of mudflow	67.25194	-135.26707	7.64	868	77.02	49.1	1.76	417	2.14	0.09	<0.025	0.04	99.50	0.163	5.06	37.77	0.1691	28.42	-	1.33	-	237.5383	-169.7	-21.6	0.74	-0.94	-1.2	2.56	7.69	-0.49
10-LM-41	2010	Halfway down mudflow	67.25361	-135.27319	7.00	2893	3.40	93.5	7.41	1594	0.55	0.05	<0.025	0.02	342.53	0.015	15.42	118.75	1.5282	118.33	-	0.85	-	215.1868	-193.0	-22.6	0.59	-0.17	-0.43	-0.33	4.8	-0.53
10-LM-42	2010	Edge of slump, pond, rain, no runoff	67.25293	-135.27103	7.10	2352	1.00	9.1	5.38	1355	0.03	0.31	<0.025	0.02	280.46	0.010	13.83	106.76	2.1469	75.58	-	1.07	-	251.9972	-182.6	-22.5	0.58	-0.27	-0.53	-0.28	4.85	-1.61
10-LM-61	2010	End of mudflow	67.25194	-135.26707	7.13	159.8	4.44	*12.0*	4.36	62.59	0.39	0.03	<0.025	-	18.54	0.259	1.23	6.93	0.0034	4.33	-	2.88	-	14.35562	-160.8	-20.9	-	-2.19	-2.44	1.62	6.95	-2.07
10-LM-62	2010	Halfway down mudflow	67.25204	-135.27165	8.52	2515	2.00	262.4	3.60	1390.36	<0.025	0.17	<0.025	-	338.02	0.138	13.27	124.58	0.2630	93.06	-	0.42	-	386.5977	-174.4	-21.1	-	-0.25	-0.5	2.94	8.26	1.47
10-LM-63	2010	Headwall	67.25297	-135.27179	7.02	1495	67.26	*0.0*	5.62	797.06	0.12	0.17	<0.025	-	145.58	0.046	13.27	53.68	0.3496	100.43	-	0.69	-	141.7194	-222.1	-27.6	-	-0.63	-0.89	-	-	-
Mean					**7.28**	**1176.19**	**27.58**	**52.5**	**3.07**	**641.16**	**1.04**	**0.08**	-	**0.04**	**152.01**	**0.14**	**8.05**	**50.50**	**0.69**	**51.96**	**207.60**	**1.26**	**0.04**	**191.60**	**-185.7**	**-23.5**	**0.56**	**-1.05**	**-1.30**	**0.79**	**5.95**	**-1.19**
StDev					**0.69**	**910.71**	**55.22**	**63.8**	**1.95**	**520.32**	**1.29**	**0.07**	**-**	**0.02**	**117.17**	**0.17**	**5.03**	**39.99**	**0.73**	**39.07**	**172.94**	**0.61**	**0.06**	**101.24**	**21.1**	**2.5**	**0.25**	**0.83**	**0.83**	**2.07**	**2.09**	**1.30**
Mean					***7.28***	***1198.27***	***207.29***	***80.9***	***2.42***	***823.31***	***0.78***	***0.06***	-	***0.03***	***234.54***	***0.11***	***7.69***	***59.43***	***0.66***	***44.59***	***310.15***	***1.47***	***0.02***	***405.12***	***-186.9***	***-23.7***						
StDev					***0.57***	***834.95***	***310.00***	***63.9***	***1.93***	***697.35***	***1.06***	***0.06***	**-**	***0.02***	***213.08***	***0.15***	***5.17***	***47.42***	***0.68***	***33.26***	***306.32***	***0.59***	***0.04***	***351.61***	***19.3***	***2.2***						
Max Value					***8.56***	***2893.00***	***911.45***	***262.4***	***8.37***	***2077.67***	***5.04***	***0.31***	**-**	***0.09***	***614.65***	***0.56***	***20.72***	***138.97***	***2.39***	***118.33***	***777.62***	***2.88***	***0.15***	***1532.23***	***-159.7***	***-20.0***						
Min Value					***5.78***	***95.00***	***0.00***	***0.0***	***0.16***	***34.35***	***0.03***	***0.01***	-	***0.02***	***14.23***	***0.01***	***1.15***	***5.06***	***0.00***	***3.24***	***15.97***	***0.42***	***0.00***	***14.36***	***-234.6***	***-29.3***						

Appendix C: Suspended Sediment Results

Table C1. Particle size analysis of suspended sediments

CHARAS	**Mean Grain size (um)**	**% Sand**	**% Silt**	**% Clay**
Headwall (11-LM-12)	20.27	7.29	66.73	25.98
Headwall (11-LM-23)	19.96	6.48	73.98	19.84
Headwall (11-LM-61)	26.81	8.43	68.28	23.29
Halfway down mudflow (11-LM-11)	23.75	6.99	68.04	24.97
Halfway down mudflow (11-LM-46)	35.27	12.78	70.05	17.17
Halfway down mudflow (11-LM-60)	29.87	10.27	67.32	22.41
End of Mudflow (11-LM-06)	15.29	3.2	69.9	26.9
Mean	24.46	7.92	69.19	22.94
Stdev	6.26	3.03	2.45	3.47
MELANIE				
Headwall (10-LM-19)	12.28	1.51	61.4	37.09

Table C2. XRF results of suspended sediments and till samples from Charas and Melanie slumps

Sample	**Loss On**	**Sum**	**SiO2**	**Al2O3**	**CaO**	**K2O**	**MgO**	**MnO**	**Na2O**	**P2O5**	**Fe2O3(T)**	**Zn**	**TiO2**	**Ba**	**Ba**	**Co**	**Ga**	**La**	**Ni**	**Pb**	**Rb**	**Sr**	**Th**	**U**	**V**	**Y**	**Zr**	**Nb**	**Cr**	**Ce**	**Nd**
	(%)	**(%)**	**(%)**	**(%)**	**(%)**	**(%)**	**(%)**	**(%)**	**(%)**	**(%)**	**(%)**	**(ppm)**	**(%)**	**(ppm)**	**(%)**	**(ppm)**	**(ppm)**	**(ppm)**	**(ppm)**	**(ppm)**	**(ppm)**	**(ppm)**	**(ppm)**	**(ppm)**	**(ppm)**	**(ppm)**	**(ppm)**	**(ppm)**	**(ppm)**	**(ppm)**	**(ppm)**
SUSPENDED SEDIMENTS																															
10-LM-06	9.3	91.682	64.68	13.52	1.11	2.421	1.71	0.051	0.67	0.273	6.185	145	0.824	1182	0.1182	24	10	32	51	27	108	124	22	7	206	31	166	16	116	69	27
10-LM-12	8.9	92.066	65.69	12.97	1.42	2.322	1.77	0.048	0.75	0.268	5.815	142	0.793	1131	0.1131	21	3	44	39	48	105	125	36	17	192	28	180	15	107	56	18
10-LM-14	9.6	91.348	64.38	14.1	0.87	2.504	1.58	0.048	0.67	0.267	5.898	127	0.781	1170	0.117	21	12	54	32	30	113	130	26	13	222	29	181	15	121	89	31
10-LM-19	9.7	91.482	62.04	15.5	1.03	2.727	1.87	0.047	0.66	0.257	6.274	133	0.827	1188	0.1188	23	5	44	48	45	125	137	32	16	238	30	169	16	128	83	35
TILL																															
FM3 #9	11.99	87.126	61.66	12.87	1.17	2.339	1.66	0.046	0.70	0.265	5.410	218	0.747	1155	0.1155	19	14	45	28	24	109	135	18	11	204	34	225	13	141	84	40
FM3 #11	10.68	91.013	65.66	13.01	0.99	2.353	1.59	0.045	0.69	0.247	5.419	139	0.763	1132	0.1132	18	10	52	33	28	109	127	25	15	198	32	220	13	138	80	34
FM4 #3	8.51	91.811	70.60	9.14	1.62	1.652	1.54	0.050	0.92	0.277	5.086	180	0.721	947	0.0947	23	<10	11	18	34	74	110	26	14	136	34	259	12	97	67	37
FM4 #4	9.96	91.932	66.13	12.46	1.52	2.234	1.79	0.050	0.73	0.277	5.746	164	0.762	1091	0.1091	14	<10	36	20	30	103	127	23	12	191	34	216	14	122	65	32
FM10 #11	11.64	89.152	62.92	13.45	1.08	2.418	1.66	0.045	0.70	0.225	5.623	140	0.794	1055	0.1055	21	16	70	24	30	113	126	19	12	215	34	199	15	132	84	35
FM10 #13	7.80	93.386	67.46	13.63	0.75	2.430	1.49	0.025	0.73	0.232	5.601	137	0.788	1190	0.119	17	<10	24	25	29	116	124	24	12	211	32	228	12	136	45	29
FM10 #14	11.11	90.577	59.19	17.30	0.80	3.034	1.88	0.041	0.49	0.247	6.486	148	0.839	1210	0.121	25	16	49	40	25	144	138	17	<10	284	32	157	15	163	117	51
FM10 #15	12.26	90.183	58.90	17.18	0.88	3.024	1.89	0.044	0.50	0.245	6.444	143	0.834	1160	0.116	22	15	50	26	32	149	144	25	14	277	35	156	15	156	61	34
FM10 #16	11.80	88.971	59.60	15.50	0.96	2.755	1.70	0.044	0.64	0.260	6.441	213	0.813	1187	0.1187	23	19	56	34	30	132	142	18	11	258	36	180	13	145	74	29
FM10 #15a	10.07	92.447	60.28	17.68	0.88	3.121	1.95	0.045	0.50	0.252	6.603	144	0.857	1219	0.1219	21	20	63	29	28	151	148	20	12	298	35	161	17	162	98	46